ALGORITHM THEORETICAL BASIS DOCUMENT (ATBD)

for the

ENVIRONMENT DATA RECORD (EDR) ALGORITHM

of the

OZONE MAPPING AND PROFILER SUITE (OMPS) LIMB PROFILER

NATIONAL POLAR-ORBITING OPERATIONAL ENVIRONMENTAL SATELLITE SYSTEM (NPOESS) PROGRAM

Prepared by

Didier F. Rault, NASA Langley Research Center, Hampton, Virginia

Co-authors

Robert Loughman, Hampton University
Ghassan Taha, Science Systems and Applications Inc, Lanham, Maryland
Albert. J. Fleig, PITA Analytic Sciences, Bethesda Maryland

TABLE OF CONTENTS

LIST OF FIGURES

LIST OF TABLES

1.0 INTRODUCTION

This document provides the physical theory and mathematical background underlying the Ozone Mapping and Profiler Suite (OMPS) / Limb Profiler (LP) retrieval algorithms. It describes the Environmental Data Record (EDR) algorithm, which generates science data from the calibrated and spectrally/spatially registered radiance data produced by the Sensor Data Record (SDR) algorithm. This document identifies the sources of input data that are required by the algorithms, lists assumptions, describes the SDR and EDR primary products as well as additional by-products, details expected sensor and algorithm errors (accuracy and precision), and discusses the performance of the algorithms.

This document is sub-divided into 5 sections. The Introduction (Section 1.0) provides information on the OMPS mission goals, objectives and requirements. The fundamental role of the OMPS suite is to provide information on the global distribution of ozone both in terms of Total Column amount and vertical profiling. The requirements for the OMPS instrument have changed as a consequence of the **N**unn McCurdy National Polar-Orbiting Operational Environmental Satellite System (NPOESS) project revision, with the OMPS/LP sensor being downgraded to a "Research Status" with streamlined pre-launch sensor testing. To retrieve ozone vertical distribution, the OMPS/LP uses the Limb Scatter (LS) method, with the sensor designed to view the Earth limb through three narrow vertical slits, handling the wide dynamic range of radiances with a combination of narrow/wide apertures and short/long integration times. The Earth limb radiance data is imaged onto a single focal plane and recorded on a two dimensional Charge Coupled Device (CCD) array. By necessity, the OMPS/LP requires a relatively large downlink data rate and the concept of operations for the instrument relies on optimizing the downloaded information in the form of the Sample Table (ST). The primary output of the OMPS/LP retrieval algorithm is the ozone density profile, while the secondary products include the aerosol extinction profile, one moment of the aerosol size distribution, the cloud top height and the effective surface albedo.

Section 2.0 outlines the overall structure of the OMPS/LP data process, with Raw Sensor Data (RDR) being first processed by the SDR algorithm and subsequently by the EDR algorithm. The SDR algorithm is described in a separate document, namely the Algorithm Theoretical Basis Document for the Sensor Data Record *[Jaross et al., 2010]*. Section 3.0 describes the EDR algorithm. With consideration of the OMPS/LP status as a "research instrument" and the consequent limited sensor characterization, the selected approach for the EDR was to develop a mainstream algorithm and a series of alternates. The mainstream algorithm is based on heritage from previous LS missions, but requires extensive data preprocessing to be done by the SDR (such as two-dimensional gridding and explicit gain consolidation). The alternative methods are based either on spectral fitting (which has the potential of identifying instrument artifacts and evaluating correction for these effects) or on the direct use of the large ensemble of radiance data measured individually by each CCD array pixel. The mainstream algorithm, which will be relied upon at least in the early phase of on-obit operations, is described in the main body of this document, whereas the two alternative algorithms are described in Appendices A and B. The EDR algorithms are based on the Optimal Estimation (OE) method to retrieve profile information, and the specific application of the OE method to the OMPS/LP sensor is described in Section 3.2. The retrieval methodology basically compares measured data with the radiances

simulated with a forward model composed of (a) a Multiple Scatter (MS) Radiative Transfer (RT) model and (b) an Instrument Model (IM). The ozone profile retrieval strategy consists of a series of sequential steps. First, for each LS event, the spectral and spatial registrations are checked or corrected using scene based methods. Second, a suite of secondary parameters (also called Intermediate Products or IP) are retrieved, such as surface albedo and aerosol extinction. Finally, all the derived IP are used to extract ozone density profiles from the SDR calibrated radiance data. At the conclusion of the retrieval process, a residual analysis is performed by comparing the spectral radiance data with the radiance simulated by the forward model which is run using all the derived products. The assumptions made by the EDR are concerned with simplifications made in the forward model RT and IM. The EDR data processing requires both static and dynamic databases. The static databases include the pre-launch sensor calibration tables, a reference solar spectrum and spectroscopic data, while the dynamic databases are SDR HDF file and climatology files for ozone, NO_2 and aerosol. The retrieval uncertainties intrinsic to the EDR algorithm may originate from either random noise or from offset biases (e.g., spectroscopic data, assumed NO_2 profile). The output of the EDR algorithm is written in three sets of files, namely: an HDF formatted file containing the vertical profiles of ozone and aerosol extinction as well as other intermediate parameters for all LS events occurring in one orbit, a set of three diagnosis files which graphically shows the performance of the retrieval process for each LS event (one for each slit), and a set of three curtain files which shows the ozone profiles retrieved for a whole orbit (one for each slit)

The performance of the SDR and EDR algorithms is described in Section 4.0. The performance of the algorithms is analyzed in terms of code functionality and overall code accuracy. While the former testing requires relatively simple testing datasets, the latter necessitates more elaborate tools such as a detailed instrument model as well as a large ensemble of synthetic and proxy limb scatter events encompassing a wide set of viewing conditions, atmospheric composition and viewing scene characteristics. Codes are tested at three levels: module, whole algorithm (both SDR and EDR), and end to end, i.e., SDR+EDR. For the latter level, a chain of codes was assembled and linked together as a one-unit testing tool. This tool, which is called "A-to-Z chain" includes: (1) the forward model, which simulates the limb radiance for a given atmosphere and viewing conditions, (2) a detailed instrument model, which simulates the main functions of the actual OMPS/LP sensor, including instrument effects such as straylight contamination and spectral/radial smiles, (3) the most critical SDR modules (straylight mitigation, two-dimensional gridding, gain consolidation), and (4) the complete EDR algorithm. The performance of the SDR+EDR set of codes is statistically evaluated by passing large simulated datasets through the A-to-Z chain. Typical test datasets involve several hundred LS events occurring over a wide range of geo-locations, seasons and corresponding to a broad spectrum of viewing conditions.

The final section (Section 5.0) is devoted to an end-to-end error analysis for the SDR+EDR series of codes. This error analysis is complex as it involves the effect of a series of parameters on the ozone density retrieval uncertainties. The analysis is sub-divided into errors affecting the accuracy of the retrieval and errors affecting the precision of the retrievals. The analysis is based partly on (1) earlier work performed by previous authors of the OMPS/LP algorithm and partly on (2) recent results obtained using the A-to-Z chain testing tool.

1.1 OMPS mission overview: objectives and scope

The OMPS suite is an important component of the NPOESS program. OMPS is one of the five instruments to be manifested on the NPOESS Preparatory Project (NPP), which is scheduled to be launched in 2011. The OMPS dataset is aimed at building up the Environmental Data Records (EDRs) to describe the global vertical, horizontal and temporal distribution of ozone in the Earth's atmosphere.

OMPS was conceived *[Graf et al., 2000; Leitch et al., 2003]* and built to allow the scientific community to continue the long-term record of ozone and aerosol measurements initiated more than 30 years ago by the Stratospheric Aerosol and Gas experiment (SAGE) family of sensors *[McCormick, 1989; Mauldin, 1998]*, the Total Ozone Mapping Spectrometer (TOMS) *[McPeters, 1991]* and the Solar Backscatter Ultraviolet Instrument (SBUV) *[Heath et al., 1975; Frederick et al., 1986; Hilsenrath et al., 1995]*.

1.2 OMPS Mission description

The OMPS instrument was designed and built by Ball Aerospace and Technology Corporation (BATC) under contract from the Integrated Program Office (IPO). As described by *[Flynn et al., 2007]* and as shown in Figure 1-1, OMPS is composed of three instruments, namely the Total Column mapper (TC), the Nadir Profiler (NP) and the Limb Profiler (LP). These three instruments have heritage respectively from TOMS, SBUV and the Shuttle Ozone Limb Sounding Experiment / Limb Ozone Retrieval Experiment (SOLSE/LORE) *[McPeters et al., 2000]*. The nadir system has two focal planes; one operating from 300 to 380 nm for total column ozone observations; the other operating at 250 to 310 nm for profile ozone observations. The limb system has one focal plane operating from 290 to 1020 nm for high vertical resolution profile ozone observations.

The first OMPS mission will be mounted on the NPP satellite, which will operate in a near circular, sun-synchronous orbit, with a 10:30am descending-node orbit at an altitude of 824 km.
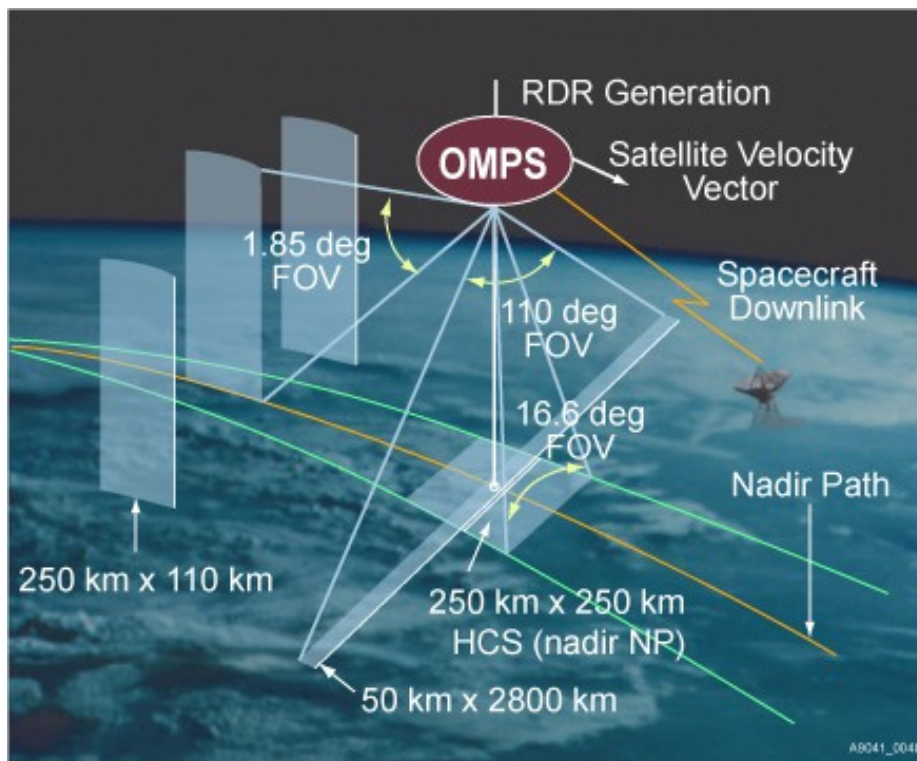
Figure 1-1. *OMPS instruments: TC, NP and LP sensors. The OMPS/LP views the Earth's limb through three thin vertical slits (about 110 km high) in the spacecraft aft direction. (Courtesy of BATC)*

1.3   OMPS mission requirements and goals

The three OMPS sensors (NP, TC and LP) were originally designed as a comprehensive set to monitor the ozone horizontal and vertical distributions. However, the NPOESS mission redesign, which was spurred by the Nunn-McCurdy review, fundamentally altered the status of the limb sensor. The OMPS/LP sensor has been downgraded to a "Research" instrument, which curtailed further development on the sensor and limited the scope of instrument calibration. The new requirement on the OMPS/LP sensor and mission basically consists of:

(1) Obtaining the best ozone profile product
(2) Performing the SDR+EDR retrieval in a timely fashion (3-5 CPU minutes per limb scatter event per slit)
(3) Characterizing the sensor on-orbit performance
(4) Evaluating the sensor capability to meet its stated specifications
(5) Constructing all analytical tools to be ready by launch time

The consequence of these new requirements was to place more emphasis on data analysis, creating the need for additional tools such as (1) a detailed instrument model to simulate instrument effects and generate high fidelity synthetic datasets for code testing and (2) an end-to-end testing workbench to test the most critical modules of the algorithm and quantify the effect of sensor and algorithm uncertainties/assumptions on retrieved ozone accuracy and precision. Increased flexibility to the retrieval algorithm was also added in terms of alternative EDR

retrieval algorithms, the first one relying on spectral fitting (useful in identifying and correcting for instrument effects) and the second one requiring minimal data preprocessing (essentially using raw CCD array measurements).

1.4 OMPS/LP sensor description

1.4.1 OMPS/LP sensor concept: The Limb Scatter method

The OMPS/LP is a Limb Scatter (LS) sensor. It is designed to observe the Earth's limb radiance in the 290-1020 nm spectral range where the prime source of light is solar radiance being scattered by atmospheric molecules (Rayleigh scatter), suspended liquid and solid particulates (aerosols), clouds and the Earth's surface (see Figure 1-2). OMPS/LP has heritage from other LS instruments, such as the Ultraviolet Spectrometer on the Solar Mesosphere Explorer (UVS/SME) *[Rusch et al., 1984]*, the Shuttle Ozone Limb Sounding Experiment / Limb Ozone Retrieval Experiment (SOLSE/LORE) *[McPeters et al., 2000]*, the Stratospheric Aerosol and Gas Experiment (SAGE III) *[Rault, 2005a; Rault and Taha, 2007]*, the Optical Spectrograph and Infrared Imager System (OSIRIS) *[Llewellyn et al,.2004]* and the SCanning Imaging Absorption spectroMeter for Atmospheric ChartograpHY (SCIAMACHY) *[Bovensmann et al,1999]*.
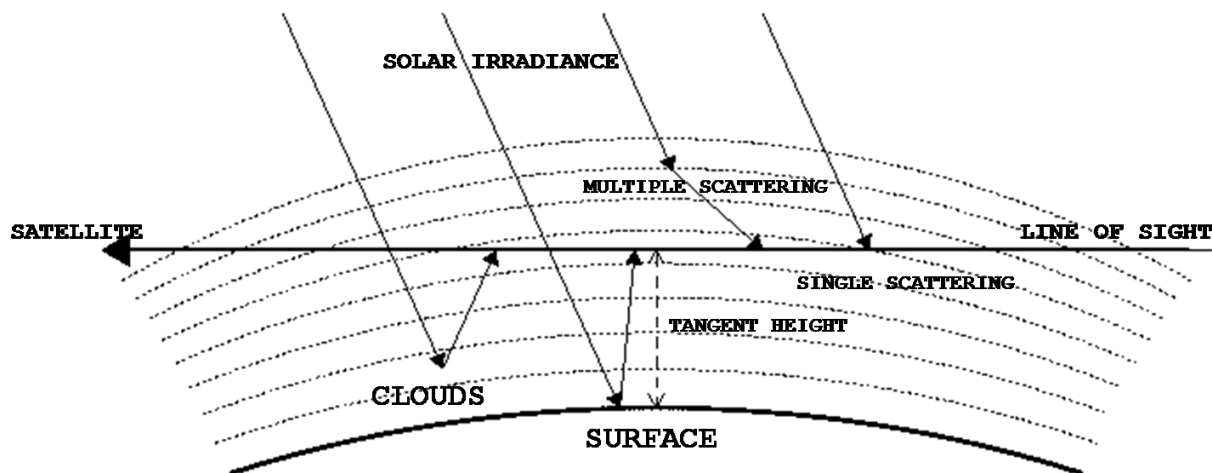
Figure 1-2. *Illustration of the LS viewing geometry. The atmosphere scatters sunlight into the line of sight (LOS) thru molecular (Rayleigh) and aerosol scattering and cloud/surface reflection.*

To interpret the radiance measurements made by the OMPS/LP sensor requires an understanding of how the Earth's atmosphere interacts with UltraViolet (UV), visible, and near infrared (NIR) radiances. Incoming solar radiation undergoes absorption and multiple scattering in the atmosphere by atmospheric constituents such as ozone and aerosols, and Rayleigh scattering. Radiation that reaches the ground is scattered by surfaces of widely varying reflectivity. To retrieve ozone vertical distribution from the tropopause to 60 km, a series of spectral channels

are selected to observe a range of strongly absorbing to weakly absorbing features in the Hartley-Huggins and Chappuis bands. Within these ozone bands, absorption by other atmospheric components is relatively small. The ozone absorption coefficients differ from band to band, with the strongest absorption at lower wavelengths. Consequently, as wavelength decreases, significant absorption occurs at progressively higher levels in the atmosphere. Although in principle the scattered radiance at a given wavelength depends upon the entire ozone profile from the top of the atmosphere to the surface, in practice it is most sensitive to the ozone density over a restricted range in altitudes, predominantly in the vicinity of the tangent point. Consequently, measurements of scattered radiation at shorter wavelengths yield information on the ozone profile at higher levels of the atmosphere than measurements at longer wavelengths.

With respect to ozone retrieval, the OMPS/LP spectral range can be subdivided into three wavelength regions:

- In the shorter wavelength range (typically 280-295 nm), solar radiation is almost completely absorbed above the ozone density peak (typically located at 20-25 km), and consequently tropospheric features (such as clouds, aerosols and terrain height) do not affect the limb signal measured by OMPS/LP. The limb signal at these wavelengths is dominated by the ozone profile above the peak, and therefore, it can be used to retrieve ozone profile at high altitudes, typically between 45 and 60 km. At these high altitudes, radiation scatter is mostly Rayleigh single scatter, which permits relatively simple retrievals.

- Between 295 nm and 310 nm, scattering takes place over a wide range of altitudes, but tropospheric features still only have a small effect on the limb signal. The limb signal at these wavelengths provides ozone profile information near and below the ozone peak. At these altitudes, multiple scatter effects become important, which necessitates the use of more complex forward models.

- For wavelengths longer than 310 nm, the limb signal is affected by the stratosphere, troposphere and the Earth's surface. Clouds, surface reflectance, aerosols and terrain height strongly influence the diffuse radiation field in the troposphere and lower stratosphere.

The retrieval of ozone information from limb signal observations requires the modeling of non-isotropic scattering within the Earth's atmosphere (by molecules and aerosols) as well as reflection from the Earth's surface (modeled as a Lambertian surface)

1.4.2 OMPS/LP sensor description

The OMPS/LP sensor simultaneously images the whole vertical extent of the Earth's limb, with a vertical Field-Of-View (FOV) of about 1.85° covering the 0-65 km nominal altitude range and allowing for boresight misalignment, spacecraft pointing error and Earth radius variation along the orbit (Figure 1-1). It is a triple-slit prism spectrometer that senses the limb radiance and solar irradiance over the wavelength range of 290 to 1020 nm. One of the slits is centered on the satellite ground track while the other two are pointing 4.25 deg (250 km) on either side (see Figure 1-1). The light entering the OMPS/LP instrument slits is dispersed by a prism and focused onto a single two-dimensional Charged Couple Device (CCD). The prism dispersion is uniquely suited for the OMPS/LP, providing high spectral resolution in the features-rich UV region and lower resolution in the somewhat featureless visible region, as shown in Figure 1-3. Figure 1-4 is a schematic representation of the CCD array layout. The primary technical challenges associated

with Limb Scatter measurements are (1) the large dynamic range of the limb signal, which typically varies by 4-5 orders of magnitude across the spectral/spatial ranges of interest, and (2) the ozone profile precision requirements which demand that radiances be measured at high Signal-to-Noise Ratio (SNR). To satisfy these two requirements, each slit is subdivided into a small and a large aperture, thus producing six distinct limb images on the CCD focal plane (Figure 1-4). Additionally, two different integration times are used to create a short and a long exposure of each image on the CCD array. Both the short and the long exposures are made of a series of sub-exposures (15 short and 10 long) which are interleaved and co-added on-board the spacecraft. The OMPS/LP sensor thus produces four images per slit spanning a gain range on the order of 100. The sensor can nominally provide 200 spectral channels for each detector image, but available data rates can only allow for a relatively small dynamic subset of these channels to be downlinked to the ground (about 10% of the CCD pixels for the short integration time and 15% for the long integration time). Residual straylight (both within a slit image and across slit images) is a significant portion of the measured signal, and therefore must be accounted for and corrected.
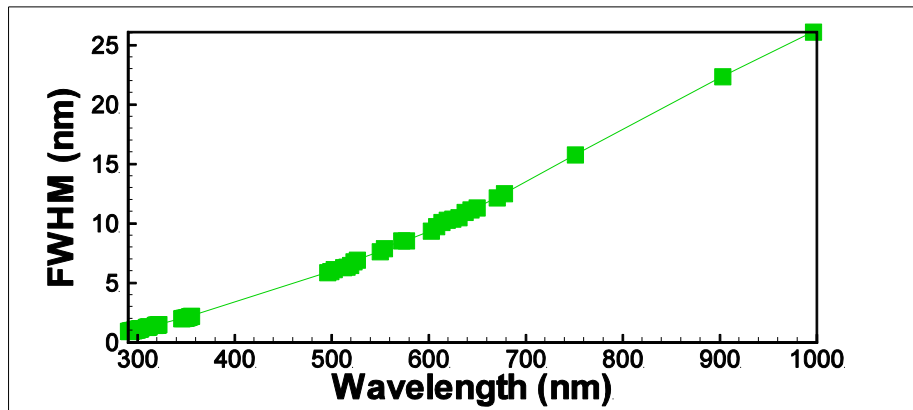
Figure 1-3. *OMPS/LP dispersion characteristics. The prism allows for variable spectral resolution, from 1 nm in the UltraViolet to 25 nm in near InfraRed.*
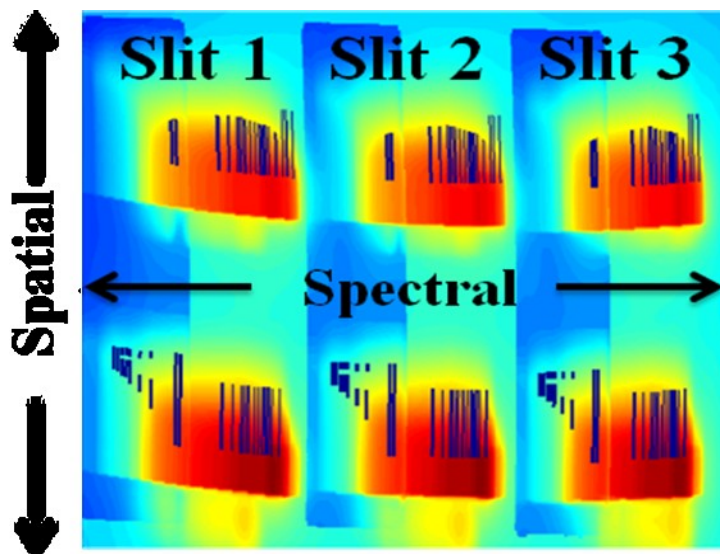
Figure 1-4. *OMPS/LP CCD array layout. The three slits are imaged onto a single 740x340 CCD array. Dark vertical lines represent the downlinked pixels. UV and visible filters are used to reduce cross-channel straylight. (Courtesy of BATC)*

The telescope is equipped with a depolarizer (to keep the linear polarization sensitivity below 2%) and two blocking filters (to minimize overlap of adjacent spectra on the focal plane). To further improve the SNR of the shortest UV channels, a Near-Infrared blocking filter was added for the large aperture images. The calibration stability (radiometric throughput and spectral registration), which is essential to enable long-term ozone monitoring, is maintained by periodic observations of the sun, using transmissive quartz diffusers to redirect the solar irradiance into the telescope. The reporting period is 19 s, corresponding to 150-km horizontal cell size along track. To satisfy the anticipated science needs, the instrument is designed with relatively tight specifications (Table 1-1), the most stringent being the precision of 3% from 15 to 50 km.

Table 1-1. *OMPS/LP instrument specifications and requirements*

Item	Specification
Spectral range	290 - 1020 nm
Spectral sampling interval	2 pixels per Full Width Half Maximum (FWHM)
Spectral resolution (FWHM)	1.5 - 40 nm (prism)
Field-of-View (FOV)	1.85° (3 slits, 4.25 deg apart)
CCD Pixel FWHM	1-1.5 km in elevation, 3 km in azimuth
Integration times	Long: 1.248 second, coadded 10 times
	Short: 0.068 second, coadded 15 times
Revisit time	5 days (average)
Vertical coverage	Tropopause — 60 km
Vertical cell size	resolution: 3 km, sampling: 1 km
SNR	320 (290nm at 60km) to 1200 (600nm at 15km)

Measurement range	0.1 - 16 ppmv
Reporting period	19 seconds (150 km along track)
CCD dimensions	740 (spectral) x 340 (spatial) pixels
Accuracy requirement	10% (15 - 60 km), 20% (Tropopause -15 km)
Precision requirement	3% (15 - 50 km), 10% (Tropopause - 15km, 50-60km)
Long-term stability requirement	2% over 7 years

Figure 1-5 shows a typical array of the sensor Signal-to-Noise-Ratios (SNR) for each CCD pixel. Note that data will be downloaded at the pixel level, i.e. no pixel binning will occur on board of the space platform. The Analog-To-Digital (ATD) converter has a full scale of 14 bits.
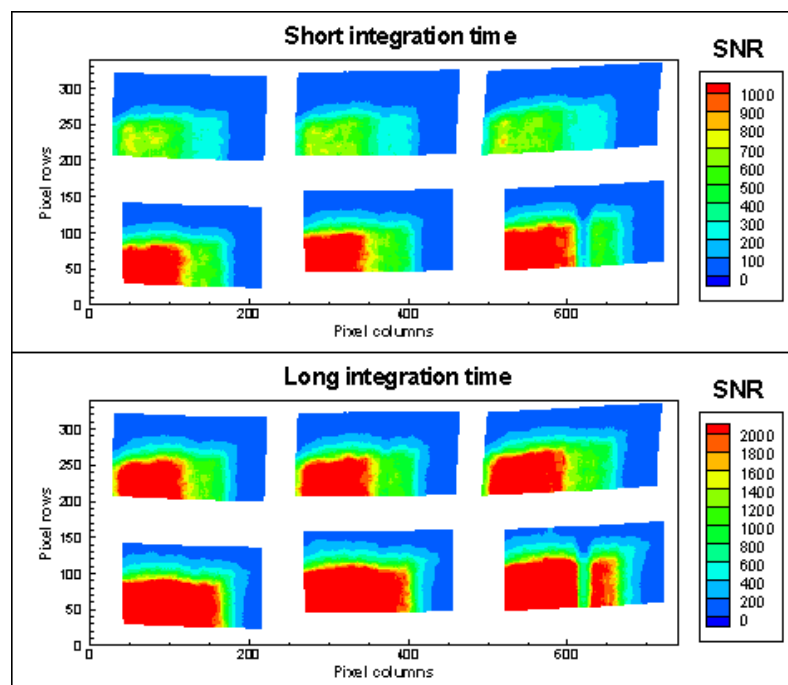
Figure 1-5. *OMPS/LP sensor Signal to Noise Ratio at short and long integration times*

1.5   Concept of operations

The OMPS/LP sensor design and measurement concept is a hybrid of predecessor limb sensors (SOLSE/LORE and SAGE III LS) and nadir-viewing Backscatterring UltraViolet (BUV) sensors (TOMS and SBUV). Earth-view data is obtained during dayside portions of the orbit in a constant and consistent data acquisition sequence. Calibration data is independently and occasionally obtained on the night-side or at the day-night boundary. The calibration data is downlinked to Earth in distinct data packets and subsequently processed separately from Earth-view data.

Each OMPS sensor was designed with a wide degree of flexibility by making extensive use of uploadable tables that can be readily updated on orbit. In addition to uploading updated tables (such as linearity, gain and sample tables) produced via the processing of calibration data, the

Command Sequence Memory (CSM) is also updated on a routine basis. Periodic updates to the CSM primarily involve such items as the scheduling of calibrations (routine and reference) and the start time of the Earth-view sequence due to the seasonal variation of the solar zenith angle. The three instruments of the OMPS suite must share the Main Electronics Box (MEB), which contains the computer controller and the signal processing electronics. During nominal Earth-view operations, all three sensors are imaging and sending data to the MEB, which necessitates a careful coordination of the individual integrations for all three sensors so as to prevent image pool buffers overload and the subsequent loss of data. Nominally, in Earth-view, the nadir and limb sensors cover the same range of solar zenith angles (up to 88 deg.), but begin their respective imaging sequences at different points along the orbit and the reporting periods are also different. Since the LP views the limb in the anti-velocity direction, it begins imaging about 7 minutes after the TC and NP sensors. The reporting periods, which must accommodate the science objectives of each sensor, are respectively: 19 sec. for the LP, 7 sec. for the TC and 37 sec. for the NP. At times, the LP will be interrupted to allow for calibration activities on the nadir sensors.

1.5.1   Pre-launch calibration dataset

The OMPS/LP sensor has undergone a suite of pre-launch tests, which resulted in establishing an initial set of calibration data. This set is composed of the 10 datafiles, which are described in Table 1-2.

Table 1-2. *OMPS/LP sensor calibration data set*

Dataset name	Dataset definition
CBC	Wavelengths at the center of each CCD pixel
SRG	Elevation angles at the center of each CCD pixel
BPS	Spectral slit function for each CCD pixel (121 elements)
FOV	Elevation slit function for each CCD pixel (121 elements)
RAD	Radiometric coefficients for each CCD pixel (counts to $W.sec/m^2/ster/nm$)
STB	Initial sample table
SLT	Point Spread Functions (PSF) and ghosts (straylight)
LED	Non-linearity correction table (as loaded into the sensor)
IRD	Irradiance calibration coefficient of each CCD pixel (counts to $W.sec/m^2/nm$)
GON	Goniometry coefficients for each CCD pixel

1.5.2   Spectral channel selection. Sample Table

The downlink data rate allocated for the OMPS/LP sensor is limited and, in normal Earth view mode, can only accommodate the download of a subset of the 740x340 CCD pixels, namely about 30000 pixels at short integration time and 50000 pixels at long integration time. The Sample Table is an editable uplink table which contains a list of the CCD pixels which (1) are "healthy" (ie. neither dead nor hot) and (2) are required by either the SDR or the EDR algorithms. The EDR algorithm requires certain spectral ranges and associated altitudes for the

ozone and aerosol retrievals: as shown in Section 3.5.6, the sensitivity of the limb radiance to ozone has two maxima, the first one in the UV for altitudes ranging from 25 to 60km and the second one in the visible in the altitude range 10-40km.

A series of channels were selected in these regions to provide overlapping vertical coverage, each channel being associated with an altitude range optimized for sensor SNR and maximum sensitivity to ozone. At the shortest OMPS wavelength, 290 nm, the cross-sections are greatest and provide coverage from 50-60 km. As the wavelength increases, the cross-section values decrease, and the range of usable altitudes moves downwards until, at 320 nm, the bottom altitude of the range is 25-28 km. In the visible, absorption cross sections are more uniform, but weaker, which limits the use of the Chappuis band data to below 40 km.

Aerosol properties are retrieved in spectral channels exhibiting weak gaseous absorption, such as on either side of the Chappuis band (500-520nm and 675 nm), and at longer wavelengths such as 740-750 nm, 840-860 nm and 900-1020 nm. As shown in Section 3.5.5, the sensitivity of the limb scatter signal to aerosol is typically small below 500 nm. The vertical extent for aerosol retrieval is typically 15-35 km, but it will vary with aerosol loading and scattering angle. Surface reflectance is retrieved using the same channels as aerosol in the 35-45 km range.

Additionally, the wavelength registration and straylight mitigation algorithms require downloading a series of pixel rows and columns (see Section 3.5.1). Moreover, since the OMPS/LP sensor is not steerable in elevation, allocation must be made for Earth's oblateness (±15 km). The size of the Sample Table can be reduced by identifying CCD pixels which are either always saturated (such as pixels corresponding to high gain and long integration times at low altitudes and in the visible), or alternatively have a low signal (such as pixels corresponding to low gain and low integration times at high altitudes and in the visible). Figure 1-4 and Table 1-3 illustrate a typical Sample Table which fulfills the requirements and constraints elaborated above.

Table 1-3. *Sample Table*

Wavelength range (km)	Altitude range (km)	Useage
290-295	50-60	Ozone
295-300	47-53	Ozone
300-305	43-53	Ozone
305-315	38-45	Ozone
315-325	28-38	Ozone
340-360	whole FOV	RSAS, Straylight
360-500	whole FOV	Straylight
500-520	10-50	Aerosol, albedo
525-675	10-50	Ozone
660-680	10-45	Aerosol, albedo, cloud top
740-750	10-45	Aerosol, albedo, cloud top
840-860	10-45	Aerosol, albedo, cloud top
900-920	10-45	Aerosol, albedo, cloud top
960	10-30	Cloud top
All wavelengths	25, 30	Wavelength registration

1.6 Data Products

The primary and secondary outputs of the OMPS/LP retrieval algorithm are listed in Table 1-4. The primary output is the vertical distribution of ozone covering altitudes from the tropopause to 60 km in 3 km vertical cells reported every 1 km. The secondary outputs are aerosol extinction profiles, one moment of the size distribution (such as Angstrom coefficient or some combination of mean radius and standard deviation), the cloud top height and the effective surface albedo (α). These primary and secondary outputs, together with additional parameters are written in an HDF file, the structure of which is described in Section 3.10.1.

Table 1-4. *OMPS/LP sensor Data products list*

	Vertical range	Vertical spacing	Vertical resolution
Primary product			
Ozone profile	Tropopause – 60 km	1 km	3 km
Secondary products			
Aerosol extinction profile	15-35 km	1 km	3 km
Aerosol size moment	15-35 km	N/A	N/A
Cloud top height	N/A	N/A	N/A
Effective surface albedo	N/A	N/A	N/A

2.0 ALGORITHM OVERVIEW

2.1   Overall concept

The OMPS/LP Algorithm has two major modules:
1. The **Sensor Data Record (SDR)** algorithm, which
    a. processes the weekly solar irradiance data to continuously upgrade the sensor calibration (dead/hot pixels identification, wavelength registration, linearity, dark current magnitude)
    b. preprocesses the Earth view data to generate sets of calibrated and spectrally/spatially registered radiance data
2. The **Environment Data Record (EDR)** algorithm, which retrieves science data from the set of SDR calibrated radiances.

The OMPS/LP mission on NPP will be the first one for this novel sensor. Consequently, together with developing a robust mainstream algorithm which will be capable of processing sensor data at launch time, alternative methods are concurrently being developed both for the SDR and EDR algorithms. The following sections will describe the mainstream algorithms as well as the most pertinent alternatives. For SDR, alternatives have been developed for individual modules, such as the straylight mitigation module, whereas, for the EDR, two alternatives have been developed for the whole EDR algorithm.

To accommodate the EDR mainstream module and its alternatives, the SDR algorithm produces calibrated radiance data in two formats, namely (1) ungridded and (2) gridded. The ungridded data is organized per CCD pixel (i.e., each data point corresponds to a CCD pixel, with its associated calibrated radiance, wavelength and tangent height), whereas the latter dataset uses a two-dimensional cartesian grid (wavelengths vs. tangent height) to remap the radiance data from the original CCD-based format. The mainstream EDR module uses gridded radiance SDR dataset whereas the two alternative EDR algorithms use the ungridded SDR radiance dataset. The mainstream EDR module has heritage from past limb scatter sensors (SOLSE/LORE and SAGE III), and therefore would fulfill the need for an at-launch robust algorithm, whereas the two alternatives are aimed at circumventing the need for data remapping onto a Cartesian grid.

2.2   Overall flowchart

As shown in Figure 2-1, the SDR module reads the OMPS Raw Data Record (RDR) and ancillary data and writes its output into the Hierarchical Data Format (HDF) Sensor Data Record (SDR) file that contains most of the dynamic information needed by the EDR Algorithm. The RDRs are little more than the data packets received directly from the sensor. The EDR algorithm in turn reads the SDR file, together with a series of ancillary files, performs the retrievals of ozone and aerosol profiles and writes its output into the HDF formatted Environmental Data Record (EDR) file. Table 2-1 summarizes the required data input and output files for both the SDR and EDR algorithms.

***Figure* 2-1.** *SDR + EDR flowchart*

Table 2-1. *SDR/EDR input/output files*

Algorithms	Static inputs	Dynamic inputs	Outputs
SDR	CBC, SRG, BPS, FOV, RAD, STB, SLT, LED, IRD, GON, Solar spectrum, Spectroscopy	RDR (HDF) Atmospheric T/P	SDR (HDF) Calibration files Uplink files
EDR	Spectroscopy Solar spectrum BPS, FOV	SDR (HDF)	EDR (HDF) Graphical diagnosis (PNG) Curtain file for orbit Misc diagnosis

A consequence of the Nunn-McCurdy project revision was to minimize the dependence of the OMPS/LP algorithms on external dynamic datasets. Apart from the RDR raw dataset, the SDR+EDR algorithms only require one external dataset, namely the specification of the atmospheric temperature and pressure at the geo-location of each limb scatter events.

2.3 Sensor Data Record (SDR) algorithm

As described in the Algorithm Theoretical Basis Document for the Sensor Data Record *[Jaross et al., 2010]*, the SDR has two main functions, namely sensor calibration and limb data preprocessing. Sensor calibration uses weekly solar irradiance measurements to perform spectral registration of each CCD array pixel, identify bad and "hot" pixels, and assess diffuser degradation. Radiometric calibration, linearity check and calibration trending are also performed. The limb data preprocessing includes: Bias/dark/smear removal, data reformatting, geo-location and viewing angles determination, straylight mitigation, Tangent Height (TH) registration, two-dimensional gridding and gain consolidation. The SDR data processing requires both static and dynamic databases, the former ones include ten pre-launch sensor calibration tables as well as a reference solar spectrum, while the latter ones include the definition of the atmospheric temperature/pressure at the geo-location of each LS event. The SDR error analysis considers measurement errors (sensor SNR), spectral/spatial mis-registration, as well as biases due to gain consolidation and straylight mitigation. Straylight contamination may be a major source of errors in the final ozone profile product, and consequently alternative modules have been developed to

assess and mitigate straylight effects. The output of the SDR algorithm is distributed into a series of three files, namely: a Hierarchal Data Format (HDF) formatted file containing all information required by the EDR algorithm, a calibration database, containing updated information on the sensor characteristics and an uplink file, containing updated information which needs to be periodically uploaded to the space platform.

3.0 ENVIRONMENT DATA RECORD (EDR)

This section describes how ozone profiles are produced from the OMPS/LP UV/Visible/NIR measurements. The algorithm description is presented as a step-by-step processing flow. The modules necessary to convert the SDR calibrated radiance data into ozone and aerosol profiles are then reviewed. In Appendixes A and B, two alternatives methods are described. The first one relies on spectral fitting, while the second one is a Direct Optimal Estimation (DOE) approach applied on the ensemble of downloaded CCD pixels. The spectral fitting method will be helpful in identifying and correcting for instrument effects *[Rault and Taha, 2007],* while the DOE technique circumvents the need for data preprocessing steps such as 2D-gridding, gain consolidation and possibly, straylight mitigation.

3.1 EDR algorithm overview

The EDR algorithm is adapted from the Herman Limb Scattering Algorithm *[Herman et al., 1995a].* This algorithm was employed with the Shuttle Ozone Limb Scatter Experiment (SOLSE) and the Limb Ozone Retrieval Experiment (LORE) *[McPeters et al., 2000; Flittner et al., 2000].* The algorithm basically compares a set of measured normalized scene radiances with the ones calculated using a Radiative Transfer (RT) model for the specific measurement geometry, viewing conditions and surface conditions. The algorithm takes the Instantaneous Field Of View (IFOV) information from the SDR, characterizes the scene (cloud height, surface reflectivity) and performs height registration before aerosol and ozone information is retrieved. The algorithm output is an HDF formatted file containing retrieved products as well as data quality flags and averaging kernel matrices.

The approach chosen for both ozone and aerosol retrievals uses the optimal estimation method *[Rodgers, 1976]*, regulated by a set of *a-priori* constraints, and Section 3.2 describes the application of the optimal estimation to the OMPS/LP retrieval. The forward model, which is used to simulate limb radiances over the OMPS/LP operational spectral and spatial ranges, relies on a pseudo-spherical multiple scattering RT model, and is described in Section 3.3. The retrieval strategy adopted for the OMPS/LP follows a series of sequential steps, as shown in Section 3.4. The goal of the first steps is to check (and modify, if necessary) the CCD array pixels spectral and spatial registrations produced by the SDR, and thus for each limb event and for each of the three slits. The following steps are aimed at specifying the scene viewed by the sensor and yield information on cloud top height and surface reflectance. The last two steps contend with the retrieval of aerosol (extinction coefficient vertical profile and one moment of size distribution), and ozone (density and volume ratio vertical profiles). The algorithms developed for each of these steps are detailed in Section 3.5. The ozone retrieval uses the doublet and triplet methods *[Flittner et al., 2000]* respectively for the Hartley-Huggins and Chappuis bands. The aerosol retrieval uses the methodology described by *[Rault and Loughman, 2007].*

3.2 Application of the optimal estimation method to OMPS/LP

The goal of the retrieval process is to identify the optimal atmospheric composition which most closely reproduces the limb scatter radiances measured by the OMPS/LP sensor, subject to the constraints provided by *a-priori* knowledge of the expected solution. This optimal composition is represented by the state vector *x*, while the measurement vector *y* is constructed using limb radiance observations over a range of tangent heights and wavelengths. A forward model is used to evaluate (a) the limb radiances *F(x)* that OMPS/LP would be expected to observe if the atmospheric state was represented by *x*, and (b) the partial derivatives of radiances with respect to the state vector *x*: $K = \partial F / \partial x$. The optimal estimation technique *[Rodgers, 1976]* is used to iteratively solve for *x*:

$$x_{i+} = \hat{x}_i + \hat{S}_i [K_i^T S_\varepsilon^- (y - F(x_i)) - S_a^- (x_i - x_a)] \qquad \text{[Equation 3.1]}$$

where subscript *i* denotes the ith iteration. Equation 3.1 uses *a-priori* constraints for regularization: x_a is an estimate of the state vector derived from climatology, whereas S_a is the corresponding covariance matrix. The matrix S_ε describes the noise covariance of the measurements. $\hat{S}_i$ is the solution covariance matrix:

$$\hat{S}_i = K_i^T S_\varepsilon^- K_i + S_a^-]^- \qquad \text{[Equation 3.2]}$$

The retrieval 1 σ uncertainty of the state vector is typically given as the square root of the diagonal of the covariance matrix. The criterion for convergence is:

$$(x_i - x_{i+1})^T \hat{S}_i (x_i - x_{i+1}) / n < N_{conv} \qquad \text{[Equation 3.3]}$$

where *n* is the dimension of the state vector and N_{conv} is the convergence threshold. [*Rodgers, 2000*] recommends setting $N_{conv} = 1$, but in practice we have used $N_{conv} = 5$ for ozone retrievals and $N_{conv} = 20$ for aerosol retrievals without significant loss in retrieval accuracy. Convergence is generally obtained within 2-3 iterations, and a maximum of 7 iterations is imposed to prevent runaway calculations when a case does not converge properly.

The kernel matrix *K*, is mathematically defined as the incremental change in the limb radiance signal at a given tangent height *TH* due to an incremental change in the state vector *x(H)* at an altitude *H*. Since the kernels depend on *x*, they must be recalculated at each step of the iterative process. This somewhat CPU intensive task can be minimized since kernels based on single scattering radiances have been shown *[Herman et al., 1995a]* to provide equivalent convergence properties, and analytical forms of the single scattering kernels can be developed for each of the constituents.

Together with profiling and uncertainty information, the averaging kernel matrix *A* is an important diagnosis parameter, since it contains information on the retrieval vertical resolution and the weight of the *a-priori* data.

$$A = \hat{S}_i K_i^T S_\varepsilon^- K_i \qquad \text{[Equation 3.4]}$$

The averaging kernel FWHM is usually taken as a measure of the vertical resolution of the retrieved parameters, since

$$x_{retrieved} = Ax_{truth} + [I - A]x_a \qquad\qquad\qquad \text{[Equation 3.5]}$$

[Rodgers, 2000], where $x_{retrieved}$ represents the retrieved state vector, x_{truth} the actual true state vector, and *I* is the identity matrix. In all retrievals related to the OMPS/LP sensor, the *A* matrix is band-diagonal, with off-diagonal terms (which determine the vertical resolution) rapidly decaying away from the diagonals.

3.3 Radiative Transfer (RT) forward model and Instrument Model (IM)

The retrieval of atmospheric constituents from limb radiance measurements basically involves comparing measured radiances with synthetic radiances generated by a forward model. The analysis of LS measurements therefore requires the use of an accurate and CPU-efficient forward model to simulate the radiative transport through the atmosphere and account for the instrument spectral and spatial characteristics (dispersion, slit function). The forward model consists of two parts, the first one being a multiple scatter, spherical atmosphere Radiative Transfer (RT) model and the second one being a simple Instrument Model (IM).

3.3.1 Radiative Transfer (RT) forward model

The RT model is based on an algorithm developed by *[Herman et al.,1995b]*, and has been specially optimized to run efficiently over a large number of discrete wavelengths [*Rault, 2005a]*, thus allowing one to (1) avoid the use of look-up tables during the retrieval and (2) perform in-line convolution with the sensor slit function. Computational efficiency is maximized by using three imbedded spectral grids:
1. The single scatter computation is performed at a medium grid resolution, illustrated by the blue line in Figure 3-1.
2. The more computationally intensive multiple scattering simulations are made on a much coarser grid. The wavelengths at which multiple scattering calculations are performed in the retrieval algorithm are indicated by vertical pink lines in Figure 3-1.
3. The modeled radiances are then interpolated onto the finer grid of solar irradiance nodes (illustrated by the cyan line in Figure 3-1) before being convolved with the instrument spectral slit function (Section 3.3.2).

The optimal layout of the three grids used in the model was derived by evaluating and minimizing the effect of grid resolution on the retrieved ozone profiles, so that grid-related errors account for a small fraction of the retrieval standard deviation. For comparison, Figure 3-1 also shows the resolution of the ozone cross-sections used in the inversion algorithm (green line), as well as the FWHMs of the OMPS pixels (red line). The partial derivatives with respect to both ozone and aerosol are computed semi-analytically and, due to CPU efficiency considerations, they are not convolved with the instrument slit function, but instead computed at the central wavelength of each pixel.

For the present study, the RT model assumes a Lambertian Earth surface and no atmospheric polarization. The measured signal will be insensitive to the polarization state of the incident radiance because the sensor is equipped with a depolarizer, and neglecting polarization in the RT calculations has little effect on the ozone retrieval *[Loughman et al., 2005]*. The RT model has been compared with other LS RT codes by *[Loughman et al., 2004]*.
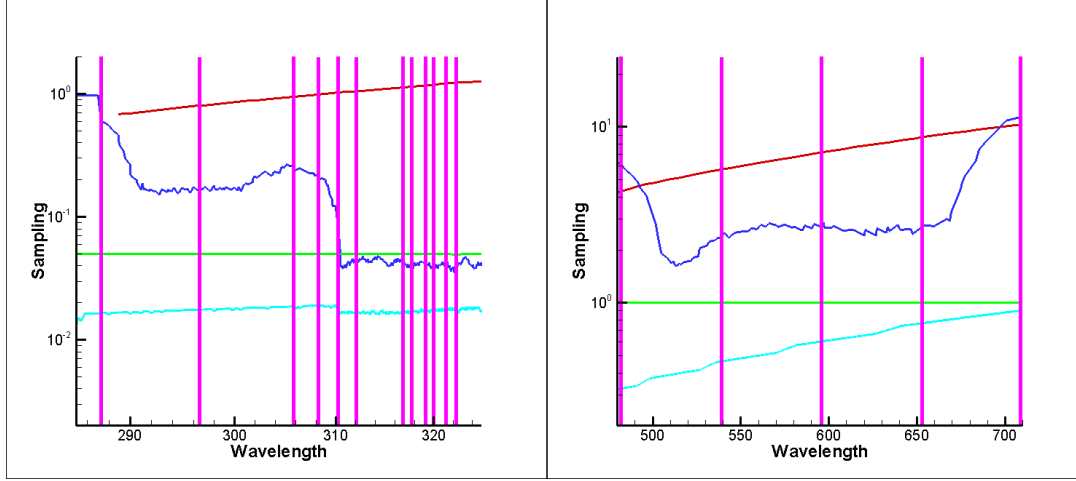
Figure 3-1. *Computational grid sampling (in nm) compared to ozone cross-section sampling (green lines) and OMPS instrument pixel FWHM values (red lines), for UV wavelengths (left panel) and visible wavelengths (right panel). The solar irradiance and single scattering sampling are shown as cyan and blue lines, respectively. Vertical pink lines indicate wavelengths at which multiple scattering calculations are made.*

3.3.2   Instrument Model (IM)

The EDR algorithm uses a simple instrument model in the retrieval process. A more elaborate instrument model, which was constructed to (1) generate synthetic datasets for code testing and (2) perform on-orbit troubleshooting, is described in Appendix C. The basic purpose of the EDR IM is to convolve the high resolution RT computed radiances $i(\lambda, TH)$ with the sensor spectral function $f_{spectral}(\lambda_k, \lambda)$ and spatial response functions $f_{spatial}(TH_k, TH)$. The convolutions are performed sequentially as:

$$I[\lambda, TH_m] = \int i[\lambda_{..}, TH_m] S[\lambda_{..}] f_{spectral}(\lambda_{..}, \lambda) d\lambda_{..} \qquad \text{[Equation 3.6]}$$

where λ_k denotes the RT high resolution spectral grid and $S[\lambda_k]$ is the solar spectrum. TH_m represents the fixed RT spatial grid, which is uniformly spaced with one km resolution. For the spatial convolution, the radiance $I(\lambda, TH_m)$ is first interpolated onto a fine TH_n grid (resolution = 0.1km) and then convolved:

$$Rad[\lambda\ TH] = \int I[\lambda\ TH_n] f_{spatial}(TH_{n,} TH) dTH_n \qquad \text{[Equation 3.7]}$$

The sensor spatial/spectral response functions on each CCD pixel are the combined sensitivity of the optics and CCD detector to an incident light spectrum. They typically are peaked quasi-gaussian functions and have been characterized during pre-launch calibration. The spectral

26

function is defined as a set of 600 points for each active CCD pixel, while the sensor spatial response is defined as a set of 120 points.

3.4   OMPS/LP products retrieval strategy. Overall algorithm layout

[Loughman et al. 2005] and [Rault and Taha, 2007] have shown that the ozone profile retrieval from LS measurements is sensitive to a series of parameters, including: the accuracy of spectral and spatial registrations, aerosol density, and to a lesser extent, surface reflectivity α and NO_2 density. The accuracy/precision requirements expected out of the OMPS/LP demand that these parameters be known to a relatively high accuracy. The SDR algorithm provides calibrated radiances for each CCD pixel, each one registered both spectrally (using weekly solar measurements) and spatially (using spacecraft position and attitude information). However, the accuracy of these registrations needs to be verified and, if necessary, corrected, as the first step of the retrieval process. Aerosol density and α may vary in time and space due to dust transport and cloud/land-cover respectively. The NO_2 density varies both spatially and in local solar time.

To account for these effects, the retrieval strategy adopted for the OMPS/LP ozone profile retrieval includes the following steps:

(1) First order estimation of NO_2 from climatology, corrected for local solar time effects
(2) TH registration check, and adjustment if necessary, using a scene-base method, such as the Rayleigh Scatter Attitude Sensor (RSAS) technique *[Janz et al. 1996]* or alternatively, the Multiple Wavelengths TH Registration Method *[Rault, 2006]*
(3) Cloud height determination, using long wavelength channels with weak gaseous absorption
(4) Surface albedo determination
(5) Aerosol retrieval (aerosol extinction and size distribution), using spectral channels with weak gaseous absorption
(6) Repeat TH registration check/adjustment. RSAS TH registration is sensitive to stratospheric aerosol content
(7) Ozone retrieval, using radiance data from both the UltraViolet and visible wavelength channels, respectively for high altitudes (30-60km) and low altitudes (Cloud top or 10km-40km)
(8) Residuals evaluation

These steps are mostly independent from each other, since each step is using a different part of the spectral range measured by OMPS/LP. The order of these steps is specifically designed to provide rapid ozone convergence by ensuring the ozone inversion is using the best estimates for all pertinent atmospheric and surface parameters. The steps are mostly sequential with very little reliance on iterative return loop in order to minimize CPU requirements.

The outputs of the EDR algorithm are the vertical distribution of ozone in the altitude range tropopause-60 km as well as by-products such as stratospheric aerosol vertical distribution and some information on aerosol size, α and cloud top height. The uncertainty estimates obtained for both ozone density and height registration are also included.

3.5   OMPS/LP product retrieval

3.5.1   Spectral registration

The UV solar and ozone absorption spectra both exhibit rich fine structures with rapidly varying features. Consequently, high ozone retrieval accuracy in the UV spectral range critically depends on high quality spectral registration. Each limb observation made by the OMPS/LP must therefore first pass a quality test with respect to spectral registration, in addition to the weekly solar-diffuser-based registration performed by the SDR. For that purpose, a series of CCD pixels are selected and downlinked to help characterize a critical region of the CCD image of each slit for each of the two apertures. Figure 3-2 shows a typical configuration, namely a "row" of pixels corresponding to a tangent height of 25 km in the low gain image and 30 km in the high gain image. To check spectral registration accuracy, the limb observations along these rows of pixels are compared with the radiance values computed by the forward model, using the SDR spectral registration to set the center wavelength of each CCD pixel in the instrument model. The measured and modeled data spectra are first both filtered with a low-frequency filter to obtain the high frequency spectra $D(\lambda)$ and $M(\lambda)$ respectively for the measured and modeled radiances. The wavelength scale shift $\Delta\lambda$ is identified by optimizing the correlation between $D(\lambda)$ and $M(\lambda+\Delta\lambda)$. An estimate of the wavelength scale stretch is obtained by using sub-intervals over which individual $\Delta\lambda$ are computed.
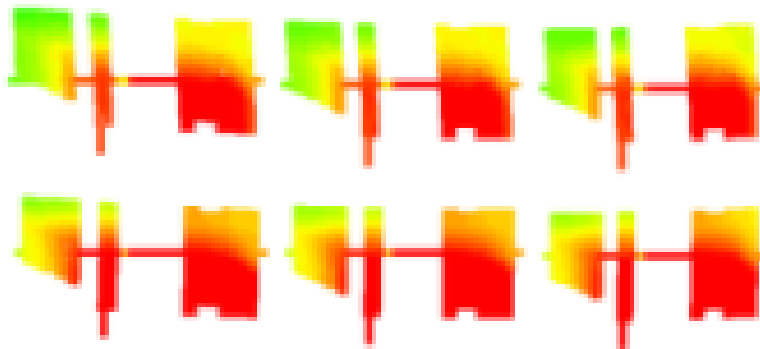
Figure 3-2. *Typical Sample Table of downlinked CCD pixels. Each colored area represents sets of downloaded pixels. Long horizontal rows of pixels are used for wavelength registration. Long column of pixels are used for TH registration.*

3.5.2   Tangent height registration

The SDR provides a height registration for each downlinked CCD pixels using (1) spacecraft position/attitude and Earth's radius data, and (2) laboratory measured angle offsets with respect to boresight. Pointing errors may lead to large uncertainties on TH registration for limb viewing sensors. For OMPS/LP, 1 arcminute pointing offset corresponds to 1 km error in tangent height. Two methods will be used to check and correct tangent height registration, namely the Rayleigh Scatter Altimeter Sensor (RSAS) technique [*Janz et al. 1996*] and the Multiple Wavelengths TH Registration Method *[Rault, 2006]*

3.5.2.1   Rayleigh Scattering Attitude Sensor (RSAS)

The RSAS method considers the non-absorbing spectral region between the ozone Huggins and Chappuis bands, around 350 nm, where Rayleigh scattering is the prime mechanism to redirect light to the LS sensor. Basically, the RSAS technique compares the measured data to the modeled radiances, with special weight being given to a TH range around a singularity point, namely the Maximum Curvature Point (MCP).

In the neighborhood of this point, the limb radiance transitions from the optically thin regime (exponential relationship between radiance and altitude) to the optically thick regime (radiance changes little with altitude and can be said to be saturated).   The outcome of the RSAS technique is a single TH shift parameter *ΔTH* which is used to correct the TH registration for all data points. *[Rault and Taha, 2007]* have shown that the accuracy of the technique critically depends on the accuracy of the atmospheric temperature/pressure profiles assumed in the forward model. Over a large ensemble of SAGE III LS measurements, RSAS was demonstrated to have negligible bias and a standard deviation of 350 m using NCEP temperature/pressure profiles. Since the MCP point typically lies in the 20-30km range, i.e., within the stratospheric aerosol layer, RSAS accuracy critically depends on the knowledge of the aerosol distribution in that altitude range. RSAS must therefore be performed at least twice during the retrieval, first in the initial processing phase for coarse registration (assuming climatological values for aerosol content) and then to fine tune tangent heights after aerosol retrieval. The first phase is performed on the CCD pixel map, using columns of pixels with wavelengths close to 350 nm, as shown in Figure 3-2. The second phase, which is using retrieved aerosol information, is performed on gridded data, just before ozone retrieval.

3.5.2.2   Multiple Wavelengths TH Registration Method

This technique uses the same principles as the RSAS technique, albeit over a wider spectral range. A set of TH shift parameters *ΔTH(λ)* is computed for each wavelength λ over a spectral range which typically extends from 310 nm to 500nm. Since the location of the MCP point varies as a function of wavelengths, (mostly decreasing in altitude with increasing wavelengths), this technique provides information on the variation of *ΔTH* with altitude. The spectral range of applicability of this technique is limited by the height of the MCP, which is required to remain in the stratosphere. *[Rault, 2006]*

3.5.3   Cloud height

The OMPS/LP long wavelength channels are sensitive to the presence of clouds. Clouds appear as either faint or sharp discontinuities of the radiance vertical profiles, whether they correspond to thin cirrus or tropospheric water clouds (Figure 3-3). Limb observations are particularly useful for detecting optically thin clouds that might go undetected by nadir sensors *[Wang et al., 1994]*. By its nature, the cloud detection algorithm must detect abrupt changes in the radiance profile. Since these sharp features must necessarily be dulled by the gridding and gain consolidation processes, the cloud detection algorithm is more effective when applied to radiances prior to gridding and gain consolidation.   The algorithm operates on a set of columns of CCD pixels, positioned at long wavelengths, as shown in Figure 3-2.

Polar Stratospheric and Mesospheric Clouds (PSC and PMC) can also be detected with LS signal *[von Savigny, 2005, Petelina, 2006]*. PSCs appear as somewhat broad features in the stratosphere. The current aerosol algorithm will treat a PSC as part of the stratospheric aerosol load, but in the future a PSC detection method will be developed (based on the spectrally flat

PSC scattering and the characteristic temperature at which PSCs are known to form). PMCs appear as enhanced scattering layers near 80 km. PMCs may unfortunately occur outside of the OMPS/LP field of view which nominally extends from Earth surface to 65 km. The LS line of sight will undoubtedly pass through PMCs, but characterization of PMCs from OMPS/LP measurements will be difficult with few observations for which the PMC occurs near the tangent point of the line of sight. Other datasets such as Aeronomy of Ice in the Mesosphere (AIM) / Solar Occultation For Ice Experiment (SOFIE) *[Russell et al., 2008]* will be used to help identify PMC presence within the OMPS/LP field-of-view and (1) mark them as a quality flag and (2) ascertain their effect on ozone retrieval.
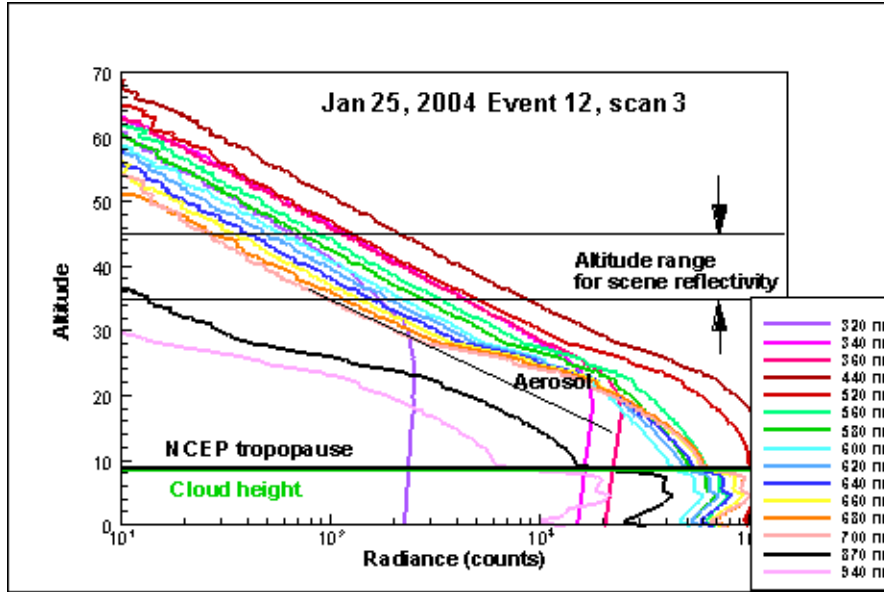
Figure 3-3. *SAGE III LS vertical radiance profile. Tropospheric clouds appear as sharp discontinuities. Stratospheric aerosol and PSCs appear as broad scattering features. Color profiles correspond to a series of wavelengths from 320 to 940 nm*

3.5.4 Surface albedo

The aerosol retrieval is conducted using a series of spectral channels which exhibit minimal gaseous absorption, namely in the following ranges: 480-510nm, 660-680 nm, 740-750 nm, 840-860 nm and 900-920 nm. The basic scheme in the aerosol retrieval algorithm is to identify and quantify the additional scattering which occurs beyond Rayleigh scattering. The first step, therefore, is to evaluate the Rayleigh scatter signal, which, in the visible/InfraRed spectral range, is a complex function of Earth surface reflectance and also involves multiple scatter effects. The Rayleigh scatter signal, however, can be estimated by comparing measured data to model radiances at high altitudes to estimate an effective surface albedo α, which can then be used to evaluate the Rayleigh component at all altitudes. The retrieved α is also used subsequently in the ozone retrieval algorithm.

In the forward model, the Earth surface is assumed to be Lambertian and homogeneous, with only one independent variable, namely its spectral dependence $\alpha(\lambda)$. To estimate $\alpha(\lambda)$ from limb observations, the measured data is compared to model radiances in the TH range of 35-45 km. This TH range is located mostly above the aerosol layer and should be minimally contaminated

by straylight. For each wavelength considered, the measured LS radiance is compared with model radiances computed at three assumed surface reflectances, namely, 0.1, 0.5 and 0.9, and $\alpha(\lambda)$ is subsequently evaluated by interpolation. Given absolute radiometric calibration of the instrument at the intended level (2%), this method yields $\alpha(\lambda)$ at sufficient accuracy (<10%) to allow accurate retrieval of trace gases and aerosol. This method is most applicable to visible and InfraRed wavelengths, since UV limb radiance sensitivity to Earth surface reflectance rapidly decreases with decreasing wavelengths.

3.5.5 Aerosol retrieval

Figure 3-4 shows typical LS radiance profiles normalized to the Rayleigh scatter signal computed using the retrieved α. The signature of stratospheric aerosols is clearly evident from 10 to 30 km. Results are shown for a series of wavelengths ranging from 449 to 800 nm. The rapidly increasing values of normalized radiances with wavelengths are primarily due to the increasing sensitivity of the LS radiance to aerosol at higher wavelengths, which is shown in Figure 3-5.
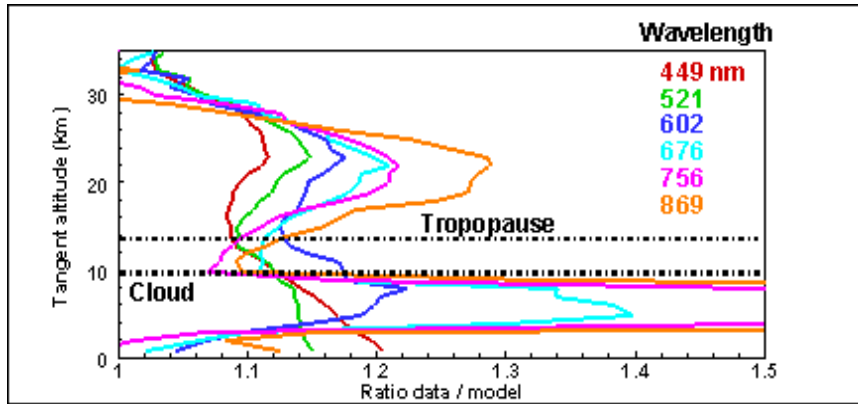
Figure 3-4. *The ratio of the measured LS radiance to the model radiances calculated for an aerosol-free atmosphere at the derived effective Lambertian surface reflectivity α(λ). A cloud can also be observed at 10km, just below the tropopause. [Rault and Loughman, 2007]*
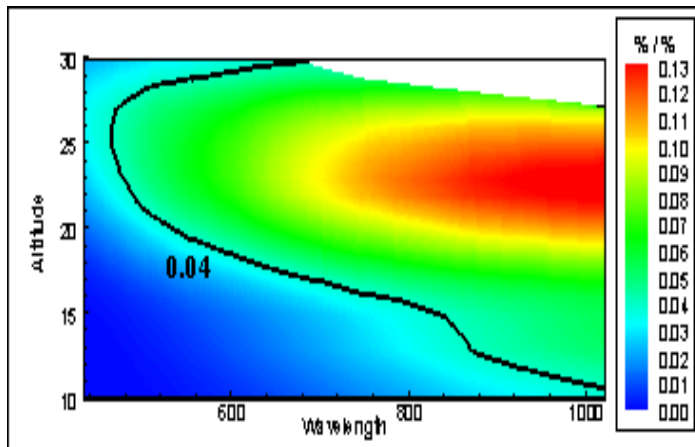
Figure 3-5. *Sensitivity of limb radiance to stratospheric aerosol. Sensitivity is defined as the maximum change [%] of limb radiance due to 1 percent change in aerosol extinction. Aerosol retrieval is not attempted in the region corresponding to sensitivities lower than 0.04.*

3.5.5.1 Aerosol extinction coefficient

For the retrieval of aerosol extinction coefficients, the measurement vector is:

$$y = I[\lambda, TH] / I[\lambda, TH_{NORM}] \qquad for \quad TH_{min} < TH < TH_{max} \qquad \text{[Equation 3.8]}$$

where $I[\lambda, TH]$ is the limb radiance at wavelength λ and tangent TH. TH_{NORM} is the tangent height selected for normalization. The high altitude normalization greatly reduces the effects of parameters such as surface/cloud reflectance, sensor absolute calibration and sensor residual polarization. The normalization altitude for aerosol retrieval is around 40 km, but may vary during on-orbit operations depending on aerosol loading. TH_{min} and TH_{max} represent the altitude range beyond which the radiance sensitivity to aerosol is too low for a successful retrieval. These parameters depend on wavelength, viewing conditions and aerosol loading, but are typically around 15 and 35 km respectively.

The *a-priori* vector is a set of extinction vertical profiles derived from SAGE III occultation measurements. These values correspond to the present period of low stratospheric background aerosol. The partial derivatives of LS radiances with respect to aerosol extinction are evaluated using analytic partial derivatives of the numerical integration employed in the RT. In this step the key assumption is that the source function due to multiple scattering is independent of small changes in stratospheric aerosol concentration.

The aerosol retrieval is performed independently for each wavelength. Once converged, the spectral dependence of the extinction coefficients is then used to infer information on the aerosol size distribution, as described in the next section. The inferred size distribution parameter is then used to evaluate the extinction coefficients at the wavelengths selected for ozone retrieval. This task is alternatively done in one of two ways:
1. Using the Angstrom coefficient that best fits the retrieved aerosol extinction
2. Using Mie theory for the retrieved aerosol size distribution to interpolate between the retrieved aerosol extinction values.

In either method, the key point is that the aerosol extinction coefficients $\beta(\lambda)$ are smooth functions of wavelength λ and therefore do not introduce spurious, non-physical, high frequency fluctuations into the ozone retrieval process.

3.5.5.2 Size distribution parameters

Inverted aerosol is reported in terms of extinction/km. However, the RT code requires additional knowledge of the aerosol characteristics such as particle size distribution, particle composition, and refractive indices. While default values corresponding to background aerosols can be used for most observing conditions, the spectral dependence of the extinction coefficients contains some information on aerosol microphysics which can be extracted as was done in the SAGE missions *[Yue, 2000]*.

Assuming the aerosols to be an ensemble of Mie scattering spherical particles with a known index of refraction and a single mode log normal size distribution, *[Yue, 2000]* has demonstrated that the extinction coefficients $\beta(\lambda, TH)$ retrieved from SAGE solar occultation observations contain the necessary information to derive the mean radius r_{mean} and the variance σ. However, due mainly to the relatively narrow spectral band over which $\beta_i (\lambda, TH)$ is derived with LS data, r_{mean} and σ cannot be independently evaluated from OMPS/LP data. Instead one can infer only one independent parameter, such as either a mean Angstrom coefficients or one moment of the

size distribution. To infer aerosol size information from the spectral dependence of the extinction coefficient $\tau(\lambda,TH)$, a series of steps are taken:

(1) A cost function is defined as:

$$\chi[R_{mean},\sigma,TH] = \sum \left[ColorRatio(\lambda,\lambda_0,TH) - ColorRatio_{MIE}(\lambda,\lambda_0,R_{mean},\sigma) \right]^2$$

[Equation 3.9]

where $ColorRatio(\lambda,\lambda_0,TH) = \beta(\lambda,TH)/\beta(\lambda_0,TH)$ evaluated with a reference wavelength λ_0 and $ColorRatio_{MIE}(\lambda,\lambda_0,R_{mean},\sigma)$ is the equivalent color ratio computed with the Mie theory for a given (R_{mean},σ) pair.

(2) Values of (R_{mean},σ) pairs which minimize the cost function $\chi[TH]$ are identified, and the minimal value recorded as χ_0.

(3) Values of (R_{mean},σ) pairs for which $\chi[R_{mean},\sigma,TH] < 2\chi_0$ are identified, as illustrated in Figure 3-6. In principle, all these points are possible solutions, as they produce similar aerosol extinction spectral characteristics.

(4) The (R_{mean},σ) pair closest to the initial set is selected as the solution. The rationale for this selection is that the initial guess, which is based on updated climatology, was probably close to the actual value. Again, this point selection does not affect the aerosol extinction characteristics since all the points with $\chi < 2\chi_0$ would lead to nearly the same result.

This 4-step procedure is repeated for each tangent height *TH*, then averaged together over the altitude range with significant aerosol sensitivity to produce a single aerosol size distribution that best fits the data.
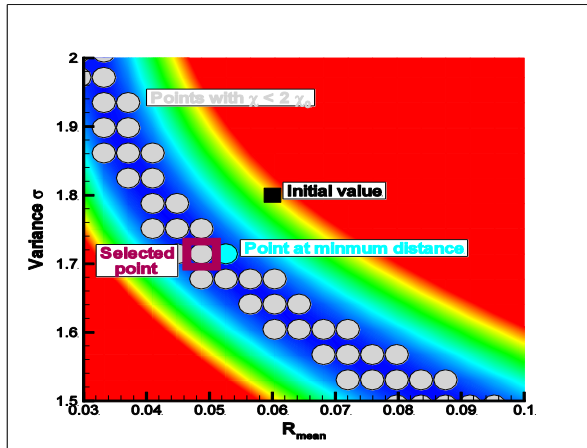
Figure 3-6. *Cost function minima to retrieve moment of size distribution*

3.5.6   Ozone profile retrieval

To retrieve ozone information from LS radiance over the altitude range 15-60 km, a series of spectral channels is selected to observe a range of weakly to strongly absorbing features in the Hartley-Huggins and Chappuis ozone bands, thus allowing one to retrieve ozone at progressively higher levels in the atmosphere. *Figure 3-7* illustrates how the sensitivity of the limb radiance $I(\lambda,TH)$ at λ = 305 and 600 nm varies with the altitude of the ozone perturbation z at various

33

tangent heights *TH*. The curves in *Figure 3-7* are sharply peaked, because *I(λ,TH)* is typically most sensitive to ozone perturbations at the altitude *z = TH*. Figure 3-8 illustrates how the sensitivity of the LS radiance to ozone density varies with *λ* in the Hartley-Huggins and Chappuis bands when *z = TH*. UltraViolet channels can be used to retrieve ozone from 30 to 60 km, while the visible channels can be used from 15 to 40 km. Due to algorithm instabilities in the 30-40 km overlap region (lower sensitivities to ozone may yield to noise amplification) and sensor design issues (UltraViolet and visible channels are recorded on CCD regions which may be widely separated in space), the data processing strategy is to separately retrieve two ozone profiles, namely a high altitude profile from UV data and a low altitude profile from visible wavelengths. The difference between these two profiles within the overlap region 30-40 km is used as a quality flag of the retrieval.
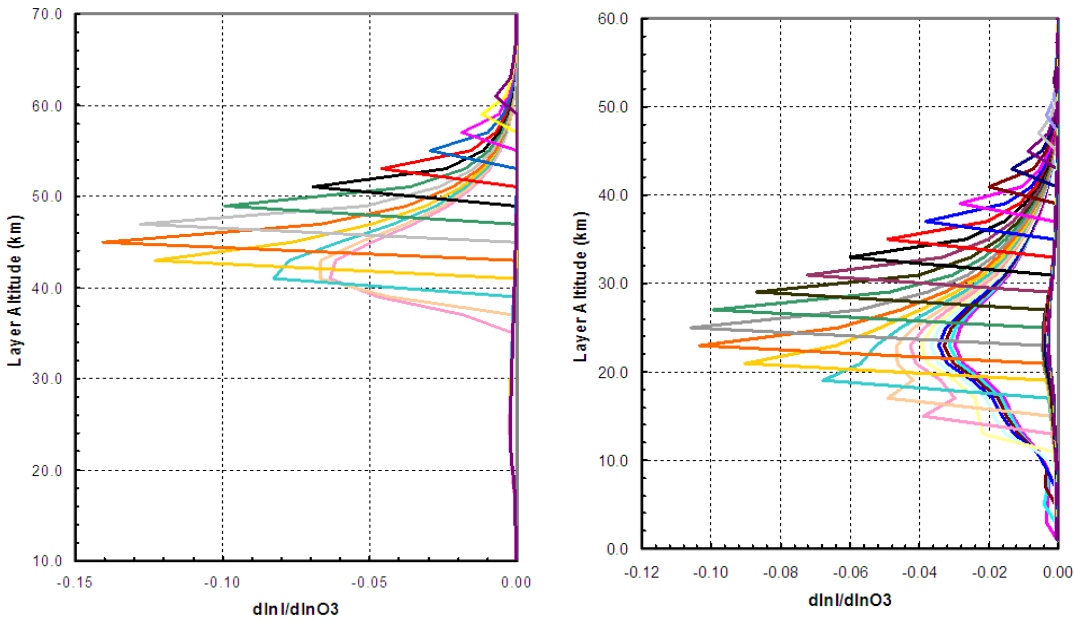
Figure 3-7. *Relative sensitivity of radiance at 305 nm (left panel) and 600 nm (right panel) to ozone perturbations. Each curve shows the sensitivity of the radiance at a given tangent height to ozone perturbations of a 1-km layer at a range of altitudes.*
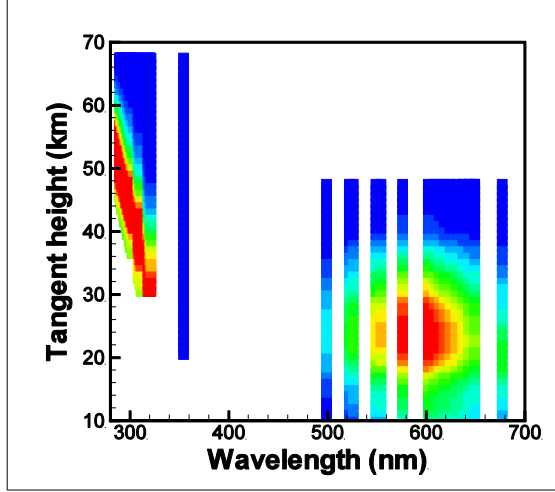
Figure 3-8. *Sensitivity of limb radiance to ozone. Sensitivity is defined as the maximum change [%] of limb radiance due to 1% change in ozone density. Results are shown for a typical set of OMPS/LP wavelengths*

3.5.6.1 Doublet and Triplet formulation

For ozone retrieval, the measurement vector is made of wavelength pairs (or doublets) in the UV, and triplets in the visible, following the technique described by *[Flittner et al., 2000]*. In effect, this technique (1) normalizes limb radiance measurements to high altitude radiances and (2) contrasts strongly absorbing channels with weakly absorbing ones:

$$y = \log\left\{\left(\frac{I(\lambda, TH)}{I(\lambda, TH_{NORM})}\right) \Big/ \left(\frac{I(\lambda_-, TH)}{I(\lambda_-, TH_{NORM})}\right)\right\} \qquad \text{[Equation 3.10]}$$

$$y = \log\left\{\left(\frac{I(\lambda, TH)}{I(\lambda, TH_{NORM})}\right) \Big/ \left[\left(\frac{I(\lambda_-, TH)}{I(\lambda_-, TH_{NORM})}\right)^{\omega}\left(\frac{I(\lambda_{--}, TH)}{I(\lambda_-, TH_{NORM})}\right)^{\omega}\right]\right\}, \qquad \text{[Equation 3.11]}$$

where *I(λ,TH)* represents the limb radiance at wavelength λ and tangent height *TH*. TH_{NORM} is the reference tangent height used for normalization. The wavelengths λ_0, λ_L and λ_R represent weakly absorbing channels which serve as references in the doublet and triplet, respectively. The weight factors ω_L and ω_R are computed as:

$$\omega_- = \frac{(\lambda_{--} - \lambda)}{(\lambda_- - \lambda)} \qquad and \qquad \omega_{--} = 1 - \omega_-\qquad \text{[Equation 3.12]}$$

The high altitude normalization greatly reduces the effects of parameters such as surface/cloud reflectance, sensor absolute calibration and sensor residual polarization. The normalization altitude selected for the Hartley/Huggins and Chappuis bands are about 62 km and 45 km

35

respectively. The triplet formulation is effective in providing a linear aerosol correction throughout the Chappuis band.

For OMPS/LP, in order to increase the Signal-to-Noise Ratio (SNR) of the measurement vector y, two modifications to the standard Doublet/Triplet technique have been implemented: (1) the normalization is not done at TH_{NORM}, but instead over an altitude range from $TH_{NORM}-\Delta H$ to $TH_{NORM}+\Delta H$, with ΔH=6km, and (2) the reference channels are not at the discrete $\lambda_0, \lambda_L, \lambda_R$, but instead include all available channels at $\lambda_0\pm\Delta\lambda, \lambda_L\pm\Delta\lambda, \lambda_R\pm\Delta\lambda$, with $\Delta\lambda$=10nm. Table 3-1 gives typical values for TH_{NORM} and $\lambda_0, \lambda_L, \lambda_R$ for both the doublet and triplet constructions. From their definition, the doublet/triplet measurement vectors can be seen to be mostly insensitive to errors in absolute radiometric calibration. Moreover, these vectors have a lower sensitivity to a series of parameters (such as α and aerosol content) than the absolute radiances $I(\lambda,TH)$ *[Loughman et al., 2005]*.

Table 3-1. *Parameters for Doublet/Triplet construction*

Parameters	Values
TH_{NORM} (Doublet)	65 km
TH_{NORM} (Triplet)	45 km
Doublet λ_0	355 nm
Triplet λ_L	500 nm
Triplet λ_R	680 nm
Wavelengths used in UV (nm)	289.3 289.8 290.3 290.9 291.4 292.0 293.1 293.6 294.2 294.7 295.2 295.8 296.5 297.0 297.6 298.2 298.8 299.4 300.0 300.6 301.2 301.8 302.4 303.0 308.9 309.5 310.1 310.8 311.6 318.0 318.7 319.4 320.2 320.9 321.7
Wavelengths used in visible (nm)	522.8 526.3 549.9 554.3 572.1 576.9 602.5 608.1 613.4 619.624.8 630.9 637.4 643.4 649.7

The *a-priori* ozone profile vector is obtained from SAGE II climatology *[Anderson., 1997]* and is stored as a function of latitude and calendar month. The *a-priori* covariance matrix is diagonal and each element corresponds to a 100% uncertainty on *a-priori* density.
For both the doublet and the triplet formulations, the averaging kernel matrix is mostly diagonal with most of the diagonal terms being close to unity. Hence the derived ozone profile depends little on a-*priori* values over most of retrieval altitude range.
The radiance data "measurements" produced by the SDR algorithm are in fact the result of a series of data manipulation steps, the last two being 2D-gridding and four-gain consolidation. The 2D-gridding process allows one to map the CCD pixel coordinates [λ_i, TH_i for each pixel *i*] onto a single uniform two-dimensional [λ, TH] Cartesian grid. The gain consolidation process allows one to merge the four gain images (two apertures and two integration times) onto a single radiance profile. In effect, the "measurements" M_{SDR} produced by the SDR are related to the actual data D_{CCD} recorded on each [λ_i, TH_i] CCD as follows:

$$M_{SDR}[\lambda\ TH] = \sum_{4\,gains} weight_{gain} \{ \sum_{4.CCD.pixels} D_{CCD}[\lambda.\ TH_i].weight_{gridding}[\lambda.\ TH_i]\}$$

[Equation 3.13]

The inner summation corresponds to the bilinear gridding used to map CCD pixel data onto the uniform Cartesian grid while the outer summation refers to gain consolidation.

The 2D-gridding and gain consolidation processes may alter the measurement uncertainties and effective slit function associated with each measurement in an unknown fashion, which may then increase retrieval errors and biases. To alleviate this problem, the OMPS/LP forward model data is processed in a manner similar to the actual data, that is, the model is run at the actual $[\lambda_i, TH_i]$ of each downlinked CCD pixels, and then recombined using Equation 3.13 to map the model values onto the two-dimensional $[\lambda, TH]$ Cartesian grid, using the same weight factors derived for the data.

3.5.7   Conversion of ozone density to ozone mixing ratio

The radiative transfer model and the retrieval algorithm use number density to specify ozone levels. However, the standard NPOESS System Specification product requires that ozone be reported in terms of volume mixing ratio. The neutral number density profile, derived from the National Center for Environmental Prediction (NCEP) temperature/pressure data, is used to convert the ozone profile from number density to volume mixing ratio.

3.5.8   Residual analysis

Upon completion of the ozone and aerosol retrieval process, the forward model is rerun using all the retrieved parameters for all spectral channels downlinked from the OMPS/LP sensor. The reconstructed signal is then compared to the actual limb radiance measurements to identify biases in (1) the radiance vertical profiles for each spectral channel and (2) the spectral profiles at each tangent height. Analysis of these residuals will allow one to detect systematic errors due either to algorithm issues or unaccounted instrument effects. Some of these residuals will be stored as quality flags.

3.6   Assumptions

The assumptions contained in the algorithm are summarized in Table 3-2.

Table 3-2. *Assumptions made in the EDR algorithm*

Forward Model
The atmosphere's lower boundary is Lambertian
The surface reflectance is spatially uniform
Atmospheric constituents only vary in the vertical direction
Retrieval
The limb radiance can be treated as coming from a point source with viewing conditions given at the center of the pixel IFOV
Aerosol size distribution is single mode log normal. Aerosol particles are Mie scattering liquid sulfate spherical particles with an index of refraction *m=1.448+0i.*
Diffuse radiation field solution on tangent point zenith applicable at all points along line of sight
Ozone and NO_2 absorption, aerosol scattering, and Rayleigh scattering are the only physical processes occurring in the OMPS channels

3.7 External dynamic data

Both the aerosol and ozone retrievals require a set of *a-priori* constraints. For aerosol, a SAGE III climatology *[Thomason, 1997]* is used to set up two sets of vertical aerosol extinction profiles which are interchangeably used for all retrievals regardless of geo-locations or seasons. In the first set, the extinction coefficient spectral dependence is consistent with a mean Angstrom coefficient of 2.5, while in the second set, the spectral dependence is consistent with a log-normal uni-modal size distribution with a mean radius of 0.06 μm and a variance of 1.73.

The NO_2 density vertical distribution is not currently retrieved in the baseline OMPS/LP algorithm. The ozone retrieval relies on one of two NO_2 climatologies:

1) A climatology based on the HALogen Occultation Experiment (HALOE) NO_2 retrievals *[Gordley et al., 1996],* enhanced by multiple linear regression analysis to create a complete climatology, including the Quasi-Biennial Oscillation (QBO), seasonal effects, etc. *[Anderson, 2002]*. The HALOE climatology is not corrected for local time and corresponds to either Sunrise or Sunset conditions.

2) A climatology constructed using the PRATMO photochemical box model *[McLinden, 2000],* which explicitly includes local time effects.

The atmospheric temperature and pressure profiles at the geo-location of the OMPS/LP events are obtained by interpolation (bilinear in space, linear in time) of the profiles provided by the National Center for Environmental Prediction (NCEP) *[Kalnay et al., 1996]*. NCEP generates global maps of atmospheric temperature and geometric heights for a set of 21 pressure levels (1000, 850, 700, 500, 400, 300, 250, 200, 150, 100, 70, 50, 40, 30, 20, 15, 10, 5, 2, 1, 0.4 mb) on a 1° by 1° longitude/latitude grid, four times daily (at 0, 6, 12, 18 GMT).

3.8 Databases

The RT model uses:

- ozone cross sections (with their temperature dependency) compiled by *[Bass and Paur, 1984]* and [*Burkholder and Talukdar, 1994]*. Alternatively, the RT is setup to use absorption cross sections measured by *[Bogumil et al, 2003]*, *[Brion et al., 1998]*, *[Malicet et al., 1995]* and *[Daumont et al., 1992]*.
- NO_2 cross sections measured by *[Harder et al., 1997]*.
- Rayleigh scattering cross-sections and anisotropy measured by *[Bates, 1984]*.
- Solar spectra compiled by *[Rothman et al., 1992]*, *[Colina et al., 1996]* and *[Kurucz, 2005]*.

3.9 EDR error analysis

The retrieval uncertainties intrinsic to the EDR algorithm may originate from either random noise (which modulates both the SDR radiance data and the NCEP temperature profiles) or from offset biases (introduced either in spectroscopic data or at some stage of the retrieval process). The effect of radiance measurement noise on ozone retrieval can be readily estimated from the optimal estimation covariance matrix. Some of the other effects can be quantified by passing a large ensemble of synthetic radiances through the EDR algorithm and perform a statistical analysis of the retrieved products. Section 4.0 describes this testing process, whereby a series of 450 synthetic LS events simulated with the forward model is used. Each LS event within the

dataset corresponds to a co-location of a SAGE II occultation measurement with a SCIAMACHY limb scattering measurement over a one-year period. These events encompass a wide range of geo-locations, seasons and solar viewing angles. The "true" ozone profile for each event is assumed to be the SAGE II retrieved ozone product, whereas the solar view angles are obtained from the SCIAMACHY measurements. For all events, the forward model simulation assumes a uniform surface albedo and a constant aerosol extinction profile typical of present background conditions. Figure 3-9 presents the results of the ozone retrieval in terms of mean bias and standard deviation. Both the Hartley-Huggins and Chappuis retrievals have accuracy better than 1% in the 20-58 km range. The standard deviation is also about 1% over the same altitude range. These results were obtained in spite of retrieval error on surface albedo (up to 20%) and uncertainties on aerosol extinction (amounting to 5% in mean bias and 10% in standard deviation). Further details of the analysis can be found in Section 4.0.

Systematic errors due to uncertainties on spectroscopy (ozone and NO_2), Rayleigh cross sections, NO_2 density, solar spectrum and air density profile can also be ascertained with this methodology and the 450 LS events dataset.
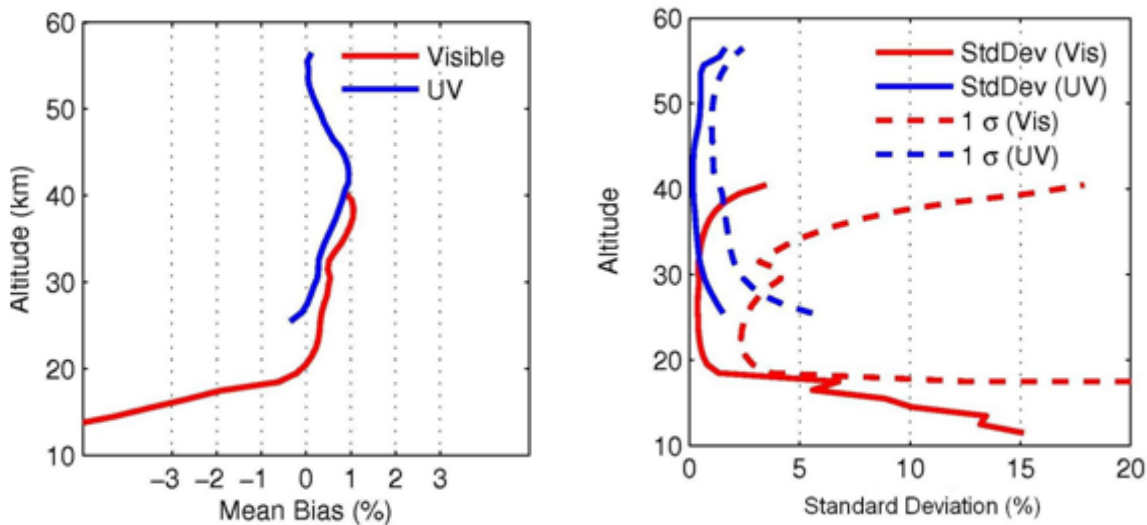
Figure 3-9. Summary plot of the percent difference for all retrieved ozone profiles for the 450 simulated radiances, red is for visible, and blue is for UV retrievals. The left panel shows the mean bias, while the right panel shows the ensemble standard deviation, with dash lines representing the retrieval 1-σ uncertainty

3.10 EDR output data file format and content

The EDR algorithm generates its output in two different ways:

- an HDF formatted file which will contain all retrieved products as well as additional parameters such as input parameters (atmospheric temperature and pressure profiles, *a-priori* constraints) and derived parameters (averaging kernels)
- a diagnosis file which visually displays information on the ozone and aerosol retrieval process

On the OMPS/LP website, the output files for individual limb events will be consolidated on a per-orbit basis resulting in one HDF file containing all results for all events (and all three slits) occurring on a given orbit, and three diagnosis files, each one containing diagnostics information for a full orbit for each of the 3 slits (see Figure 3-10). Curtain files will also be constructed to display the ozone profile information along the orbit, and thus for each of the three slits (see Figure 3-11).

3.10.1 EDR HDF data file (structure and fields definition)

The EDR HDF file will be composed of two core groups (GEOLOCATION and DATA), each one being subdivided into a series of fields. Table 3-3 shows the major components of the DATA group

Table 3-3. *EDR HDF file content*

Data Fields	
AveKernel_O3UV	Averaging kernel matrix for ozone UV
AveKernel_O3Vis	Averaging kernel matrix for ozone Visible
AveKernel_aer	Averaging kernel matrix for aerosol
HT0	Retrieval altitude grid (km)
O3CombinedL2gpPrecision	Combined ozone profile uncertainty [m^{-3}]
O3CombinedL2gpValue	UV+Vis Combined ozone profile [m^{-3}]
O3CombinedQuality	Quality flag for Combined ozone profile
O3UvConvergence	Retrieved UV ozone Convergence
O3UvL2gpPrecision	Retrieved UV ozone uncertainty [m^{-3}]
O3UvL2gpValue	Retrieved UV ozone vertical profile [m^{-3}]
O3UvQuality	Retrieved UV ozone Quality flag
O3UvStatus	Retrieved UV ozone. Number of iterations
O3VisConvergence	Retrieved Chappuis ozone Convergence
O3VisL2gpPrecision	Retrieved Chappuis ozone uncertainty [m^{-3}]
O3VisL2gpValue	Retrieved Chappuis ozone vertical profile [m^{-3}]
O3VisQuality	Retrieved Chappuis ozone Quality flag
O3VisStatus	Retrieved Chappuis ozone. Number of iterations
O3VmrCombinedL2gpPrecision	Ozone Volume Mixing Ratio uncertainty
O3VmrCombinedL2gpValue	Ozone Volume Mixing Ratio
O3VmrCombinedQuality	Ozone Volume Mixing Ratio Quality flag
HT_AerosolBottom	Retrieved TH bottom for aerosol [km]
HT_AerosolTop	Retrieved TH top for aerosol [km]
HT_HugginsBottom	Retrieved bottom height for Huggins Ozone [km]
HT_HugginsTop	Retrieved top height for Huggins Ozone [km]
HT_ChappuisBottom	Retrieved bottom height. Chappuis Ozone[km]
HT_ChappuisTop	Retrieved top height for Chappuis Ozone [km]
HT_AerosolBottom	Retrieved TH bottom for aerosol [km]
PmcL2gpValue	PMC Tangent Height [km]
PmcStatus	Flag for PMC presence

PscL2gpValue	PSC Tangent Height [km]
PscStatus	Flag for PSC presence
aerosolExtinctionConvergence	Retrieved aerosol extinction Convergence
aerosolExtinctionL2gpPrecision	Retrieved aerosol extinction uncertainty [km^{-1}]
aerosolExtinctionL2gpValue	Retrieved aerosol extinction profile [km^{-1}]
aerosolExtinctionQuality	Retrieved aerosol extinction Quality flag
aerosolExtinctionStatus	Retrieved aerosol extinction.Number of iterations
aerosolSizeAngstromCoeff	Retrieved aerosol size dist Angstrom coefficient
aerosolSizeRmean	Retrieved aerosol size distribution Rmean
aerosolSizeSigma	Retrieved aerosol size distribution Sigma
aerosolSizeMomentStatus	Size dist moment: (1)Angstrom, (2) microphysics
cloudHeightThick	Retrieved Thick Cloud top [km]
cloudHeightThin	Retrieved Thin Cloud top [km]
cloudHeightQuality	Retrieved Cloud top. Quality flag
sfcReflL2gpPrecision	Retrieved albedo standard deviation
sfcReflL2gpValue	Retrieved albedo
sfcReflQuality	Retrieved albedo Quality flag
stratO3L2gpPrecision	Integrated strat total column O3 uncertainty [Du]
stratO3L2gpValue	Integrated total column ozone / stratosphere [Du]
stratO3Quality	Integrated total column strat ozone Quality flag
Geolocation Fields	
Date	Calendar date
Latitude	Tangent point latitude (TH=20km)
LineOfSightAngle	Line-of-Sight direction wrt due North [°]
LocalSolarTime	Local solar time at tangent point
Longitude	Tangent point longitude (TH=20km)
OrbitGeodeticAngle	Orbit geodetic angle [°]
SingleScatterAngleAt20kmTH	Single scattering angle at 20km TH [°]
SolarAzimuthAngleAt10kmTH	Solar azimuth angle at 10 km TH [°]
SolarAzimuthAngleAt20kmTH	Solar azimuth angle at 20 km TH [°]
SolarAzimuthAngleAt40kmTH	Solar azimuth angle at 30 km TH [°]
SolarAzimuthAngleAt60kmTH	Solar azimuth angle at 40 km TH [°]
SolarZenithAngleAt10kmTH	Solar zenith angle at 10 km TH [°]
SolarZenithAngleAt20kmTH	Solar zenith angle at 20 km TH [°]
SolarZenithAngleAt40kmTH	Solar zenith angle at 30 km TH [°]
SolarZenithAngleAt60kmTH	Solar zenith angle at 40 km TH [°]
SpacecraftAltitude	Spacecraft altitude [km]
SpacecraftLatitude	Spacecraft latitude [°]
SpacecraftLongitude	Spacecraft longitude [°]
TerrainAltitude	Terrain altitude at point tangent point [km]
Time	UTC time

Additional	
A_prioriAerosolModelID	*A-priori* aerosol vertical extinction profile dataset
A_prioriAerosolModelImgRefIndex	Assumed aerosol refractive index. Imaginary

A_prioriAerosolModelLNSimga	*A-priori* aerosol size distribution variance
A_prioriAerosolModelMeanRadius	*A-priori* aerosol size distribution mean radius
A_prioriAerosolModelRealRefInd	Assumed aerosol refractive index. Real part
A_prioriAerosolSTDDEV	*A-priori* aerosol uncertainty $[km^{-1}]$
A_prioriAlbedo	*A-priori* albedo of the Nchannel channels used
A_prioriO3STDDEV	*A-priori* ozone uncertainty $[m^{-3}]$
A_priori_grid	Height grid on which a-priori is defined
A_priori_O3	*A-priori* ozone vertical profile $[m^{-3}]$
A_priori_aerosol	*A-priori* aerosol extinction vertical profile $[km^{-1}]$
Auroral	Flag for presence/absence of aurora
D1_O3_UV	Vertical profile of Residuals in O3 retrieval UV
D1_O3_Vis	Vertical profile of Residuals in O3 retrieval Vis
D1_aerosol	Vertical profile of Residuals in aerosol retrieval
Eclipse	Flag for presence of lunar/solar eclipse
InitialAtmosphereHscale	Vertical grid to define initial atmosphere [km]
InitialAtmosphereDensity	Initial atmosphere neutral density [1/m3]
InitialAtmosphereOzone	Initial atmosphere ozone density [1/m3]
InitialAtmosphereNO2	Initial atmosphere NO_2 density [1/m3]
InitialAtmosphereTemperature	Initial atmosphere temperature [K]
InitialAtmosphereAerosolWavelength	Wavelengths at which aerosol extint'n is defined
InitialAtmosphereAerosol	Initial atmosphere aerosol extinction [1/km]
InitialAtmospherePressure	Initial atmosphere pressure [Pa]
InversionVersionNumber	EDR version number
LunarDistToSlitBoresight	Distance of Moon wrt slit boresight [arcminutes]
NO2	NO_2 number density vertical profile
NO2model	NO_2 source: HALOE (SR/SS), model
Nchannel	Number of channels used in selection table
NormalizationHeightsUsed	Normalization TH of the Nchannel channels used
OrbitNumber	Orbit number
Pressure	Atmospheric pressure vertical profile [Pa]
ReconstructRadianceResiduals	Vertical profiles of radiance residuals [W/m2/nm/ster]
RetrievalAltGrid	Retrieval height grid [km]
RsasOffset	Retrieved Tangent Height registration offset [km]
RsasOffsetSTDDEV	Retrieved RSAS TH offset uncertainty [km]
SouthAtlanticAnomaly	Flag for South Atlantic Anomaly
Spec	Channel purpose each Nchannel channels
StarInSlit	Flag for presence of stars within FOV
THMinMax	Retrieval minimum and maximum TH [km]
TH_Retrieval_bottom	TH bottom for each Nchannel channls [km]
TH_Retrieval_top	TH top for each Nchannel channels [km]
Temperature	Atmospheric temperature vertical profile [K]
TropopauseHeight	Tropopause geometric height [km]
NCEPOzoneDensity	NCEP ozone density at event geolocation $[m^{-3}]$

ChannelWavelengths	Wavelengths of the Nchannel channels used
WaveReferenceOzoneLeft	Left Ref channel used by each Nchannel channl
WaveReferenceOzoneRight	Right Ref channel used by each Nchannel channl
AlbedoTable	Albedo used by each Nchannel channels
WavelengthRegistrationOffset	Retrieved wavelength registration offset [nm]

3.10.2 Diagnosis graphic files

Figure 3-10 shows the content of the graphical diagnosis file. This picture, which corresponds to a given slit of a single limb scatter event, is composed of 6 panels:
- the top left panel shows the retrieved ozone profile for both the Hartley/Huggins and Chappuis bands at each iteration
- the top center panel shows the retrieved aerosol profile at each iteration
- the bottom left panel shows the SDR radiance profiles
- the bottom center panel shows the convergence of the optimal estimation measurement vectors for both ozone bands and the aerosol
- the top right panel displays information on the limb scatter event
- the bottom right panel shows the geo-location of the tangent point
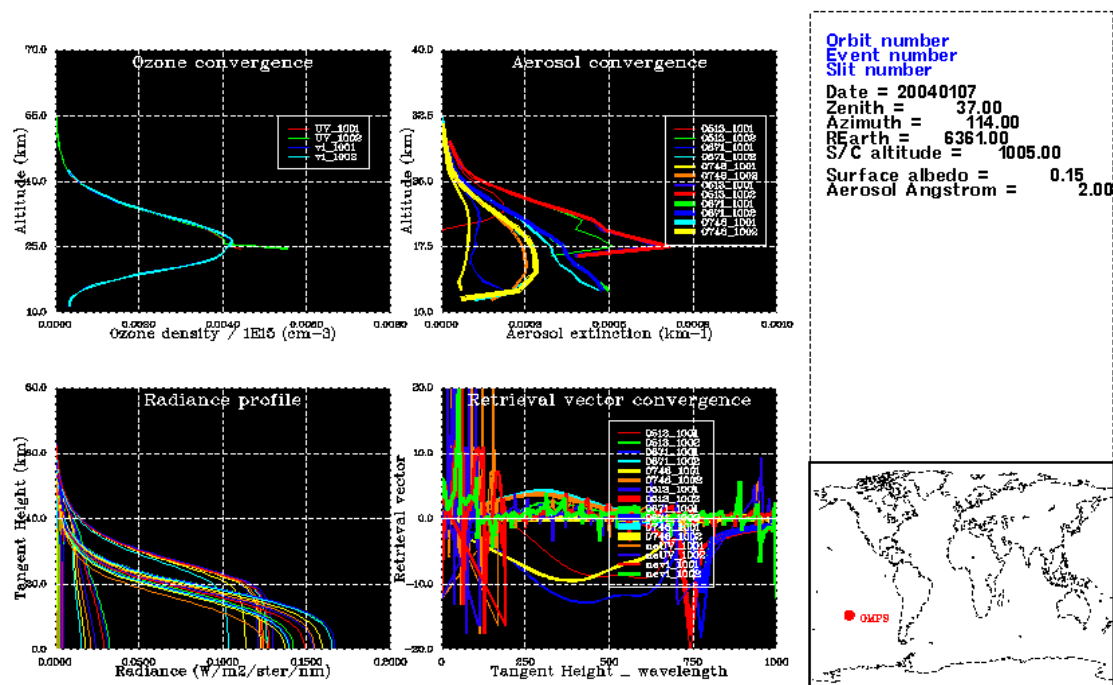
Figure 3-10. *OMPS/LP graphical diagnosis. Such plots will be used to diagnose the retrieval process for each LS event.*
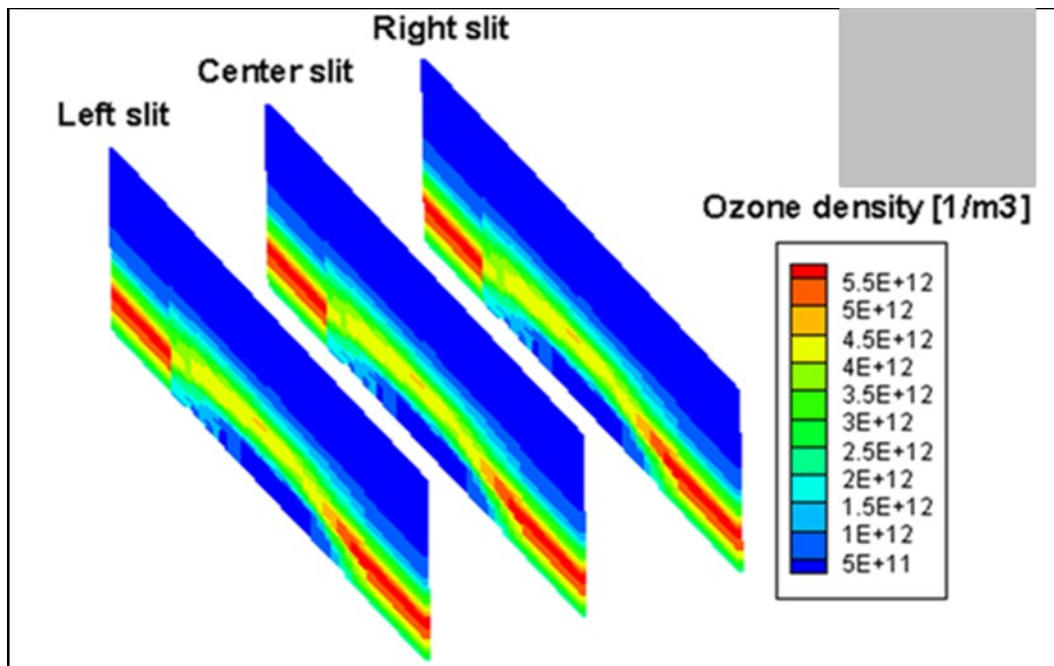
Figure 3-11. Curtain file of ozone density profiles for one orbit. Each retrieved vertical profile (every 19 seconds) is plotted contiguously to assess retrieval quality.

4.0 ALGORITHM TESTING AND PERFORMANCE

4.1   Testing methodology

The code testing has two purposes, namely (1) to analyze the functionality of modules and the links between modules, and (2) to assess the performance of the algorithms. The functionality test deals with issues such as code integrity and inter-module interfaces, whereas the performance test is concerned with quantifying the accuracy and precision of the algorithms. While functionality testing requires relatively simple testing datasets, the performance testing necessitates more elaborate tools such as a detailed instrument model as well as a large ensemble of synthetic and proxy limb scatter events encompassing a wide set of viewing conditions, atmospheric composition and viewing scene characteristics.

4.2   EDR algorithm performance

The EDR retrieval algorithm is being tested alternatively with either synthetic data (generated with a forward model) or proxy data (generated from actual measurements made by existing LS instruments, such as SAGE III LS, OSIRIS, and SCIAMACHY). The first type of testing allows one a full control on the problem parameters, whereas the second one contains "real world" effects such as data imperfections (instrument effects), clouds, underlying scene inhomogeneities, along-track inhomogeneities, etc.

4.2.1   Algorithm testing with synthetic data

4.2.1.1   Concept and sample result

Synthetic limb radiance data are generated using the forward model described in Section 3.3. The resolution for each of the three computational spectral grids was initially set up to be as fine as possible: the finer grid resolution matched the solar spectrum data sampling, whereas the single- and multiple-scattering grids resolution equaled the ozone absorption cross-section data sampling. Further experimentation revealed that additional loosening of the grid resolution produced substantial time savings (from many hours down to 3 minutes CPU time to calculate a complete image), with radiance accuracy better than 0.2% at all wavelengths. This relaxed grid which is used to generate synthetic data is illustrated in Figure 4-1.
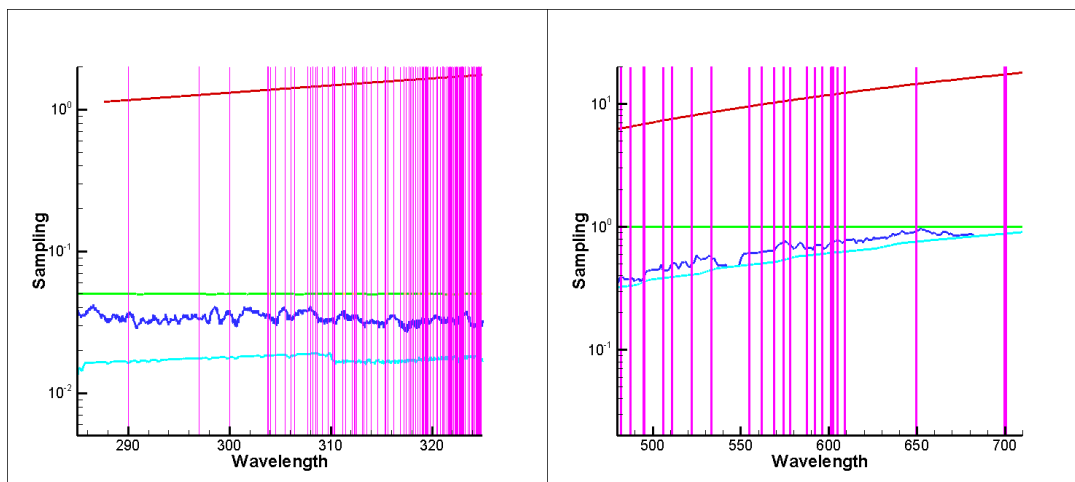
Figure 4-1. *Computational grid sampling (in nm) used to generate synthetic data, compared to ozone cross-section sampling and OMPS instrument characteristics, for UV wavelengths (left panel) and visible wavelengths (right panel). Color scheme is identical to Figure 3-1.*

An example of the performance of the OMPS/LP algorithm is shown in Figure 4-2, which compares the retrieved profile to the input profile used in the forward simulation. The test case corresponds to a low latitude observation, with background aerosol, solar zenith angle = 55° and azimuth angle = 51°. Algorithm retrieval accuracy is compared to the retrieval 1 σ uncertainty (shown as a grey shaded area). The retrieval errors are mostly less than 1% at all altitudes. TH misregistration (and subsequent correction) are included in the results. Somewhat larger errors (<2%) can be seen when the algorithm must retrieve both aerosol and ozone.
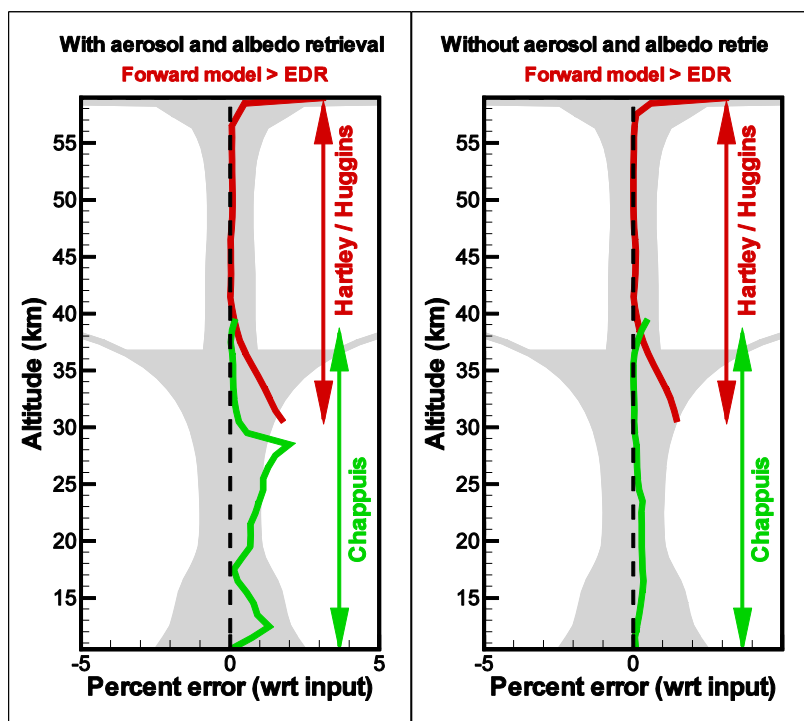
Figure 4-2. *Testing ozone retrieval algorithm. Red and green lines refer to Hartley-Huggins and Chappuis band retrievals, respectively. Grey shaded zones indicate the retrieval 1-σ uncertainty.*

46

4.2.1.2 Testing with large synthetic dataset

For more comprehensive testing of the retrieval algorithm, a relatively large synthetic dataset is used. This step allows one to test the EDR algorithm over a wide range of geo-locations, zenith angles and ozone vertical profiles, and therefore statistically evaluate the performance of the EDR modules and quantify retrieval uncertainties.

The synthetic dataset is composed of 450 LS events, each one corresponding to a co-location of a SAGE II occultation measurement with a SCIAMACHY limb scattering measurement over a one-year period. SAGE II was selected as reference since it is widely recognized by the community *[Wang et al., 2002, Borchi et al., 2004, Thomason 2006]* as the de-facto standard for global ozone measurements in terms of accuracy and precision. *[Borchi et. al., 2004]* have conducted a series of intensive inter-comparisons campaigns which showed that the SAGE II ozone measurements have a precision of 2% or better in the lower stratosphere. Additionally, *[Cunnold et al., 2004]* made extensive comparisons between SAGE II and ozone sondes and showed that SAGE II data is statistically indistinguishable from ozone-sondes data from the tropopause up to 30 km. SCIAMACHY was selected because it is an LS sensor with an obit similar to the one contemplated for OMPS. To create the OMPS/LP synthetic dataset, the forward model is run using (a) input ozone profile from the SAGE II retrieved product, and (b) solar view angles from the SCIAMACHY measurements. For all events, the simulation assumes a uniform surface albedo $\alpha = 0.15$, and a constant aerosol extinction profile typical of present background conditions. The atmospheric temperature and pressure profiles are generated from NCEP reanalysis interpolated at the event location. The synthetic events encompass a wide range of geo-locations, seasons and solar viewing angles, as illustrated in Figure 4-3 and 4-4. The size of the synthetic dataset was chosen to ensure meaningful statistics of the testing procedure.
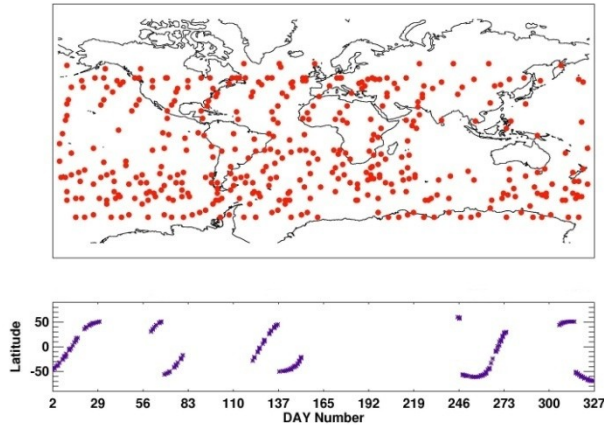
Figure 4-3. *Geo-location for 450 LS events dataset*
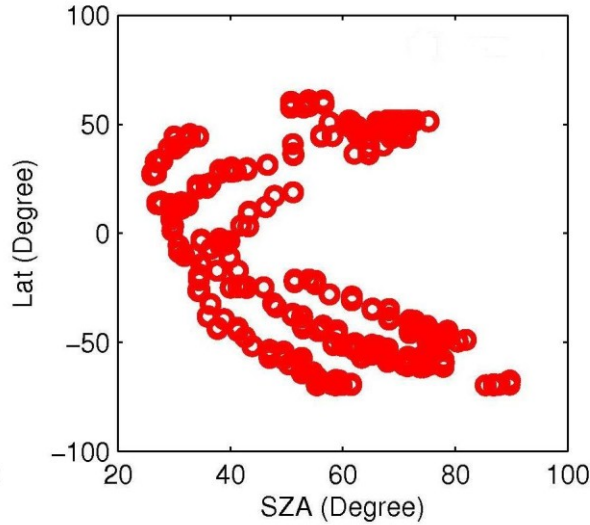
Figure 4-4. *Distribution of the solar zenith angle vs. latitude for the 450 LS event dataset.*

For the EDR retrieval, the *a-priori* ozone data vector is evaluated for given latitude and calendar month from the SAGE II climatology, while the *a-priori* aerosol vector used is three times the value of the input aerosol profile. For both the forward simulation and the EDR retrieval, the *a-priori* aerosol size distribution is assumed to be single mode log normal distribution, with 0.06 μm effective radius and variance σ of 1.73, composed of spherical liquid sulfate particles, with an index of refraction *m=1.448+0i*. The same temperature, pressure, and NO_2 profiles are also used in the simulation and inversion. Instrument noise is not included in the simulated radiances, and the instrument vertical slit function is not accounted for in neither the forward simulation nor the EDR inversion. In the EDR, the retrieved aerosol microphysical properties are used to interpolate aerosol extinctions.

Figure 4-5 to 4-8 summarize the outcome of the statistical analysis performed on the EDR retrieved products. Figure 4-5 is a histogram of the retrieved albedo, which shows a mean bias of about 20% and a standard deviation of 15%. Figure 4-6 shows the performance of the RSAS retrieval in the form of a histogram of the retrieved RSAS offset. As explained in Section 3.0, the RSAS module is run twice, before and after the aerosol retrieval. Figure 4-6 corresponds to the final RSAS offsets, and shows a mean bias of about 50 m and a standard deviation of less than 50 m. The retrieved altitude offsets are used here for diagnostics only and no correction is applied downstream to the retrieval profiles. The performance of the aerosol retrieval is shown on Figure 4-7. Mean biases are on the order of 5%, while standard deviation is about 10%. Finally, Figure 4-8 shows the performance of the ozone retrieval. Both the Hartley-Huggins and Chappuis retrievals have an accuracy of better than 1% in the 20-58 km range. The ensemble standard deviation is also about 1% over the same altitude range.
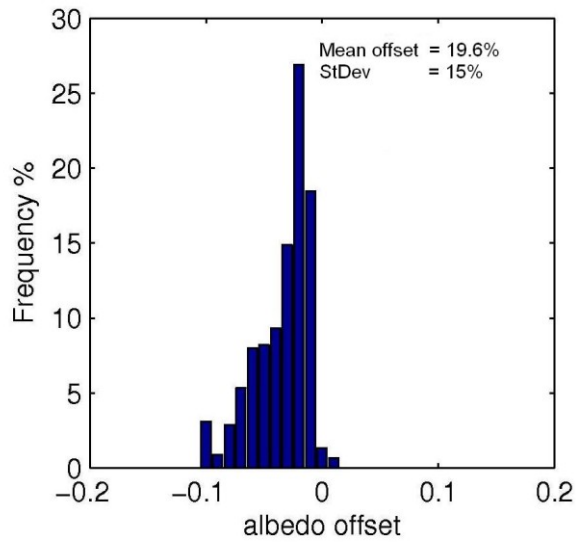
Figure 4-5. *Effective scene albedo histogram obtained with the 450 LS events ensemble.*
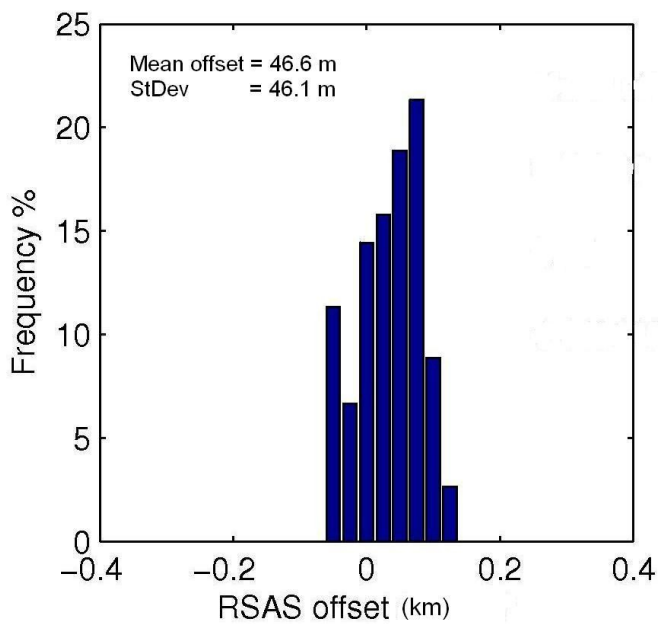
Figure 4-6. *Tangent height registration RSAS offset histogram obtained with the 450 LS events ensemble.*
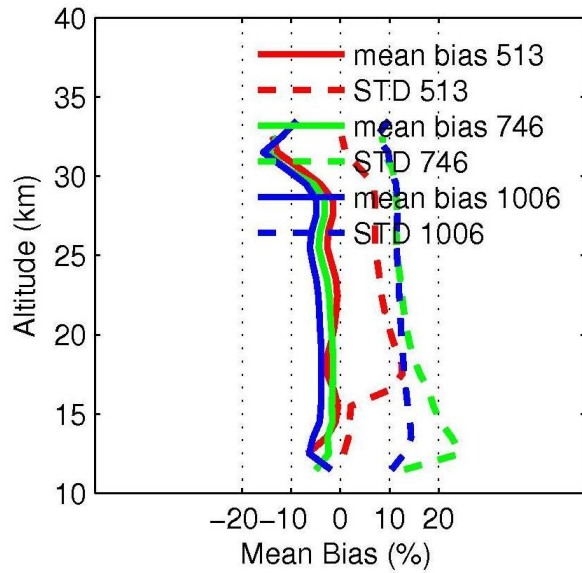
Figure 4-7. *Aerosol extinction profile retrieval. Mean biases are represented by solid lines, ensemble standard deviation by dashed lines. Blue corresponds to 1006 nm, green to 746 nm, and red to 513 nm.*
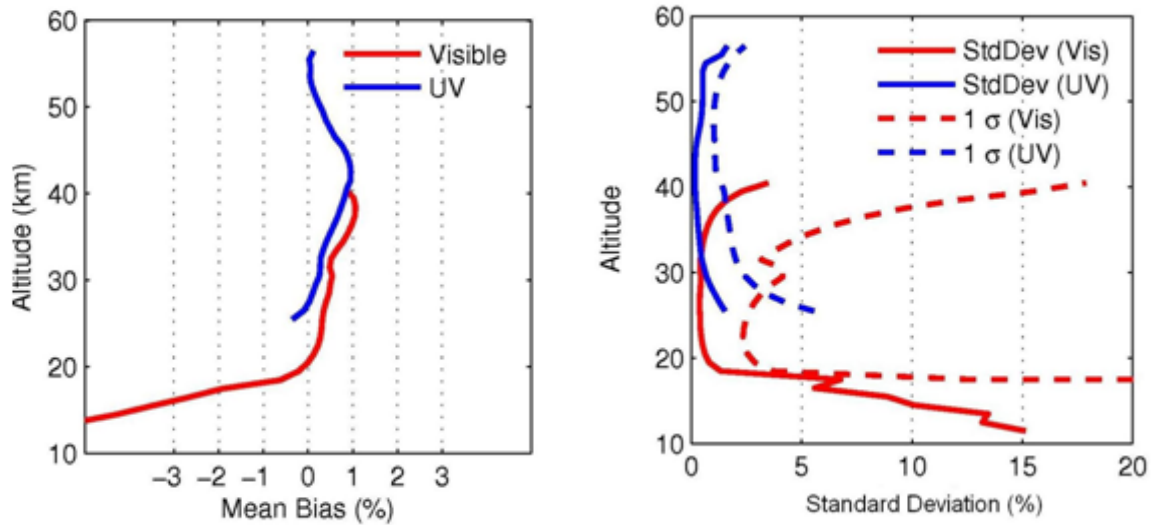
Figure 4-8. *Summary plot of the percent difference for all retrieved ozone profiles for the 450 simulated radiances, red is for visible, and blue is for UV retrievals. The left panel shows the mean bias, while the right panel shows the ensemble standard deviation, with dash lines representing the retrieval 1-σ uncertainty*

4.2.2 Algorithm testing with proxy data

While synthetic datasets allows the testing of the EDR under controlled and well known conditions, the testing with proxy data generated from actual LS measurements made by other sensors, such as OSIRIS and SCIAMACHY, allows one to verify the performance of the algorithm under "real-world" conditions. The effect of clouds, along-track and across-track inhomogeneities, straylight residuals, etc. can thus be included. Using a set of OSIRIS and SCIAMACHY measurements coincident with SAGE II solar occultations offers the additional advantage of a direct comparison of the OMPS/LP algorithm products with SAGE II retrievals, under a wide range of atmospheric conditions, geo-locations, zenith solar angles and seasons. Such comparison is obviously difficult since it does involve instrument artifacts and effects (which are different with each sensor) and atmospheric variability. Nonetheless, the results obtained herein can be considered as upper bounds for the accuracy and precision of the OMPS/LP retrieval algorithm.

The following assumptions were made for all of the proxy data analysis presented in Sections 4.2.2.1 and 4.2.2.2:

- The *a-priori* ozone profile is evaluated for given latitude and calendar month from the SAGE II climatology described in Section 3.5.6.
- The aerosol extinction profiles $\beta(h,\lambda)$ at height h and wavelength λ are a consistent set of profiles corresponding to the present period of low stratospheric background aerosol, as described in Section 3.7.
- The aerosol size distribution in *both* the forward simulation and t*he* EDR inversion is assumed to be single mode log normal distribution, with 0.06 μm effective radius and variance σ of 1.73, composed of spherical liquid sulfate particles, with an index of refraction *m=1.448+0i*.
- In both the forward simulation and the EDR inversion, the atmospheric temperature and pressure profiles are generated f*ρ*om the NCEP (ECWMF for OSIRIS) d*α*taset, and the NO_2 information is taken from climatology constructed using the PRATMO p*hotochemic*al box model.
- Signal-to-Noise-Ratios provided by the relevant research team (OSIRIS or SCIAMACHY, respectively) were used.

4.2.2.1 OSIRIS-based proxy data

The OSIRIS spectrograph has been making Limb Scatter measurements since February 2001 *[Degenstein et al., 2009]*. It measures scattered sunlight over the wavelength range 280–810 nm (with a segment gap between 476 and 530 nm) with a 1 nm resolution. Its instantaneous field of view is about 1 km and its vertical sampling varies from 1.5 to 3.75 km. OSIRIS is on a sun-synchronous circular orbit, with a 1800 local solar time ascending node, which confines its observations to a range of high solar zenith angles. See *[Llewellyn et al., 2004]* for more detailed information on OSIRIS.

OMPS/LP spectral resolution is about the same as OSIRIS in the UV spectral range, but lower in the visible. To generate OMPS proxy data from OSIRIS radiance measurements, one must degrade OSIRIS data. This is accomplished by convolving OSIRIS measurements with the OMPS/LP slit function. Furthermore, OMPS/LP vertical sampling is smaller than OSIRIS and to

produce OMPS proxy at 1 km interval, one must create additional data points to satisfy the OMPS/LP algorithm requirements. This is accomplished by linear interpolation of the logarithm of the radiance. No attempt was made to degrade OSIRIS vertical resolution to match OMPS/LP values. Instead, in both the forward simulation and the EDR inversion, the vertical resolution is not considered; i.e., FOV is assumed to be 0 for the OSIRIS proxy data study.

A subset of OSIRIS events is selected to test the OMPS/LP retrieval algorithm performance. This subset corresponds to OSIRIS observations which occurred in the close vicinity of SAGE II occultation events, so that OMPS/LP retrievals can be compared directly with SAGE II ozone and aerosol products. Geo-location and solar zenith angle information for the subset of OSIRIS events is displayed in Figure 4-9.

Figure 4-9. *Geo-location for OSIRIS events used for OMPS proxy.*
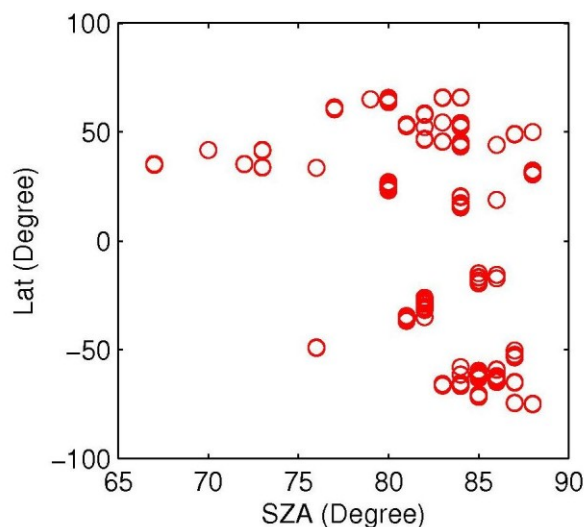
Figure 4-10. *Distribution of the solar zenith angle vs. latitude for the OSIRIS dataset.*

Figure 4-9 and 4-10 show a sample comparison of OMPS/LP and SAGE II products. The OMPS/LP ozone retrieval closely reproduces the occultation measurements, including the sub-layer which appears below the ozone maximum. The aerosol retrieval was performed for a series of wavelengths at 710, 750, 790 nm and the retrieved aerosol microphysics were used to infer aerosol extinction between 500 and 700 nm. As shown in Figure 4-11, the retrieved aerosol extinction compare well with SAGE II measurements in the altitude range within which limb

signal is sufficiently sensitive to aerosol, which typically extends from 15 to 30 km. Figure 4-12 displays the statistics of SAGE II vs. OMPS/LP comparisons for a series of about 200 OSIRIS events randomly spread over the Earth surface, with solar zenith angles less than 88°. Aerosol distribution and size parameter were simultaneously retrieved. Relative accuracy within 5 % can be observed in the altitude range 20 to 50 km, with relative precision of better than 10% for both the Chappuis and Hartley-Huggins bands.

Figure 4-11. *Testing ozone and aerosol algorithms with OSIRIS proxy data. Comparison with coincident SAGE II occultation measurements. Individual retrieved profiles are shown in color, whereas SAGE II products are shown in black. [Bourassa,2008].*

Figure 4-12. *Testing ozone algorithm with OSIRIS proxy data. Comparison with coincident SAGE II occultation measurements. Statistics over 200 events. [Bourassa,2008].*

4.2.2.2 SCIAMACHY-based proxy data

The hyper-spectral spectrometer SCIAMACHY has been making Limb Scatter measurements since March 2002 *[Eichmann et al., 2004]*. It measures atmospheric radiance spectra from 240 to 2380 nm at a resolution ranging from 0.24 to 1.5 nm. Its instantaneous field of view is about 110x2.6 km (horizontal x vertical) and its vertical sampling is 3.3 km. SCIAMACHY is on a sun-synchronous circular orbit at 799.8 km altitude with an inclination angle of 98.55° and a 10:00 am local solar time descending node *[Bovensmann et al.,1999]*.

SCIAMACHY spectral resolution is finer than OMPS/LP resolution in both the UV and visible spectral ranges. To generate OMPS proxy data from SCIAMACHY radiance measurements, one must degrade SCIAMACHY data. This is accomplished by convolving SCIAMACHY measurements with the OMPS/LP slit function. Furthermore, both sensors have about the same vertical resolution, but OMPS/LP vertical sampling is smaller than SCIAMACHY and to produce OMPS proxy at 1 km interval, one must create additional data points to satisfy the OMPS/LP algorithm requirements. This is accomplished by linear interpolation of the logarithm of the radiance. To account for the relatively coarse vertical resolution, simulated radiances are convolved with a vertical Gaussian slit function with a Full Width Half Maximum (FWHM) of 2.7 km.

A subset of SCIAMACHY LS events is selected to test the OMPS/LP retrieval algorithm performance. This subset corresponds to SCIAMACHY observations which occurred in the close vicinity of SAGE II occultation events, so that OMPS/LP retrievals can be compared directly with SAGE II ozone and aerosol products. Geo-location and solar zenith angle information for the subset of SCIAMACHY events is displayed in Figure 4-13 and 4-14.
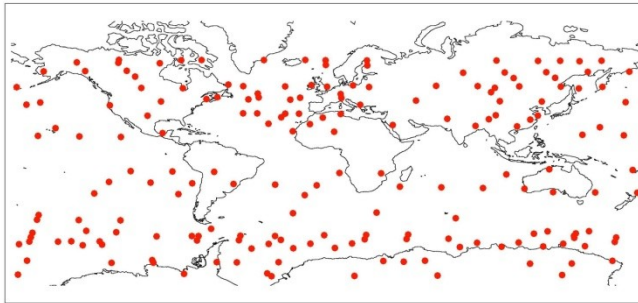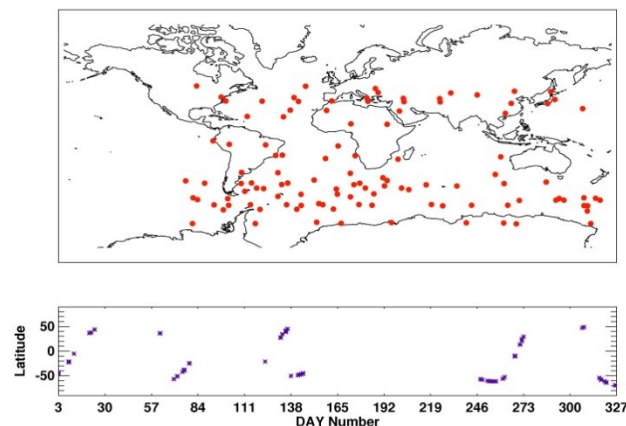

Figure 4-13. *Geo-location for SCIAMACHY dataset used for OMPS proxy.*
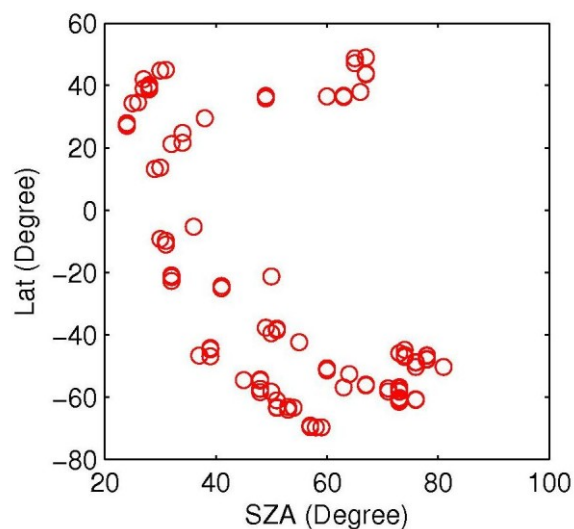
Figure 4-14. *Distribution of the solar zenith angle vs. latitude for the SCIAMACHY dataset.*
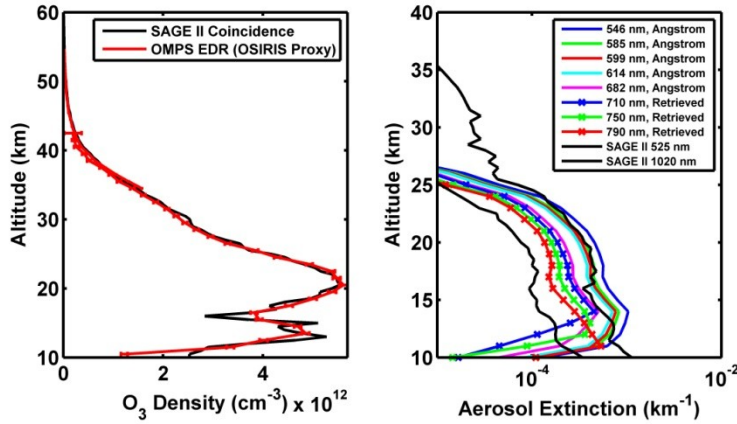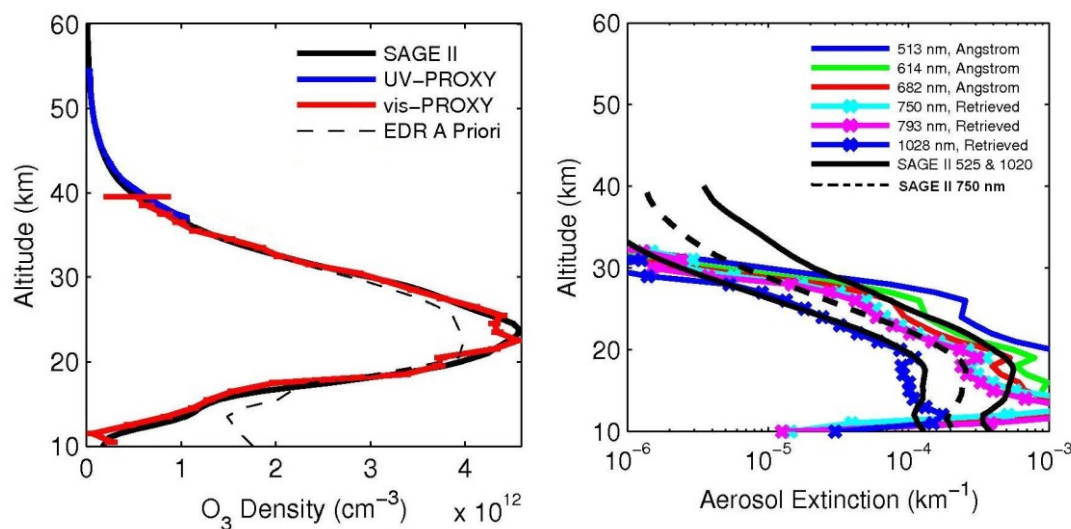

Figure 4-15. *Testing ozone and aerosol algorithms with SCIAMACHY proxy data. Comparison with coincident SAGE II occultation measurements. Individual retrieved profiles are shown in color, whereas SAGE II products are shown in black.*

Figure 4-15 shows a sample comparison of OMPS/LP and SAGE II products. The OMPS/LP ozone retrieval can be observed to closely match SAGE II measurements. The aerosol retrieval was performed for a series of wavelengths between 750 and 1028 nm. They compare well with SAGE II measurements in the altitude range within which limb signal is sufficiently sensitive to aerosol, which typically extends from 16 to 30 km. Figure 4-16 displays the statistics of SAGE II vs. OMPS/LP comparisons for a series of 120 SCIAMACHY events randomly spread over the Earth surface, with solar zenith angles less than 88°. Aerosol distribution and size parameter were simultaneously retrieved. Relative accuracy of better than 5% can be observed in the

altitude range 22 to 38 km, and within 5-10% for altitude range 40-52 km. The relative precision is better than 10% in the Chappuis band and 15% in the Hartley-Huggins bands.
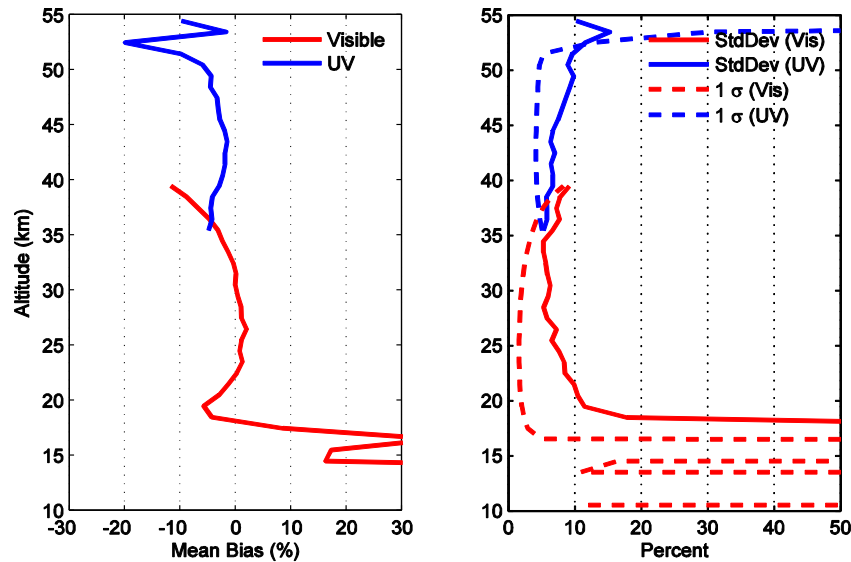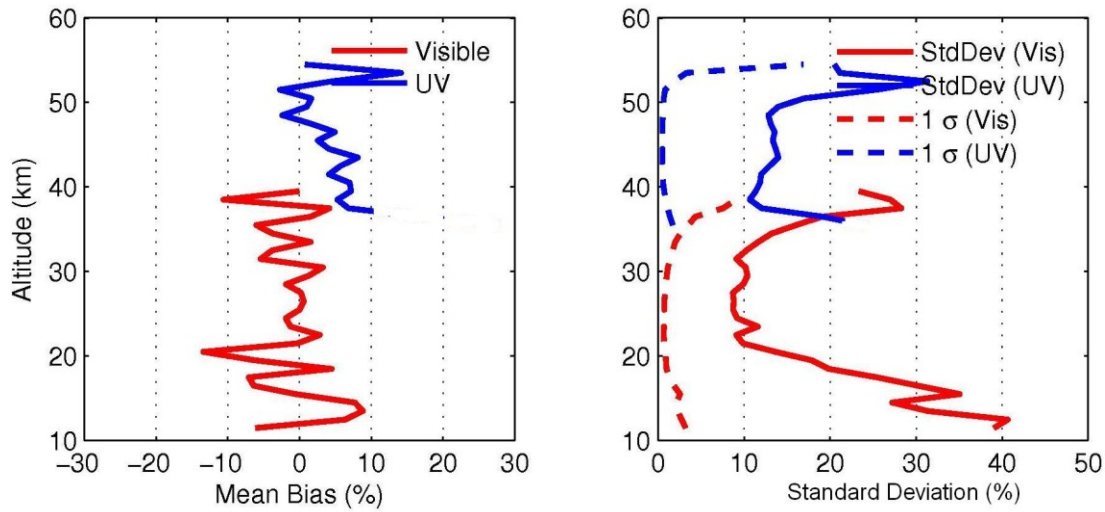

Figure 4-16. *Testing ozone algorithm with SCIAMACHY proxy data. Comparison with coincident SAGE II occultation measurements. Statistics over 120 events*

4.3 End-to-End testing

4.3.1 Testing methodology (End-to-end testing chain)

Figure 4-17 shows the main modules used in the end-to-end testing of the SDR+EDR combination of codes. Starting from an assumed atmosphere composition (ozone density profile, aerosol extinction profile, NO_2 density profile and temperature/pressure profile) and Earth reflectance characteristics (albedo), the forward model described in Section 4.2.1.1 is used to compute the limb radiance profile over a wide spectral range (280 to 1020 nm) for tangent heights ranging from 0 to 80 km. The output of the forward model is a two-dimensional array of limb radiances convolved with the spectral and spatial slit functions of the instrument. The instrument model described in Appendix C is then used to convert radiances into electrons for each integration time, evaluate measurement noise (shot, read, quantization), map modeled radiances onto the CCD array grid and add contribution from straylight. The output of the instrument model is expressed in terms of counts for each CCD pixel which has been marked to be downlinked. The simulated CCD map is then used to test the SDR main modules (straylight mitigation, Tangent Height registration, two-dimensional gridding and consolidation) and the EDR. The outcome of the end-to-end testing is a statistical comparison of the EDR outputs (ozone, aerosol, TH registration, albedo) with the corresponding characteristics of the input atmosphere. The end-to-end testing is used to check the data flow through the SDR+EDR as well as quantify the performance of the algorithm in terms of accuracy and precision. The effect of parameters such as CCD pixel PSFs, spectroscopic absorption coefficients, spectral/spatial registration biases, instrument noise, straylight residuals, etc,… can also be studied with the end-to-end testing chain.
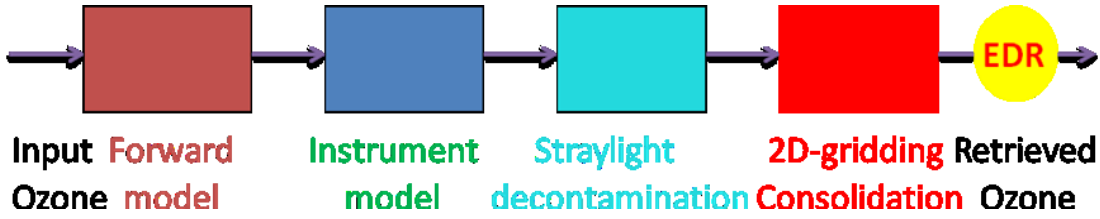
Figure 4-17. *End-to-end testing chain. Synthetic CCD maps are simulated using the RT forward model (to generate limb radiances) and the Instrument Model. The CCD map pixel data is then preprocessed (straylight mitigation and gain consolidation) before EDR retrieval.*

4.3.2 End-to-end testing results

The end-to-end test chain has been exercised using the same proxy SCIAMACHY-SAGE II based dataset described in Section 4.2.2.2. The dataset consists of 450 LS events, each one corresponding to a co-location of a SAGE II occultation measurement with a SCIAMACHY LS measurement. Figure 4-18 and 4-19 show the statistics of the comparison between the chain inputs and outputs for each of the three slits. The performance of the RSAS module is illustrated in Figure 4-18, which shows a histogram of the RSAS offset for each slit. The mean bias is < 40 m and the standard deviation is less than 100 m. Figure 4-19 presents the results of the ozone retrieval in terms of mean bias and standard deviation for each slit. The Hartley-Huggins retrieval has an accuracy of better than 3%. The standard deviation is about 2-3% from 30-60 km. The Chappuis band retrieval shows an accuracy of better than 4% from 20-40 km with a standard deviation of 2-5%. A fairly large number of events in the dataset correspond to high latitudes and exhibit low ozone density at lower altitudes. As a consequence, relative errors below 20 km are significant. In all cases the ensemble standard deviation and the retrieval 1-σ uncertainty are in close correlation, which indicates that the error dispersion is mostly due to "measurement" random noise and ozone sensitivity decrease at low and high altitudes for each absorption band. The performance of the aerosol retrieval is illustrated in Figure 4-20, which compares the mean aerosol profile to the assumed input profile, and shows the mean bias and the standard deviation for each slit. Aerosol can be retrieved with accuracy within 10%, which should be sufficient to adequately ascertain and correct for the aerosol effect on ozone retrieval.
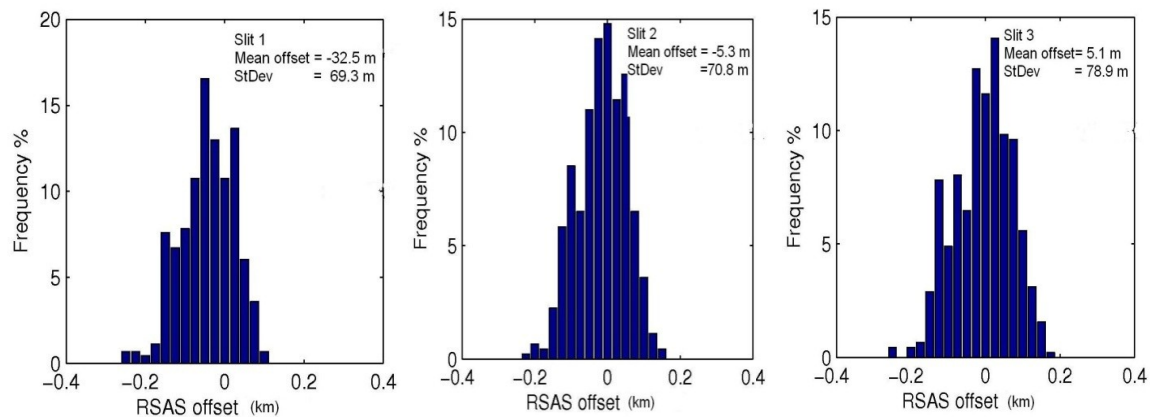
Figure 4-18. *Tangent height registration offset histograms for each slit.*

57
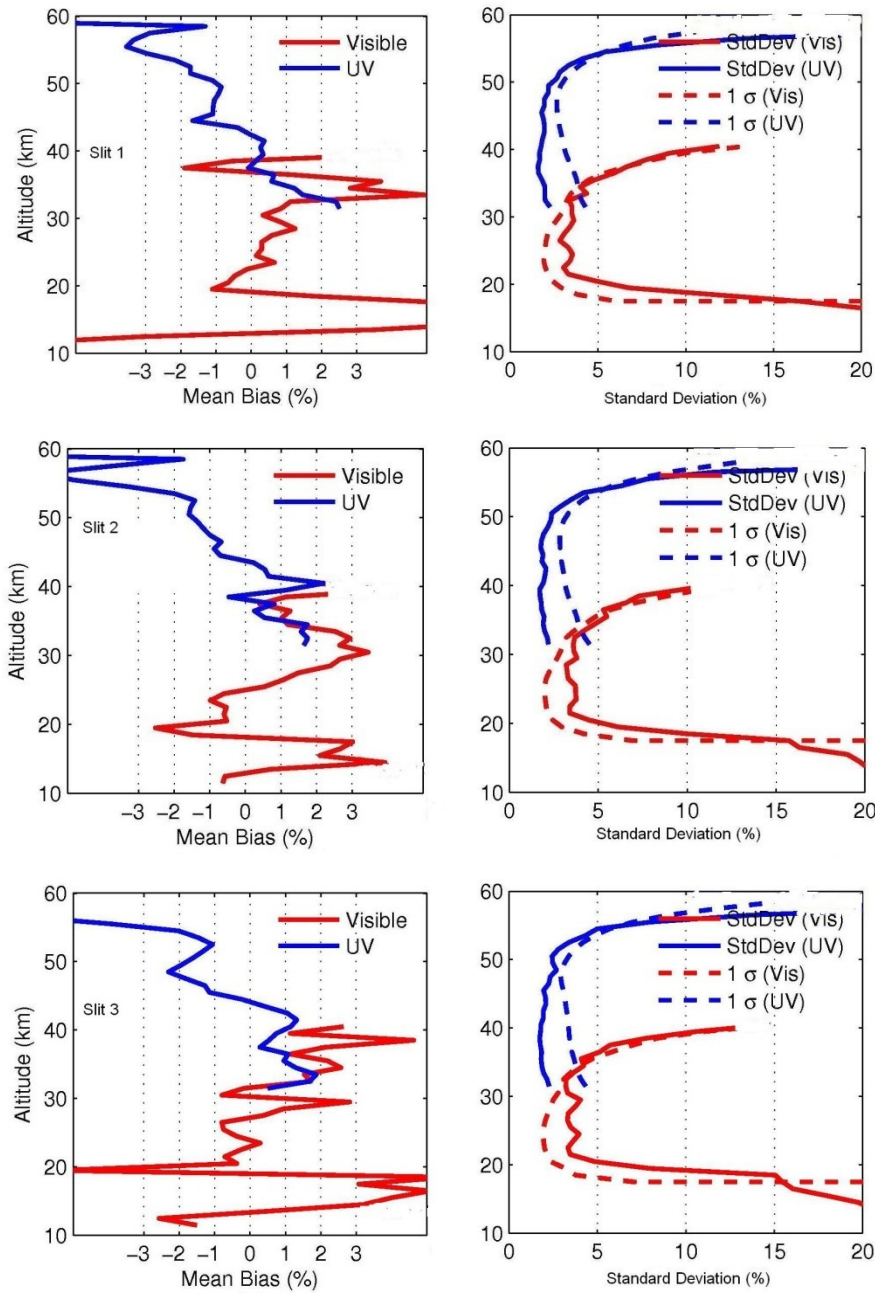
Figure 4-19. *Ozone retrieval for each slit. Left panels represent the mean biases and right panels represent the standard deviation and retrieval 1σ uncertainty. Red refers to Chappuis band retrieval and blue to the Hartley-Huggins retrieval UV retrievals.*
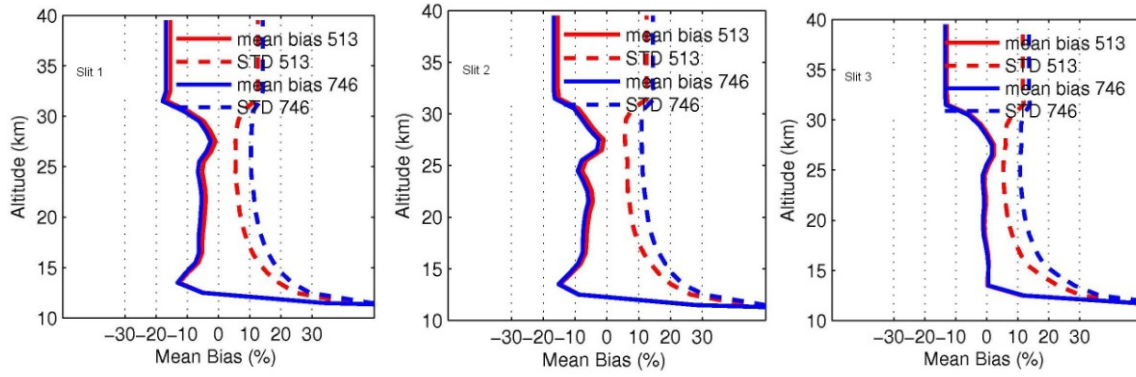
Figure 4-20. *Aerosol extinction retrieval for each slit. Solid lines correspond to mean biases and dashed lines to ensemble standard deviation. Blue refers to 746 nm and red to 513 nm.*

5.0 ACCURACY AND PRECISION

The accuracy and precision of the OMPS/LP sensor are being analyzed and quantified using the A-to-Z chain described in Section 4.3. The present section describes the most pertinent results of this analysis and also refers to an earlier study of the OMPS/LP instrument conducted by *[Larsen et al., 2005]* whenever required. Since the sensor products are vertical profiles, this analysis is concerned with uncertainties in both the gas density (or alternatively the aerosol extinction) and the vertical height registration.

5.1   Accuracy of ozone profile retrievals

The accuracy of the retrieved ozone profiles is a measure of the biases and systematic errors introduced in the data preprocessing and retrieval process. Table 5-1 lists the main sources of error which contribute to the ozone measurement accuracy budget. In orbit, the relative accuracy will be assessed by comparing the OMPS/LP retrieved ozone profiles with correlative/collocated measurements made by ozone-sondes, lidars or other space-based sensors (OSIRIS, SCIAMACHY, Microwave Limb Sounder (MLS), SAGE III) as was done by *[Rault and Taha, 2007]*. Prior to launch, accuracy assessments are made by passing simulated OMPS/LP radiances through the algorithms, as described in Section 4.2.1.

Table 5-1. *Sources of ozone errors (accuracy)*

Origin of error	Source of error
Sensor / Calibration	Absolute radiometric coefficients Pixel-to-pixel radiometric calibration Spectral registration
Sensor / Instrument effects	Residual polarization sensitivity Residual straylight PSF and ghosts Boresight and sensor alignment uncertainty Thermal distortion uncertainty
SDR Algorithm	Two-Dimensional gridding Gain consolidation Pointing retrieval (see Section. 5.3)
Atmospheric composition	Aerosol retrieval errors NO_2 density Temperature profile
Forward model	Ozone cross sections NO_2 cross sections Rayleigh cross sections
Scene	Inhomogeneous ground/cloud albedo

The absolute radiometric calibration errors induce errors in the retrieval of surface reflectivity α. Since the ozone retrieval algorithm is basically self-calibrating (through high altitude radiance normalization), these errors only minimally contribute to ozone uncertainty. As shown by *[Rault and Taha, 2007]* and *[Loughman et al. 2005]*, a 0.1 albedo error results in ozone uncertainty of less than 1%.

Polarization of backscattered radiation in the UV is significant, which could induce large solar-angle dependent ozone retrieval errors, which in turn will cause cross-track and latitudinal dependent ozone biases. However, the OMPS/LP sensor uses a depolarizer at its entrance aperture, with a specification-limited residual linear polarization of 2%. This residual polarization should minimally affect the accuracy of ozone retrieval since, as shown by *[Larsen et al., 2005]*, the systematic ozone errors for a residual depolarization of 10% is less than 0.1% over the whole range of altitudes.

The effect of residual straylight, 2D gridding, consolidation and aerosol retrieval errors on ozone retrieval have been estimated by using the A-to-Z chain testing setup described in Section 4.3. These results were obtained with a series of 450 synthetic LS events corresponding to the SCIAMACHY/SAGE II coincidences. The forward model used in both the synthetic radiance simulation and the EDR includes the finite spectral bandpass and the finite vertical slit function. The effects of two-dimensional gridding and consolidation are taken into account as well as sensor noise and spectral/spatial smile. All the steps in the EDR are exercised, including albedo and aerosol retrievals and TH registration. As can be observed in Figure 4-19 (left panels), accuracy on the order of 4% can be obtained from altitudes 20 to 55 km, for each of the three slits

The effect of uncertainties on PSF and ghosts on ozone retrieval can also be obtained using the A-to-Z chain setup. The shape of the PSF and the ghosts (height and location) can be slightly altered in the instrument model and the straylight module and the resulting effect on ozone retrieval can be evaluated.

The effect of spectral mis-registration can likewise be ascertained with the A-to-Z chain testing setup.

All the other effects have been quantified by *[Larsen et al., 2005]* and the results are summarized in Table 5-2 and Table 5-3.

Table 5-2. *Effect of algorithm- and scene-related effects on ozone retrieval accuracy [Larsen et al., 2005]*

Effect	Tropopause-15 **km**	15 km-28 km	28 km – 60 km
Rayleigh cross-sections	0.3 %	0.3 %	0.3 %
Ozone cross-sections	1.25 %	1.25 %	1.0 %
Ozone cross-section temperature coefficient	0.15 %	0.15 %	0.88%
Aerosol	4.0 %	4.0 %	0.3 %

Neutral density	1.0 %	1.0 %	2.0 %
Non-homogeneous scene	0.1 %	0.1 %	0.1 %

Notes on Table 5-2:
(1) The Rayleigh scattering coefficients have an accuracy of 0.3% *[Bodhaine et al., 1999]*.
(2) The ozone absorption coefficients in the Chappuis band have an accuracy of 1.25% *[Anderson and Mauersberger, 1992]* and 1.0% in the UV *[Bass-Paur comparisons, 2000]*
(3) The ozone temperature dependent coefficients are assumed to have an error of 0.25%/K in the UV and 0.1%/K in the Chappuis band. The temperature uncertainty is assumed to be 1.5 K for altitude below 28 km and 3.5 K for altitude above 28 km.
(4) For the aerosol effect, a series of LS events are used, with representative TOMS standard atmospheres (H325, L275 and M325). The aerosol related effects on ozone errors depend on background stratospheric aerosol number concentration, size distribution and refractive index. The worst case scenario is identified and used for the estimate of the error for each altitude range.
(5) The systematic error on number density is assumed to be 1% for retrievals lower than 28 km and 2% for retrievals above 28 km.
(6) The effect of non-homogeneous scene along the line-of-sight (LOS) is evaluated by varying the reflectances under and along the line-of-sight (LOS) *[Flittner, 2003]*

Table 5-3. *Effect of sensor-related parameters on ozone retrieval accuracy [Larsen et al., 2005]*

Effect	Tropopause-15 km	15 km-28 km	28 km – 60 km
Initial wavelength-independent albedo calibration	1.5%	1.5%	0.2%
Long-term wavelength-independent albedo calibration	0.5%	0.5%	0.05%
Initial wavelength-dependent albedo calibration	2.0%	2.0%	0.1%
Long-term wavelength-dependent albedo calibration	1.0%	1.0%	0.05%
Pixel-to-pixel radiometric calibration uncertainty	1.4%	1.4%	1.4 %
Wavelength calibration accuracy	1.44%	1.44%	1.42%
On-orbit wavelength calibration	0.44%	0.22%	0.53%

Notes on Table 5-3:

(1) Use of tangent height normalization and wavelength groups makes the OMPS/LP algorithm largely self-calibrating. The values given in Table 5-3 refer to the small residual sensitivity to the albedo calibration, both initially (in the immediate post-launch period) and long-term (after the initial on-orbit calibration period).

(2) The uncertainty of the relative calibration (including flat-fielding, linearity and offsets) also contributes to the ozone profile accuracy.

(3) Wavelength calibration accuracy is also broken down into two components: The initial sensitivity to wavelength calibration, and an additional term due to imperfect characterization of the change in the wavelength registration during a typical orbit (due to thermal stresses, etc.).

5.2 Precision of ozone profile retrievals

The precision of the retrieved ozone profiles is a measure of the repeatability of the retrieval process. In orbit, the precision can be estimated by comparing a set of ozone profiles corresponding to limb scatter events which are closely collocated in both time and space *[Rault and Taha, 2007]*. Figure 5-1 shows the typical layout of the tangent point geo-locations for a series of LS events occurring over several consecutive NPP orbits, with each color corresponding to the left, center and right slits. This figure shows numerous collocated events when considering adjacent slits on consecutive orbits, which should allow for a detailed precision analysis. Moreover, the retrieval 1 σ uncertainties (evaluated as the square root of the covariance matrix diagonal terms) can be validated by comparing them with the ensemble standard deviation of the differences between OMPS/LP products and collocated measurements by other sensors, as was done by *[Rault and Taha, 2007]*.

A pre-launch estimate of the precision can be obtained by identifying the source of random errors in both the sensor and in factors affecting algorithm performance. The major source of uncertainty in the sensor is due to the Signal-to-Noise Ratio (SNR) of the limb radiance measurement. The smaller signals used in the high altitude range yield smaller SNRs, driving the scatter of the retrieved ozone values higher.

An estimate of the retrieval precision is obtained from the algorithm end-to-end testing presented in Figure 4-19 (right panels). These results were obtained with a series of 450 synthetic LS events corresponding to the SCIAMACHY/SAGE II coincidences. The forward model used in both the synthetic radiance simulation and the EDR included the finite spectral bandpass and the finite vertical slit function. Aerosol and RSAS retrievals are also included, as well as the effects of two-dimensional gridding and consolidation.

The precision budget also depends on atmospheric inhomogeneities, as well as on uncertainties on parameters such as temperature profile and scene albedo, as shown in Table 5-4 which reproduces results obtained by *[Larsen et al., 2005]*
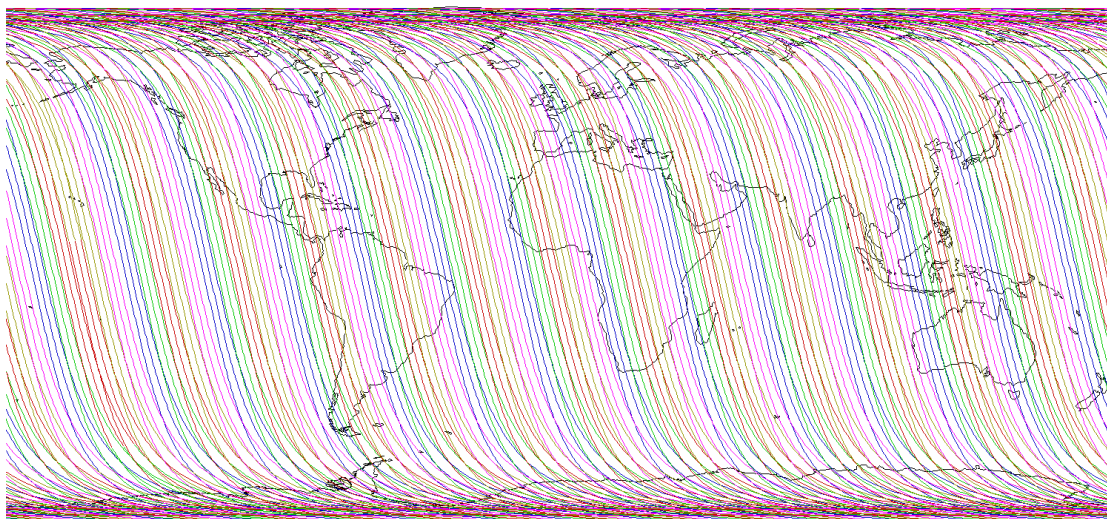
Figure 5-1. *Geo-locations of tangent point (TH=25km) for OMPS/LP over a 5 days period. Each color represents a day, respectively blue, green, red, yellow, and purple for days 1 to 5. Tracks are shown for the 3 slits.*

Table 5-4. *Effect of algorithm- and scene-related effects on ozone retrieval precision [Larsen et al., 2005]*

Effect	Tropopause-15 km	15 km-28 km	28 km – 50 km	50 km – 60 km
Inhomogeneity along LOS	3.0 %	1.2 %	1.2 %	1.2 %
Inhomogeneity cross track	2.0 %	1.0 %	1.0 %	1.0 %
Ozone absorption coef	0.15 %	0.15 %	0.38%	0.9 %
Aerosol	1.0 %	1.0 %	0.3 %	0.3 %
Neutral density	0.5 %	0.3 %	0.3 %	0.5 %
Surface reflectivity	0.2 %	0.1 %	0.1 %	0.1 %

Notes on Table 5-4:
   (1) The inhomogeneous scene effects along the LOS were estimated by considering an orbit worth of Advanced Very High-Resolution Radiometer (AVHRR) data to simulate the heterogeneous reflecting surface below the LOS for a wide range of conditions and subsequently run the baseline ozone retrieval algorithm *[Flittner, 2003]*.

(2) The cross-track inhomogeneity effect accounts for the inability of a 3 km wide slit observation to represent a 250 km cell. The magnitude of this effect was determined using gridded TOMS data (1 deg x 1 deg) at 60 deg S latitude, where level of horizontal variability can be expected to be high.

(3) The error due to ozone absorption coefficients only accounts for uncertainties on the atmospheric temperature profiles through the ozone cross section temperature dependence. (Estimated at 0.25%/K at altitudes greater than 28 km where UV wavelengths are used for ozone inversions, and at 0.1%/K at lower altitudes, where the ozone absorption coefficients in the Chappuis band are less temperature sensitive. Atmospheric temperature uncertainties were estimated at 3.5 K above 28 km and 1.5 K below 28 km).

(4) The error due to aerosol was evaluated over a large ensemble of simulated LS events for which both aerosol and ozone were retrieved simultaneously. The error shown are the maximum ozone errors retrieved for a wide range of background stratospheric aerosol number concentration, size distribution and refractive index as well as variability in the inhomogeneous surface reflectance field.

(5) The error on neutral number density corresponds to temperature uncertainties of 3.5 K above 28 km and 1.5 K below 28 km.

(6) The surface reflectivity allocations are based on the sensitivity of the reflectivity channels to sensor noise from the Rayleigh scattering reference channels.

5.3   Pointing accuracy and precision allocations

LS ozone retrievals depend crucially on correct tangent height registration of the measured radiance profile. Boresight pointing information derived solely from the NPP space platform state vector and attitude information probably will not be sufficiently accurate to achieve the desired ozone profile retrieval performance. The scene-based method which is implemented in both the SDR and EDR algorithm, namely the RSAS method, basically matches the measured and modeled Rayleigh scattered signal around 350 nm in the altitude range 20-35 km. At this altitude, the LS signal depends on the atmospheric temperature, aerosol loading and surface albedo. Typical uncertainties of the NCEP temperature data has been shown by *[Rault and Taha, 2007]* to yield one-sigma uncertainties of 200 m on RSAS TH registration. The two-step RSAS procedure (before and after aerosol retrieval) will enhance the RSAS performance to a degree which depends on solar zenith angle. An estimate of this latter uncertainty can be assessed from the results presented in Section 4.3.2. These results were obtained with a series of 450 LS events corresponding to SCIAMACHY/SAGE II coincidences over a full calendar year with a wide range of geo-locations. RSAS uncertainties are presented in Figure 4-18 histograms, with the following characteristics: bias (akin to accuracy) of 30 m and standard deviation (akin to precision) of 75 m.

5.4   Profile long-term stability

As noted by *[Larsen et al., 2005]*, the long-term stability of the OMPS/LP ozone product depends primarily on maintaining the calibration of the instrument.   The ozone retrieval

algorithm is designed with several normalizations (most notably tangent height normalization and channel combinations) to reduce sensitivity to calibration errors. The *[Larsen et al., 2005]* long-term stability performance estimate is reproduced in Table 5-5.

Table 5-5. *Estimate of long-term stability uncertainty on ozone profile [Larsen et al., 2005]*

Effect	Uncertainty	Ozone Uncertainty
Wavelength-independent calibration	0.25%	0.25%
Wavelength-dependent calibration	0.13%	0.52%
RSS Radiometric Performance		0.58%

6.0 REFERENCES

Anderson, S. M. and K. Mauersberger, (1992), Laser measurements of ozone absorption cross sections in the Chappuis band, *Geophys. Res. Lett., 19*, 933.

Anderson, J. (2002) (Private communication)

Bates, D.R. (1984), Rayleigh scattering by air, *Plan. and Space. Phys.*, **32**, 785-790.

Bevington, P.R. (1969), *Data reduction and error analysis for the physical sciences*, McGraw Hill, New York.

Bodhaine et al. (1999), *J. Atmos. Ocean Tech.* 16, 1854-1861

Bogumil, K., Orphal, J., Homann, T., Voigt, S., Spietz, P., Fleischmann, O.C., Vogel, A., Hartmann, M., Bovensmann, H., Frerick, J., Burrows, J.P. (2003), Measurements of molecular absorption spectra with the SCIAMACHY pre-flight model: instrument characterization and reference data for atmospheric remote-sensing in the 230–2380 nm region. *J Photochem. Photobiol*. A, 157-167.

Borchi, F., J.-P. Pommereau, A. Garnier, M. Pinharanda (2004), Evaluation of SHADOZ sondes, HALOE and SAGE II ozone profiles at the tropics from SAOZ UV-Vis remote measurements onboard long duration balloons, *Atmos. Chem. Phys. Discuss*., 4, 4945-4997.

Bourassa, A (2008) (Private communication)

Bovensmann, H,, J.P. Burrows, M. Buchwitz, J. Frerick, S. NoH, V.V. Rozanov, K.V. Chance, and A. P.H.Goede (1999), "SCIAMACHY Mission objectives and measurement modes," *Journal of the Atmospheric Sciences,* vol. 56, no. *2,* pp. 127–150.

Brion, J., A. Chakir, J. Charbonnier, D. Daumont, C. Parisse and J. Malicet (1998), Absorption Spectra Measurements for the Ozone Molecule in the 350-830 nm Region, *J. Atm. Chem.* 30, 291-299.

Burkholder, J.B. and R.K. Talukdar (1994), Temperature dependence of the ozone absorption spectrum over the wavelength range 410 to 760 nm, *Geophys. Res. Lett., 21*, 581-584.

Colina, L., R.C. Bohlin and F. Castelli (1996), The 0.12-2.5 micron absolute flux distribution of the sun for comparison with solar analog stars, *Astron. J.*, 112, 307.

Cunnold, D.M., E-S. Yang, H-J. Wang, and P. Jing (2004), Mid-latitude tropospheric ozone columns and trends calculated from TOMS - PV-mapped SAGE stratospheric columns, *Proceedings of the XX Quadrennial Ozone Symposium*, 1-8 June 2004, Kos, Greece, Zerefos, C.S. (ed.).

Daumont, D., J. Brion, J. Charbonnier, and J. Malicet (1992), Ozone UV spectroscopy I: Absorption cross-sections at room temperature, *J. Atmos. Chem.,* 15, 145-155.

Degenstein, D. A., Bourassa, A. E., Roth, C. Z., and Llewellyn, E. J.: Limb scatter ozone retrieval from 10 to 60 km using a multiplicative algebraic reconstruction technique, *Atmos. Chem. Phys*., 9, 6521-6529, 2009.

Eichmann, K.-U., J.W. Kaiser, C. von Savigny, A. Rozanov, V.V. Rozanov, H. Bovensmann, M. von König, and J.P. Burrows (2004), SCIAMACHY limb measurements in the UV/Vis spectral region: first results, *Adv. Space Res., 34*, 775-779.

Flittner,D.P.K. Bhartia, B.M., Herman (2000), O_3 profiles retrieved from limb scatter measurements: Theory, *Geophys. Res. Lett*., 27, 2601-2604.

Flittner, D. (2003), First Limb Workshop, Bremen April 14-16, 2003.

Flynn, L.E., Seftor, C.J., Larsen, J.C., Xu P. (2007), The Ozone Mapping and Profiler Suite (OMPS), Earth Science Satellite Remote Sensing, Springer-Verlag and Tsinghua University Press.

Frederick, J.E, R. P. Cebula, and D. F. Heath (1986), Instrument characterization for the detection of long-term changes in stratospheric ozone: An analysis of the SBUV/2 radiometer, *J. Atmos. Oceanic Technol.*, **3**, 472-480.

Graf, P.H., I. Becker, M. Chrisp, M. Dittman, W. Fowler, P. Hendershott, G. Jaross, J. Larsen, P. Mehalko, D. Michaels, V. Minerva, J. Qu, R. Rathburn, J.V. Rodriguez, C. Seftor, R. Schwiesow, H.F. Snell, T.J. Swissler, R. Tarde and C. Wellemeyer (2000), The Preliminary design of the Ozone Mapping and Profiler Suite (OMPS), in *Atmospheric Ozone : Proceedings of the Quadrennial Ozone Symposium*, Sapporo, Japan 3-8 July 2000, Edited by R.D. Bojkov AND K. Shibasaki, International Ozone Commision, 401-402, (http://eic.ipo.noaa.gov/IPOarchive/SCI/sensors/omps/graf-sapporo-extabs%5B1%5D.pdf).

Gordley, L. L., Russell III, J. M., Mickley, L. J., Frederick, J. E., Park, J. H., Stone, K. A., Beaver, G. M., McInerney, J. M., Deaver, L. E., Toon, G. C., Murcray, F. J., Blatherwick, R. D., Gunson, M. R., Abbatt, J. P. D., Mauldin III, R. L., Mount, G. H., Sen, B., and Blavier, J.-F. (1996), Validation of nitric oxide and nitrogen dioxide measurements made by the Halogen Occultation Experiment for UARS platform, *J. Geophys. Res.*, 101, 10 241–10 266.

Haley, C.S., C. von Savigny, S. Brohede, C.E. Sioris, I.C. McDade, E.J. Llewellyn, and D.P. Murtagh (2004), A comparison of methods for retrieving stratospheric ozone profiles from OSIRIS limb-scatter measurements, *Advances in Space Research, 34*, 769–774.

Harder, J. W., J. W. Brault, P. V. Johnston, and G. H. Mount (1997), Temperature dependent NO_2 cross sections at high spectral resolution, *J. Geophys. Res.,* 102, 3861-3879.

Heath, D. F., A. J. Krueger, H. R. Roeder, and B. D. Henderson (1975), The solar backscatter ultraviolet and total ozone mapping spectrometer (SBUV/TOMS) for Nimbus G, *Optical Engineering*, **14**, 323-331.

Herman, B.M., D.E. Flittner, R.D. McPeters, and P.K. Bhartia (1995a), Monitoring atmospheric ozone from space limb scatter measurements, *Proc. SPIE Vol. 2582*, 88-99.

Herman, B.M., T.R. Caudill, D.E. Flittner, K.J. Thome, and A. Ben-David (1995b), Comparison of the Gauss-Seidel spherical polarized radiative transfer code with other radiative transfer codes, *Appl. Opt.*, *34*, 4563-4572.

Hilsenrath, E., R.P. Cebula, M.T. Deland, K. Laamann, S. Taylor, C. Wellemeyer, and P.K. Bhartia (1995), Calibration of the NOAA-11 Solar Backscatter Ultraviolet (SBUV/2) Ozone Data Set from 1989 to 1993 using In-Flight Calibration Data and SSBUV, *J. Geophys. Res.*, **100**, 1351-1366.

Janz, S.J., E. Hilsenrath, D. Flittner, D. Heath (1996), Rayleigh scattering attitude sensor, *Proc. SPIE*, 2831, 146-153.

Jaross, G., et al. (2010), Algorithm Theoretical Basis Document (ATBD) for the Sensor Data Record (SDR) Algorithm of the Ozone Mapping and Profiler Suite (OMPS) Limb Profiler.

Kalnay, E., et al (1996), The NCEP/NCAR Reanalysis Project. *Bull. Amer. Meteor. Soc., 77*, 437-471.

Kurucz, R.L. (2005) High resolution irradiance spectrum from 300 to 1000 nm, presented at AFRL Transmission Meeting, 15-16 June 2005, Lexington, Mass., Astro-ph/0605029.

Larsen, J., et al. (2005), Algorithm theoretical basis document (ATBD) (Limb profile ozone) for the Ozone Mapper and Profiler Suite (OMPS) of the National Polar-orbiting Operational Environmental Satellite System (NPOESS) Program, Doc. In0092a-107, Ball Aero. Syst. Div., Boulder, Col. (http://eic.ipo.noaa.gov/IPOarchive/SCI/atbd/atbd_lp.pdf)

Leitch, J.W., J.V. Rodriguez, M.G. Dittman, D. Frazier, B.K. McComas, R.H. Philbrick, D. Wasinger, Debra, T.J. Valle, T. Dixon, D. Dooley, R. Munzer, J.C. Larsen, (2003), Limb scatter ozone profiling sensor for the NPOESS ozone mapping and profiler suite (OMPS), *Optical Remote Sensing of the Atmosphere and Clouds III*. Edited by Huang, Hung-Lung; Lu, Daren; Sasano, Yasuhiro. Proc. Of the SPIE, Vol.4891,pp.13-21. (http://eic.ipo.noaa.gov/IPOarchive/SCI/sensors/omps/LimbScatterOzoneProfilingSystemforOMPS.pdf)

Llewellyn, E.J, et al. (2004), The OSIRIS instrument on the Odin spacecraft, *Canadian Journal of Physics*, 82, 411-422.

Loughman R. P., D. E. Flittner, B. M. Herman, P. K. Bhartia, E. Hilsenrath, and R. D. McPeters (2005), Description and sensitivity analysis of a limb scattering ozone retrieval algorithm, *J. Geophys. Res.*, 110, D19301, doi:10.1029/2004JD005429

Loughman R. P., E. Griffioen, L. Oikarinen, O.V. Postylyakov, A. Rozanov, D.E. Flittner and D.F. Rault (2004), Comparison of radiative transfer models for limb-viewing scattered sunlight measureeements, *J. Geophys. Res.*, 109, D06303, doi: 10.1029/2003JD003854.

Malicet, J., D. Daumont, J. Charbonnier, C. Parisse, A. Chakir and J. Brion (1995), Ozone UV Spectroscopy. II. Absorption cross-sections and temperature dependence, *J. Atm. Chem.,* 21, 263-273.

Mauldin, L. E., R. Salikhov, S. Habib, A. Vladimirov, D. Carraway, G. Petrenko, J. Comella (1998), Meteor-3M-/Stratospheric Aerosol and Gas Experiment III (SAGE III), *Proc. SPIE*, 3501, 355-365.

McCormick, M. P., J. M. Zawodny, R. E. Veiga, J. C. Larsen, and P.-H. Wang, (1989). An Overview of SAGE I and II Ozone Measurements, *Planet. Space Sci.*, 37, 1567-1586.

McPeters, R. D., and W. D. Komhyr (1991), Long-Term Changes in the Total Ozone Mapping Spectrometer Relative to World Primary Standard Dobson Spectrometer 83, *J. Geophys. Res.*, *96*(D2), 2987–2993.

McPeters, R.D., S.J. Janz, E. Hilsenrath, T.L. Brown, D.E. Flittner, and D.F. Heath (2000), The retrieval of O_3 profiles from limb scatter measurements: Results from the shuttle ozone limb sounding experiment, *Geophys. Res. Lett.*, *27*, 2597-2600.

McLinden, C. A., Olsen, S., Hannegan, B., Wild, O., Prather, M. J., and Sundet, J., (2000), Stratospheric ozone in 3-D models: A simple chemistry and the cross-tropopause flux, *J. Geophys. Res.,* 105(D11), 14 653–14 665.

Petelina, S.V., D.A. Degenstein, E.J. Llewellyn and N.D. Lloyd (2006) Correlation of PMC relative brightness and altitudes observed by Odin/OSIRIS in the Northern Hemisphere in 2002–2003 *Journal of Atmospheric and Solar-Terrestrial Physics*,doi:10.1016/j.jastp.2005.08.005

Rault,D.F. (2005), Ozone profile retrieval from Stratospheric Aerosol and Gas Experiment (SAGE III) limb scatter measurements, *J. of Geophys. Res.*, 110, D09309, doi:10.1029/2004JD004970

Rault, D.F, (2006), Development of high accuracy Tangent Height registration for Limb Scatter measurements, AGU Fall conference, San Francisco, CA

Rault, D.F. and G. Taha (2007), Validation of ozone profiles retrieved from SAGE III limb scatter measurements*, J. Geophys. Res., 120*, doi:10.1117/12.626618.

Rault, D.F. and R. Loughman (2007), Stratospheric and upper tropospheric aerosol retrieval from limb scatter signals, *Proceedings of SPIE Remote Sensing conference*, Florence

Rodgers, C.D. (1976), Retrieval of atmospheric temperature and composition from remote measurements of thermal radiation, *Rev. Geophys. And Space Phys.,* **14**, 609-624.

Rodgers, C.D. (2000) *Inverse methods for atmosphere sounding: Theory and practice*, 238 pp., World Scientific Publishing Co, Singapore.

Rothman, L.S., R.R. Gamache, R.H. Tipping, C.P. Rinsland, M.A. Smith, D.C. Benner, W.M. Devi, J.M. Flaud, C. Camy-Peyret, A. Perrin, A. Goldman, S.T. Massie, L.R. Brown and R.A. Toth (1992). The HITRAN Molecular Database Editions of 1992, *J. Quant. Spectrosc. Radiat. Transfer, 48*, 469-507.

Rusch, D. W., G.H. Mount, C.A. Barth, R.J. Thomas and M.T. Callan (1984), Solar mesopshere explorer ultraviolet spectrometer: Measurements of ozone in the 1.0-0.1 mbar region, *J. Geophys. Res*., 89, 11,677-11,687.

Russell, J.M., S.M. Bailey, L.L. Gordley, D.W. Rusch, M. Horanyi, M.E. Hervig, G.E. Thomas, C.E. Randall, D.E. Siskind, M.H. Stevens, M.E. Summers, M.J. Taylor, C.R. Englert, P.J. Espy, W.E. McClintock, and A.W. Merkel (2008), The Aeronomy of Ice in the Mesosphere (AIM) mission: Overview and early science results, *J. Atmo. Sol. Terr. Phys*., 71, 289-299, doi:10.1016/j.jastp.2008.08.011.

Thomason, L. W., Poole, L. R., and Deshler, T. R. (1997), A global climatology of stratospheric aerosol surface area density as deduced from SAGE II: 1984–1994, *J. Geophys. Res*., 102, 8967–8976.

Thomason, L. W. (Ed.) (2006), *Assessment of Stratospheric Aerosol Processes*, 1 –322 pp., World Climate Research Program

von Savigny, C., E. P. Ulasi, K.-U. Eichmann, H. Bovensmann, and J. P. Burrows (2005), Detection and mapping of polar stratospheric clouds using limb scattering observations, *Atmos. Chem. Phys. Discuss*., SRef-ID: 1680-7375/acpd/2005-5-7169.

Wang, P.-H., M.P. McCormick, L.R. Poole, W.P. Chu, G.K., Yue, G.S. Kent and K.M. Skeens (1994), Tropical high cloud characteristics derived from SAGE II extinction measurements, *Atmos. Res*., 34, 53-83.

Wang, H. J., D. M. Cunnold, L. W. Thomason, J. M. Zawodny, and G. E. Bodeker, (2002), Assessment of SAGE version 6.1 ozone data quality, *J. Geophys. Res.,* 107(D23), 4691, doi:10.1029/2002JD002418.

Yue, G. K. (2000) Retrieval of Stratospheric Aerosol Size Distributions and Integral Properties From Simulated Lidar Backscatter Measurements, *Appl. Opt*. **39**, 5446-5455.

APPENDIX A. ALTERNATIVE EDR ALGORITHM. MULTIPLE LINEAR REGRESSION (MLR)

The Doublet/Triplet formulation is a well proven technique and will be relied on for routine operations. Multiple Linear Regression (MLR) *[Bevington, 1969]* is an alternative technique which offers additional diagnosis capability to analyze the dataset spectral characteristics and identify instrument effects through residual analysis. MLR is basically a technique to fit the measured spectra with ozone absorption spectral features. For OMPS/LP, it will be used directly on the CCD pixel map data, i.e. before the data is re-gridded onto a uniform Cartesian grid. As shown in Figure A-1, MLR is applied on each row of pixels, for each of the 4 gains, and each of the 3 slits. Along a row, the measured data $I(\lambda)$ is regressed using two orthogonal functions, namely the ozone cross section $\sigma(\lambda)$ and a closure polynomial $polyn((\lambda)$.

$$\log\left[\frac{I(\lambda)}{\left(\frac{S(\lambda)}{\lambda}\right)}\right] = -CD*\sigma \ \lambda \ + \ polyn(\lambda \qquad\qquad \text{[Equation A1]}$$
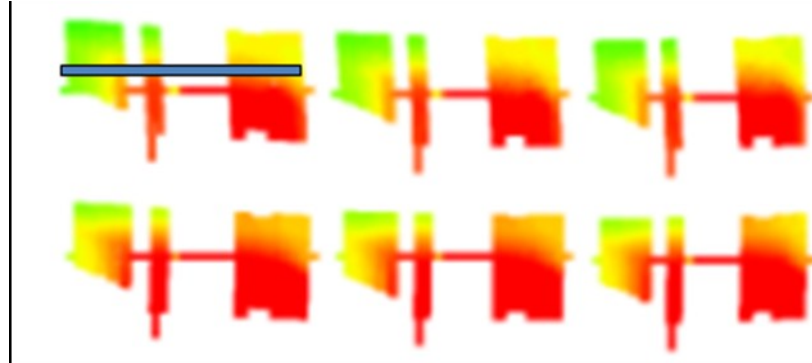

Figure A-1. *Multiple Linear Regression on CCD array.Technique is applied consecutively on individual rows of pixels, for each gain and each slit*

The measured data is normalized by the solar radiance $S(\lambda)$ and the Rayleigh λ^4 term. Equation A1 is solved for the effective column density $CD*$. Because of "smile" effect on the CCD array, the pixels along a CCD array row do not observe the same tangent height TH. Hence

$$CD* = \ CD(TH) + \frac{\partial \ CD}{\partial \ TH}\Delta \ TH \qquad\qquad \text{[Equation A2]}$$

where TH is a mean tangent height defining the pixel row and ΔTH represents the altitude offset of each row pixel with respect to the mean value TH. Equation A1 can then be rewritten as:

$$\log\left[\frac{I(\lambda)}{\left(\frac{S(\lambda)}{\lambda}\right)}\right] - \frac{\partial CD}{\partial TH}\Delta TH\sigma\lambda = -CD(TH)\sigma\lambda + polyn(\lambda)$$ 　　　　[Equation A3]

Equation A3 is solved by iterations to retrieve *CD(TH)*. In the first iteration, the second term on the left side of the equation is zero. Subsequently, it is evaluated by differentiation of the column density *CD(TH)*. This analysis is performed for each of 4 gains, separately for the Hartley/Huggins and Chappuis bands, and consecutively for each of the 3 slits. The residuals of this process will be analyzed to assess performance of the sensor.

The ozone density profiles are retrieved from the column density *CD(TH)* using Rodgers' optimal estimation method *[Haley et al., 2004]*. The measurement vectors are:

$$y = CD(TH)$$ 　　　　[Equation A4]

using data from the unsaturated part of the 4 gain images.

The "forward model" is:

$$F(x) = CD_{model}(TH, x)$$ 　　　　[Equation A5]

using the same CCD pixels as the ones considered to analyze data, where $CD_{model}(TH,x)$ is the MLR effective column density evaluated as shown in Equation A1, but with $I(\lambda)$ being evaluated on each CCD pixel with the forward model, using the current ozone density as the state vector *x*.

The kernel matrix *K(x)* is the path length matrix, which can be evaluated as:

$$K(x) = \frac{1}{\sigma_{TH}(\lambda)}\frac{\partial\log[I(\lambda, TH)]}{\partial}$$ 　　　　[Equation A6]

where $\sigma_{TH}(\lambda)$ is the mean ozone cross section along the line of sight at tangent height *TH*.

Figures A-2 and A-3 show typical retrieval results, respectively for effective column density and ozone profile.
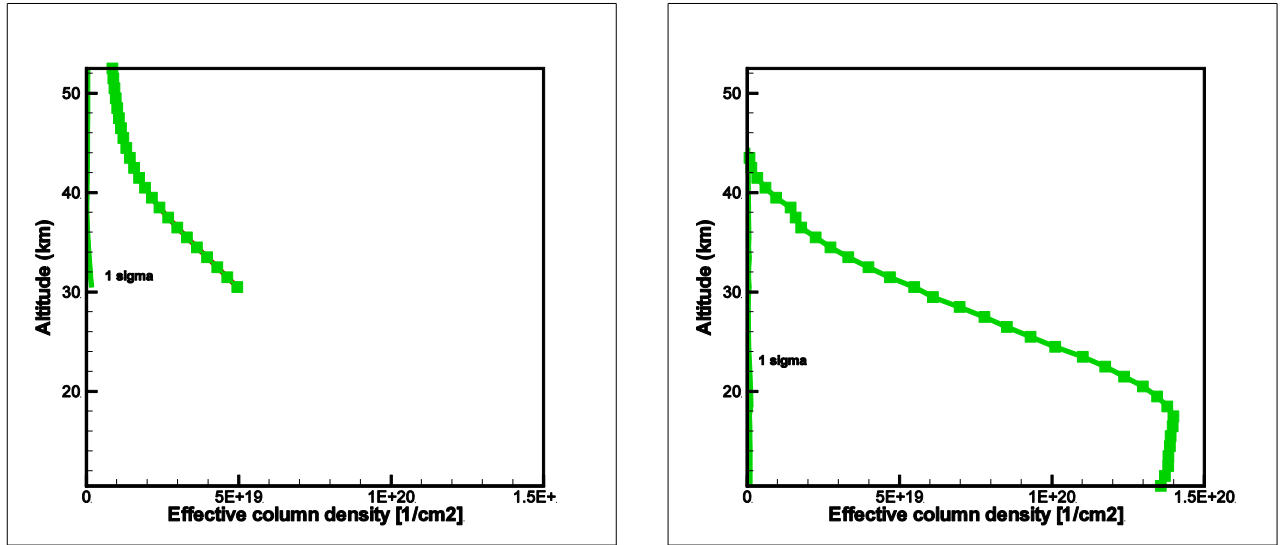
Figure A-2. MLR effective column density. Left panel corresponds to Hartley/Huggins bands, whereas right panel corresponds to Chappuis band.
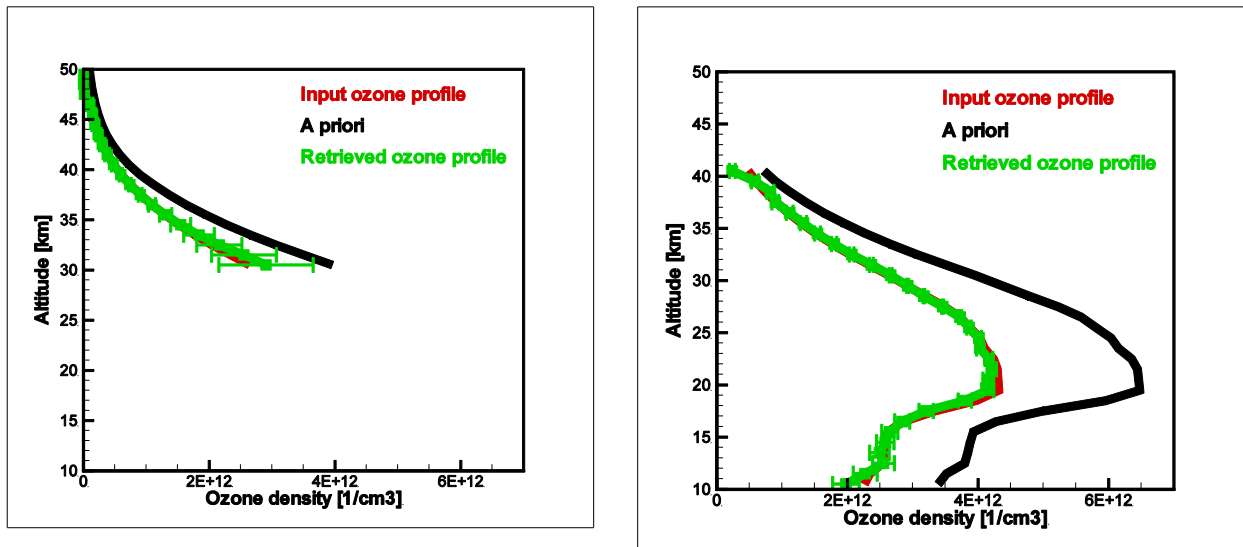

Figure A-3. Retrieved ozone density profile using MLR. Left panel corresponds to Hartley/Huggins bands, whereas right panel corresponds to Chappuis band. Black lines represent the a-priori ozone profile.

APPENDIX B. DIRECT OPTIMAL ESTIMATION METHOD (DOE)

The Direct Optimal Estimation method (DOE) tries to directly infer ozone vertical distribution from the large ensemble of measurements made by individual CCD pixels. The problem is necessarily over dimensioned with typically 100 unknowns (ozone density at 50 altitudes, 2 aerosol extinction at 25 altitudes) and potentially thousands of measurements. The algorithm is based on the optimal estimation method which is used to compare the measured data with a set of radiances simulated with a multiple scatter forward model. In this Appendix, the forward model, which establishes the limb radiance vertical and spectral characteristics on an unstructured grid is first described. The DOE algorithm is then explained and its performance is illustrated using synthetic datasets.

By circumventing the need for (1) data remapping and (2) explicitly performing the gain consolidation, the DOE method has the potential for higher quality products and improved data quality assessment:

-dead or missing pixels can easily be removed from the dataset

-retrievals can alternatively be independently performed for each gain setting, thus
 yielding four ozone profiles which can then be compared to identify instrument effects
 for each of the three slits.

-the retrieval vertical resolution is optimized since data smearing induced by re-gridding
 is avoided

-cloud detection, and spectral/spatial registrations can be done on raw data (along CCD
 pixels row and columns), thus minimizing errors and biases induced by data
 preprocessing.

B.1   Forward model on unstructured grid

The forward model described in Section 3.3 evaluates limb radiances on a gridded two-dimensional Cartesian frame (very high resolution in wavelength λ dimension, medium resolution in tangent height TH). For DOE application, the forward model must be able to evaluate radiances and radiance partial derivatives at the center of each pixel, i.e. at arbitrary $[\lambda, TH]$. To obtain limb radiances on this unstructured grid, the gridded high resolution modeled radiances are convolved with the instrument slit function centered at $[\lambda, TH]$:

$$Rad[\lambda, TH] = \iint I(\lambda_i, TH_i) f(\lambda_i - \lambda, TH_i - TH) d\lambda_i \, lTH_i \qquad [\text{ Equation B.1 }]$$

where $I(\lambda_i, TH_i)$ is the limb radiance evaluated on the high resolution Cartesian grid $[\lambda_i, TH_i]$, and $f(\lambda_i-\lambda, TH_i-TH)$ is the laboratory measured instrument slit function at $[\lambda, TH]$. The partial derivatives must also be evaluated at the un-gridded $[\lambda, TH]$ location. The partial derivative of the limb radiance at $[\lambda, TH]$ with respect to a parameter x_j in layer j is approximated as:

$$\frac{dRad}{dx_j}(\lambda \; TH) = 1-w)\frac{dRad}{dx_j}(\lambda \; lTH_i) + w\frac{dRad}{dx_j}(\lambda \; lTH_{i+}) \qquad [\text{ Equation B.2 }]$$

where the weighting factor $w = (TH-TH_i)/(TH_{i+1}-TH_i)$, TH_i and TH_{i+1} are the gridded tangent heights above and below the reference tangent height TH, as illustrated in Figure B-1. Equation

B.2 applies only for shells not containing the tangent point. For this latter shell, the partial derivative is scaled relatively to the geometrical path length within the shell:

$$\frac{dRad}{dx_j}(\lambda\ TH) = \frac{L}{L_i}\frac{dRad}{dx_j}(\lambda\ TH_i)$$ [Equation B.3]

where L is the geometric path length corresponding to the tangent height TH, whereas L_i is reference path length within shell i, ie, the path length of the ray travelling through the middle of layer i.
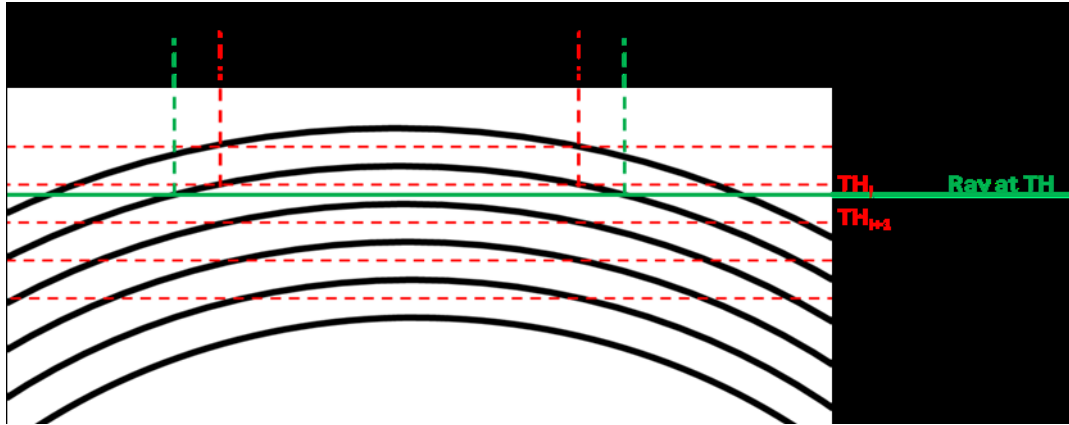

Figure B-1. *Limb radiance geometry. Evaluation of radiances and radiance partial derivatives*

B.2 Retrieval algorithm methodology

As shown in Section 3.5, the ozone profile retrieval from limb scatter measurements is sensitive to a series of parameters, among which: the accuracy of spectral and spatial registrations, aerosol density, and to a lesser extent, surface albedo and NO_2 density. The accuracy/precision requirements expected out of the OMPS/LP demand that these parameters be known to a relatively high accuracy. The OMPS/LP data preprocessor will use (1) spacecraft position and attitude information to register the tangent height TH for each CCD pixel, and (2) weekly solar irradiance measurements to calibrate the spectral registration of each CCD pixel. However, the accuracy of these registrations needs to be verified and, if necessary, corrected, for each limb scatter event. Aerosol density and effective albedo typically vary in time and space due to dust transport and cloud/land-cover respectively, and must also be retrieved for each event. The NO_2 density varies both spatially and in local solar time, but its effect on ozone retrieval is relatively small and can be adequately modeled.

To account for these effects, the retrieval strategy adopted for the OMPS/LP ozone profile retrieval includes the following steps:

   (1) Wavelength registration check, and adjustment if necessary, using the solar Fraunhofer lines in the UV
   (2) First order estimation of NO_2 from climatology, corrected for local solar time effects
   (3) Cloud height determination, using long wavelength channels with weak gaseous absorption

(4) *TH* registration check, and adjustment if necessary, using a scene-base method, such as the Rayleigh Scatter Altimeter Sensor (RSAS) technique *[Janz et al. 1996]* or alternatively, the Multiple Wavelengths *TH* Registration Method *[Rault 2006]*

(5) Surface albedo determination and aerosol retrieval (aerosol extinction and size distribution), using spectral channels with weak gaseous absorption

(6) Repeat TH registration check/adjustment. This step is necessary since the RSAS *TH* registration method is sensitive to stratospheric aerosol content

(7) Ozone retrieval, using radiance data from both the UV and visible wavelength channels, respectively for high altitudes (30-60km) and low altitudes (Clout top or 10km-40km)

These steps are mostly independent from each other, since each step is using a different part of the spectral range measured by OMPS/LP.

B.2.1 Spectral registration

The UV solar and ozone absorption spectra both exhibit rich fine structures with rapidly varying features. These features can be captured by selecting a series of CCD pixel rows for each slit and each aperture, as illustrated in Figure B-2. Along these rows, the limb observations on each pixel can be compared with the radiance values computed with the forward model. The measured and modeled data spectra are first both filtered with a low-frequency filter to obtain the high frequency spectra $D(\lambda)$ and $M(\lambda)$ respectively for the measured and modeled radiances. The wavelength scale shift $\Delta\lambda$ is identified by optimizing the correlation between $D(\lambda)$ and $M(\lambda+\Delta\lambda)$, as described in Section 3.5.1.
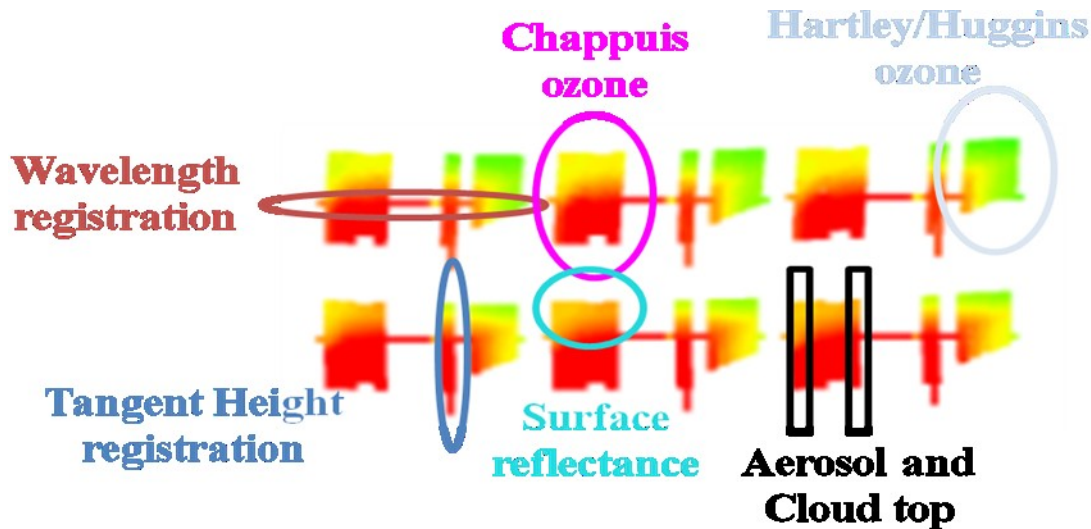

Figure B-2. *CCD array layout showing pixel regions used for each retrieval.*

B.2.2 Surface albedo

The Earth surface is assumed to be Lambertian and spatially homogeneous, and its albedo α is assumed to only depend on wavelength λ. To estimate $\alpha(\lambda)$ from limb scatter observations, the measured data is compared to model radiances in visible/IR spectral regions with weak gaseous absorption and in the tangent height range of 35-45km. This height range is located mostly above the aerosol layer and should be minimally contaminated by straylight. For each wavelength range considered (typically centered around 500, 680, 780 and 860nm), the measured limb scatter

radiance is compared with model radiances computed at three assumed surface reflectances, namely, 0.1, 0.5 and 0.9, and α(λ) is subsequently evaluated by interpolation. In orbit, the sensor will undergo a weekly radiometric calibration and it is therefore expected that surface albedo can be retrieved at sufficient accuracy (<10%) to allow accurate retrieval of trace gases and aerosol.

B.2.3 Rayleigh Scattering Attitude Sensor (RSAS)

The RSAS method is described in Section 3.5.2.1. In the DOE, the RSAS technique is applied on a series of M columns of CCD pixels with wavelengths close to 350 nm, as shown in Figure B-2. The ΔTH shift correction for each slit and each aperture is evaluated as the mean RSAS offset for all the M pixel columns.

B.2.4 Cloud top height

The OMPS/LP long wavelength channels are sensitive to the presence of clouds. Clouds appear as either faint or sharp discontinuities of the radiance vertical profiles, whether they correspond to thin cirrus or tropospheric water clouds.
A simple algorithm is used to infer the cloud presence. It relies on the computation and comparison of the derivatives of the radiance I with respect to TH: dI/dTH_{back} and dI/dTH_{forw}. dI/dTH_{back} is the backward derivative (evaluated using data points below TH) whereas dI/dTH_{forw} is the forward derivative (evaluated using data points above TH). Two threshold values are used: the first one differentiates thin clouds from noise, while the second one differentiates between thin and thick clouds. This cloud detection algorithm is used on a set of columns of CCD pixels, positioned at wavelengths with weak absorption, namely 675, 740, 870 and 920nm.

B.2.5 Aerosol retrieval

The presence of aerosol in the atmosphere has a clear effect on the limb scatter radiance, as was shown in Section 3.5.5. However, the information content of the limb scatter radiance data over the relatively narrow 500-960nm spectral range is not sufficient to allow the retrieval of more than two parameters per altitude bins, such as the extinction coefficient at a given wavelength and a moment of the size distribution. Assumptions have to be made on the aerosol microphysics, such as uni-modal size distribution of spherical sulfate Mie scattering particles. To facilitate the aerosol retrieval, the algorithm relies on a presumed log-linear relationship between aerosol extinction β and wavelength λ

$$\log[\beta(\lambda, H)] = \iota(H)\log(\lambda) + \nu(H) \qquad\qquad \text{[Equation B.4]}$$
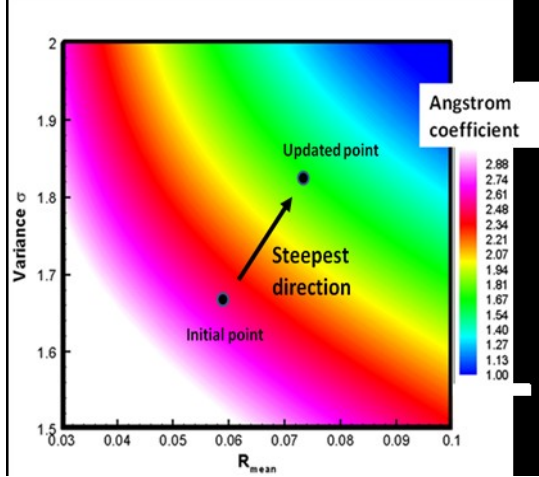
Figure B-3. *Angstrom coefficients for a set of uni-modal log-normal size distribution parameters mean radius R$_{mean}$ and variance σ. Microphysics update follows path of steepest slope.*

where *β(λ,H)* is the aerosol extinction coefficient at wavelength *λ* and altitude *H*. The coefficients *a* and *b* are assumed to be function of altitude only. Alternatively, the problem can be thought of retrieving two extinction coefficients at wavelengths *λ$_1$* and *λ$_2$*, with the extinction coefficient *β* at wavelength *λ* defined as:

$$\log(\beta \lambda TH]) = A\log(\beta \lambda_1 TH]) + 1 - A)\log(\beta \lambda_2, TH])$$ [Equation B.5]

where *A = log(λ/λ$_2$)/log(λ$_1$/λ$_2$).*

The retrieval algorithm considers the ensemble of CCD pixels in a series of spectral ranges (470-525, 670-680, 740-750, 770-900) and retrieves the extinction coefficients at two wavelengths, namely *λ$_1$* = 520nm and *λ$_2$* = 870nm. The retrieval algorithm uses the optimal estimation method, with the following definitions:

  -measurement vector = *y(i)* = *Rad[λ,TH] / Ref[λ]*, where *Rad[λ,TH]* refers to the measurement on pixel *I* (registered at wavelength *λ* and tangent height *TH*). *Ref[λ]* is the high altitude reference, which is evaluated using the measurements made by all CCD pixels corresponding to high *TH* and a wavelength close to *λ*. All four gains of each aperture are considered when selecting the CCD pixels to be used. The variance associated with each pixel is related to the Signal-to-Noise ratio of the measurement on that pixel.

  -state vector = *x(1:Nvar)* = *β[λ$_1$,TH$_{1:Nvar}$]*
              x(Nvar+1: Nvar+Nvar) = *β[λ$_2$,TH$_{1:Nvar}$]*
  where *Nvar* is the number of altitude bins at which the retrieval is performed (typically retrieval is done from 15 to 40 km)

  -forward model vector = *F(x$_{1:2xNvar}$)* = *Mod[λ,TH] / ModRef[λ]*, where *Mod[λ,TH]* refers to the forward model computed for the pixel *i* (registered at wavelength *λ* and tangent height *TH*). *ModRef[λ]* is the high altitude   reference, which is evaluated using the same CCD pixels and the same method as for the measurement vector.

The retrieval process is iterative. At the end of each iteration, the effective Angstrom coefficient is estimated from the mean ratio $\beta(\lambda_1,H)/ \beta(\lambda_2,H)$ evaluated over a set range of altitudes (18<H<28 km). The mean Angstrom coefficient is then used to estimate the mean radius R_{mean} and standard deviation σ of a uni-modal log-normal size distribution, which is in turn used to evaluate the Mie phase function and scattering coefficients in the forward model. As shown in Figure B-3, the functional dependence of the Angstrom coefficient with respect to R_{mean} and σ is multi-valued, ie, a given Angstrom coefficient corresponds to a range of $[R_{mean},\sigma]$ pairs. The algorithm upgrades its $[R_{mean},\sigma]$ values in a direction perpendicular to the iso-Angstrom curves, as illustrated in Figure B-3. *A-priori* values for the extinction coefficients $\beta(\lambda_1,H)$ and $\beta(\lambda_2,H)$ are obtained from SAGE II climatology *[Thomason, 1997]*

B.2.6 Ozone retrieval

The ozone retrieval is considering all the CCD pixels in the wavelength range 280-330nm (Hartley-Huggins bands) and 500-680 nm (Chappuis bands). The doublet/triplet algorithm described in Section 3.5.6 is also used in DOE to construct the optimal estimation measurement vectors. These vectors are made of wavelength pairs (or doublets) in the UV, and triplets in the visible.

The high altitude normalization is performed using an approach similar to the one described for the aerosol retrieval, using CCD pixels in the altitude range 62-68 km for the Hartley/Huggins bands and 42-48 km for the Chappuis band. For the doublet reference $D_{ref}(TH)$ of the Hartley-Huggins retrieval, CCD pixels are selected in a non-absorbing region (340-360nm) with a tangent height close to *TH*. For the two triplet references $T_{ref}(TH)$ of the Chappuis band, CCD pixels are selected in non-absorbing regions on either side of the Chappuis band (490-510 nm and 66-680 nm) with a tangent height close to *TH*. The forward model vector $F(x)$ is constructed in a similar fashion, using the same CCD pixels for normalization and doublet/triplet construction as the ones selected for the data measurement vectors.

Since the number of measurements (typically 80000 CCD pixels) is much larger than the number of unknowns (typically 50 ozone densities), the solution convergence is fast and only requires 2 to 3 iterations. With typical OMPS/LP SNR levels, the DOE averaging kernels are typically close to the identity matrix, which ensures that *a-priori* values have little effect on the retrieved profiles.

For each slit, the retrieval can be performed for each of the four gains independently or alternatively by combining all four gain data into a single measurement vector. The first method will be used in the initial operation phase to identify instrument effects, while the second method will be relied on once the sensor performance is better known.

All the downloaded CCD pixels within the Hartley/Huggins and Chappuis bands can be used. However, to minimize CPU requirements, an optimal subset of pixels has been identified and used with negligible effect on accuracy and precision. Eventual loss of CCD pixels during the course of operations can be easily accounted for by modifying the selected subset of pixels.

B.3 Performance of DOE algorithm

The DOE algorithm has been tested in two different ways:
1. using a two-dimensional gridded radiance input, to test the gas and aerosol retrieval algorithms

2. using a set of ungridded synthetic CCD radiance inputs, to test the capability of the DOE algorithm to (a) ingest unstructured CCD data, (b) perform the gain consolidation process and (3) retrieve aerosol and ozone products.

B.3.1 DOE testing with gridded data

The first test series is conducted on a relatively large synthetic dataset. This dataset was generated by the forward model and is composed of 450 limb scattering events, each one corresponding to a co-location of a SAGE II occultation measurement with a SCIAMACHY limb scattering measurement over a one-year period. This synthetic LS dataset was described in Section 4.2.1.2. Expected values of the OMPS/LP SNR are used to simulate the noise on the synthetic radiances for each CCD pixel. Assumption is made that 10% of the CCD pixels are unavailable (either "hot" or "dead"). The performance of the RSAS module is illustrated on Figure B-4 which shows a histogram of the RSAS offset. The mean bias is 120 m whereas the standard deviation is 175 m. Figure B-5 (left and center panels) presents the results of the ozone retrieval in terms of mean bias and standard deviation. Since the forward model includes the spatial convolution with the instrument elevation slit function, the input ozone profile used for the comparisons are similarly convolved. The Hartley-Huggins retrieval has accuracy better than 3%. The standard deviation is about 2-3% from 30 to 60 km. The Chappuis band retrieval shows an accuracy of better than 4% from 20 to 40 km with a standard deviation of 2-5%. A fairly large number of events in the dataset correspond to high latitudes and consequently exhibit low ozone density at lower altitudes. As a consequence, relative errors below 20 km are significant. In all cases the standard deviation and the retrieval 1-σ uncertainty are in close correlation, which indicates that the error dispersion is mostly due to "measurement" random noise as well as ozone sensitivity decrease at low and high altitudes for each absorption band. The performance of the aerosol retrieval is illustrated in Figure B-5 (right panel), which compares the mean aerosol profile to the assumed input profile. Aerosol can be retrieved with an accuracy of about 20%, which should be sufficient to adequately ascertain and correct for the aerosol effect on ozone retrieval.
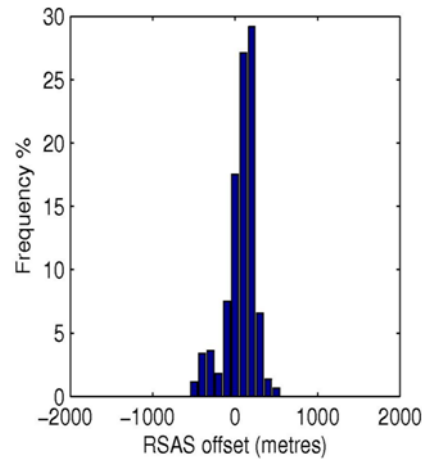

Figure B-4. *Tangent height registration histogram for 450 simulated LS events. Mean offset = 120m, Ensemble standard deviation = 175 m*
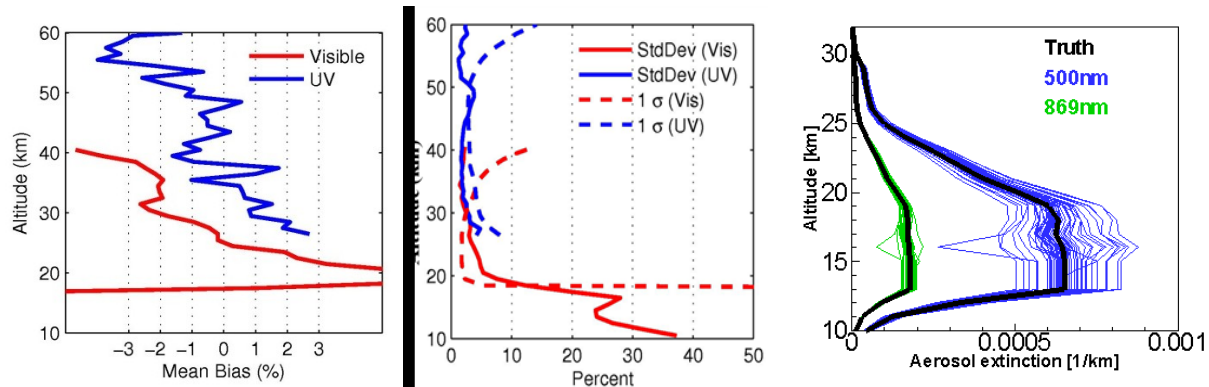
Figure B-5. *(Left and center frames) Ozone retrieval statistical performance for 450 simulated limb scatter events. (Right frame) Aerosol retrieval statistical performance for 100 simulated limb scatter events.*

B.3.2 DOE testing with un-gridded data

The second test series considers a small set of synthetic CCD maps constructed with the forward model and the detailed Instrument model. Figures B-6 and B-7 show ozone retrieved directly from the CCD pixel map shown on Figure B-2. Figure B-6 compares the retrieval 1 σ retrieval uncertainties (shaded area) with the differences between input and retrieved ozone profiles for Slit 1, whereas Figure B-7 corresponds to Slit 2. For both cases, the retrieval is performed using the data for all available gains, i.e., narrow/large apertures and long integration time for UV channels, and narrow/large apertures and short/long integration times for visible channels. Saturated pixels and pixels with low SNR are discarded before the retrieval. A high frequency structure can be observed (due to data and retrieval samplings being the same, namely 1km), but biases are generally low, with 1 σ uncertainty of 2-3%. Retrievals can alternatively be obtained using data from only one gain to investigate the performance of the sensor. The DOE technique is very promising in terms of retrieval quality, ease of use, flexibility (results shown on Figures B-6 and B-7 were obtained assuming 10% dead pixels randomly distributed on the CCD array) and minimum pre-processing requirements. Its CPU time requirements are similar to the ones of the Doublet/Triplet method.
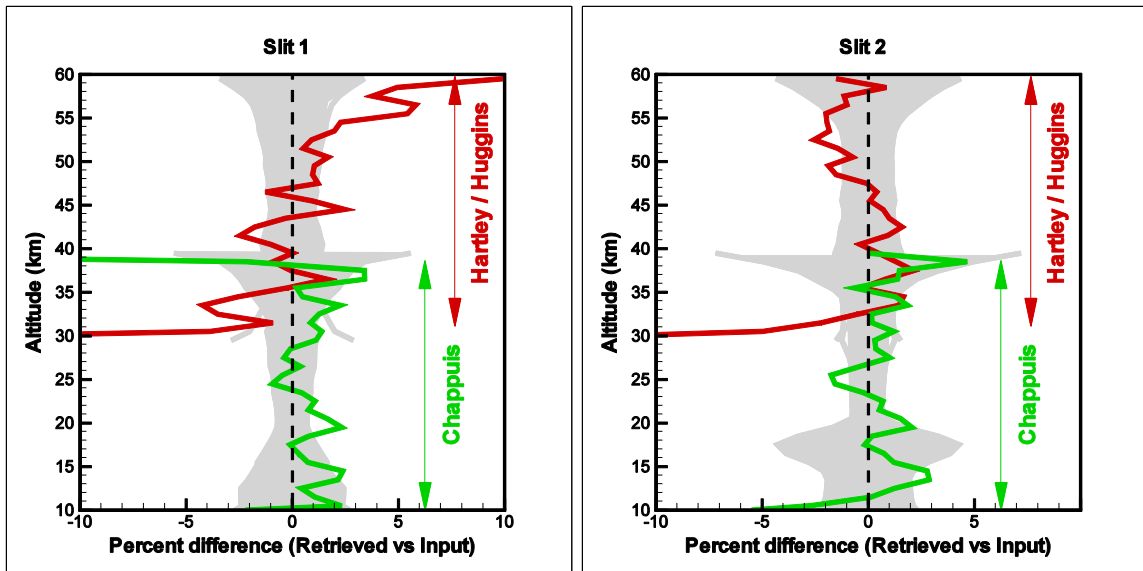
Figure B-6. *Ozone retrieval with DOE for Slit 1. (UV retrieval uses High/Low gains at long integration time. Visible retrieval uses all 4 gains). Grey shaded area corresponds to retrieval 1 σ uncertainty.*

Figure B-7. *Ozone retrieval with DOE for Slit 2. (UV retrieval uses High/Low gains at long integration time. Visible retrieval uses all 4 gains).. Grey shaded area corresponds to retrieval 1 σ uncertainty*

APPENDIX C. OMPS/LP INSTRUMENT MODEL

The Instrument Model (IM) was conceived to simulate the main functions of the OMPS/LP sensor. The IM first establishes the spectral and spatial registrations of each CCD pixel, using the CBC and SRG calibration tables described in Table 1-2. The spectral bandwidth and spatial Field-of-View (FOV) functions compiled in the BPS and FOV calibration tables are used to convolve the high resolution forward model radiance data with the inner core of the sensor slit functions. The radiance on each pixel is then converted into electrons and counts for the two integration times using the radiometric coefficients stored in the RAD calibration table.
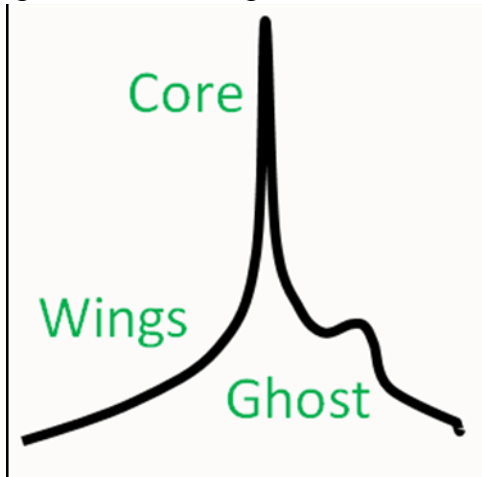

Figure C-8. *Schematic representation of instrument slit function. The near Gaussian core is typically asymmetric. The wings are due to optical imperfections and ghosts are due to internal reflections*

The Point Spread Functions (PSFs) of each CCD pixel, which are stored in the SLT calibration table, are used in the straylight contamination module. As shown in Figure C-8, the PSF is composed of non Gaussian "wings" (asymmetric side lobes, which accounts for optical design imperfections) and ghosts (due to reflections on filter edges). The SLT table defines the PSF wings and ghosts on a subsample of 108 CCD pixels spread over the 6 CCD images at the location where actual measurements were made. Bilinear interpolation is used to compute the wings strength, ghost relative position (with respect to PSF centroids) and ghost magnitude at each of the 740x340 CCD pixels. Straylight is computed by convolving the limb radiance on each of the 340x740 CCD pixels with the corresponding PSF, which itself is defined with about 1 million points. The convolution is straightforward but CPU time intensive. The convolution can however be markedly optimized by taking advantage of the rapidly decreasing strength of the PSF wings with distance from the PSF centroid. Defining PSF "pixel layers" as concentric groups of pixels around the PSF centroid (Figure C-9), and letting the layers progressively increase in size as distance to centroid is increased, it is possible to redefine the PSF of each pixel as an ensemble of about 1000 elements (Figure C-10), which can be then stored and used in the convolution, thus decreasing the CPU time by 3 orders of magnitude. The contribution of the ghosts, which are relatively small in size, can then be superimposed to complete the straylight evaluation. Figure C-11 shows the resolution at which the PSF is defined.

In its last module, the IM evaluates the dark current and smear contributions, and subsequently quantifies the sources of instrument noise, such as shot noise (square root of the number of electrons) and dark current noise. The IM output is an array of counts to represent the signal strength on each illuminated CCD pixel.
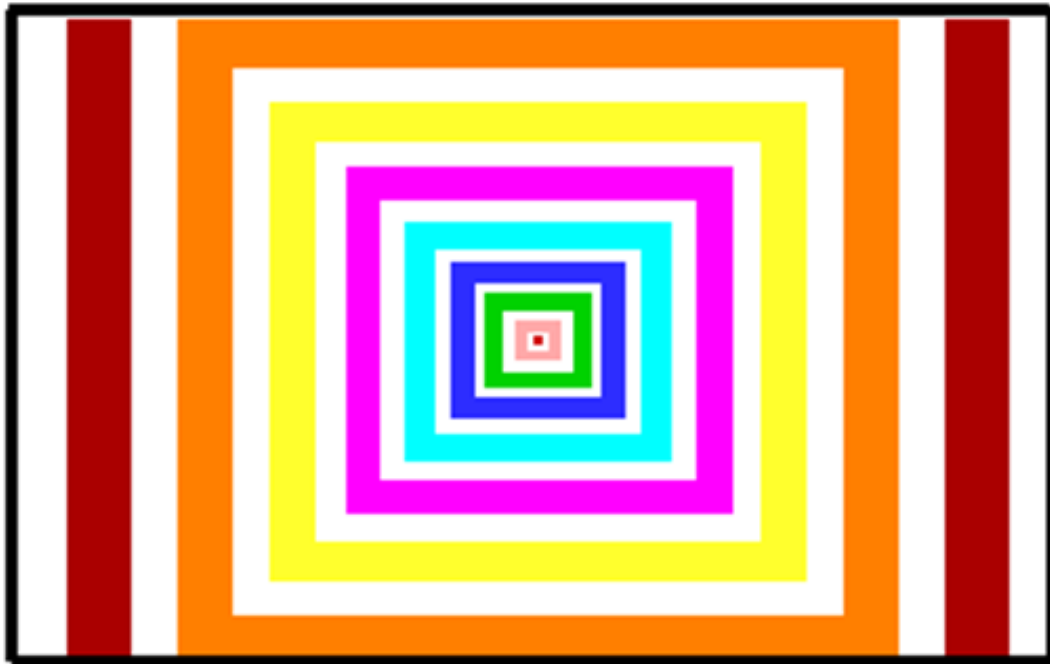

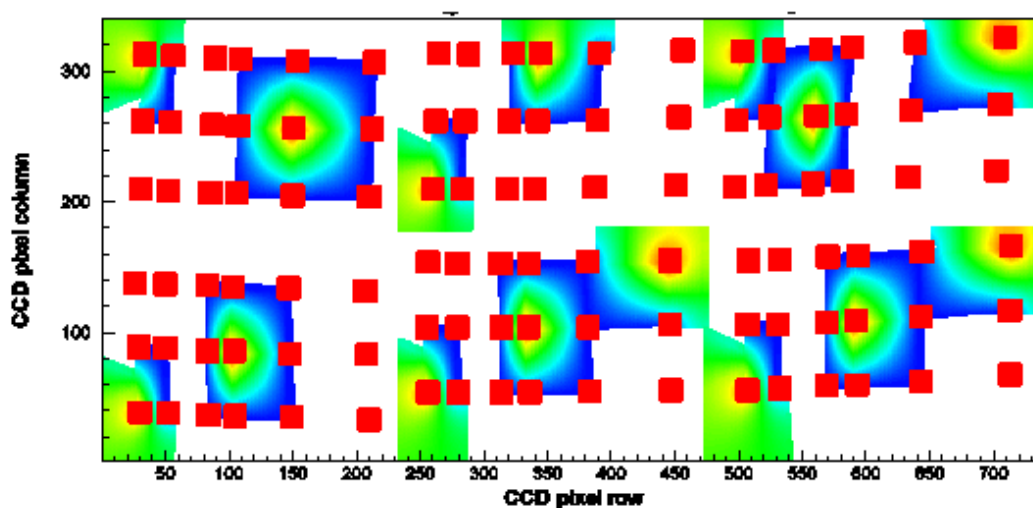**Figure C-9.** *PSFs approximate representation. Pixel layering concept*

Figure C-10. *Bilinear interpolation for PSF. Red squares denote the location of the 108 PSF measurements. The color contours show a sample of the bilinear coefficients used for the interpolation of PSF and ghosts.*
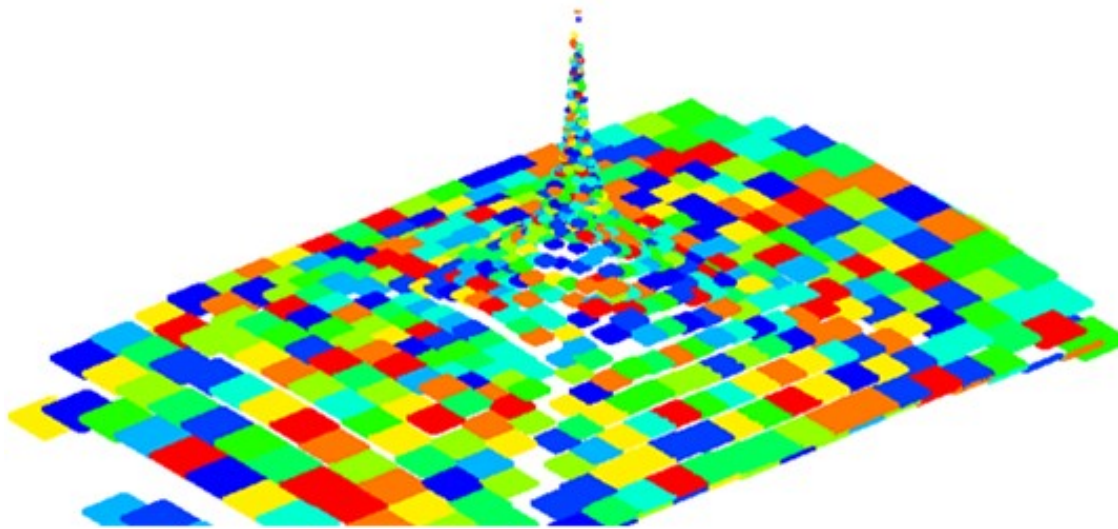
Figure C-11. *Variable resolution PSF. Each color represents one of about 1000 PSF elements within which PSF is assumed to be constant*